Skoltech
Skolkovo Institute of Science and Technology

Skolkovo Institute of Science and Technology

OPTICAL PROPERTIES OF HOLLOW-CORE MICROSTRUCTURED FIBERS
MODIFIED BY POLYMERS AND/OR INORGANIC NANO- AND SUBMICRON
PARTICLES

Doctoral Thesis

by

TIMUR ERMATOV

DOCTORAL PROGRAM IN PHYSICS

Supervisor
Professor Dmitry Gorin

Moscow - 2021

I hereby declare that the work presented in this thesis was carried out by myself at Skolkovo Institute of Science and Technology, Moscow, except where due acknowledgement is made, and has not been submitted for any other degree.

Candidate (Timur Ermatov)

Supervisor (Prof. Dmitry Gorin)

Abstract

This work presents a study of the fabrication and the experimental and theoretical characterization of functionalized hollow-core microstructured optical fibers (HC-MOFs). It was accomplished in the scope of a doctoral thesis at the Skolkovo Institute of Science and Technology in Moscow.

HC-MOFs provide a new means of exploiting the unique optical properties of hollow waveguides, such as a broad window of transmission extending far into the infrared, and the guidance in low refractive index materials that is totally impossible in conventional optical fibers. At the same time, when filling the hollow capillaries of HC-MOFs with liquid or gas medium, the overlap of a dissolved or suspended sample with the light field is close to unity giving rise to high sensitivity. Moreover, a series of post-processing techniques applied to the fibers improve their performance and gives a rise to new applications.

Within the framework of this thesis a comprehensive study of new experimental techniques that allow the controlled modification of the inner surface of fiber capillaries with nanofilms of various thicknesses and nature (polymer, organic, composite) using the highly controllable and reproducible layer-by-layer (LbL) assembly is introduced. The impact of the functionalization on the optical transmission of HC-MOFs has been investigated in a broad spectral range (400 – 1500 nm).

Following the emerging fields of biophotonics and optofluidics, the practical application of in-fiber multispectral optical sensing (IMOS) based on a set of functionalized HC-MOFs has been verified by advanced refractometric measurements of biological liquids on the example of bovine serum albumin (BSA) at different concentrations. Albumin is the most abundant circulating protein. The plasma albumin concentration is normally between 35 and 50 $g\,L^{-1}$, while its deviations indicate various abnormal conditions and diseases. The performance of IMOS has been demonstrated by measuring the concentration of BSA dissolved in water and a phosphate-buffered saline solution in both static and dynamic modes and a resolution of ~1 $g\,L^{-1}$ when determining the BSA concentration was shown, which matches the accuracy of standard tests on

albumin. Pushing the limits further, it might eventually be possible to retrieve detailed information on the investigated solutions *in situ*.

The foundations of this thesis can be found throughout different fields of science and technology. Therefore, a brief introductory review of the relevant fields will be given

A theoretical study based on the analytic treatment of resonant guidance in HC-MOFs as well as numerical simulations covering the evolution of transmission spectra followed by the functionalization of fiber capillaries provided a deeper insight into the guidance mechanism and helped the extraction of the thicknesses of deposited layers and the refractive indices of the investigated solutions.

List of publications

Research articles

1. T. Ermatov, R. E. Noskov, A. A. Machnev, I. Gnusov, V. Atkin, E. N. Lazareva, S. V German, S. S. Kosolobov, T. S. Zatsepin, O. V Sergeeva, J. S. Skibina, P. Ginzburg, V. V Tuchin, P. G. Lagoudakis, D. A. Gorin, «Multispectral sensing of biological liquids with hollow-core microstructured optical fibres», *Light: Science & Applications* **2020**, *9*, 173 (Q1, IF 17.8).

TE and RN have an equal contribution.

2. T. Ermatov, Y. V. Petrov, S. V. German, A. A. Zanishevskaya, A. A. Shuvalov, V. Atkin, A. Zakharevich, B. N. Khlebtsov, J. S. Skibina, P. Ginzburg, R. E. Noskov, V. V. Tuchin, D. A. Gorin, «Microstructured Optical Waveguide-Based Endoscopic Probe Coated with Silica Submicron Particles», *Materials* **2019**, *12*, 1424 (Q2, IF 3.6).

Main contribution.

3. S. Perevoschikov, N. Kaydanov, **T. Ermatov**, O. Bibikova, I. Usenov, T. Sakharova, A. Bocharnikov, J. Skibina, V. Artyushenko, D. Gorin, «Light Guidance up to 6.5 μm in Borosilicate Soft Glass Hollow-Core Microstructured Optical Waveguides», *Optics Express* **2020**, *28*, 27940 (Q1, IF 3.9).

Contribution: transmission spectra measurements of hollow-core microstructured optical fibers.

4. Timur Ermatov, Marina Novoselova, Julia S. Skibina, Andrey Machnev, Dmitry A. Gorin, Roman E. Noskov, «Ultrasmooth, Biocompatible, and Removable Nanocoating for

Hollow-Core Microstructured Optical Fibers», *Optics Letters* **2021**, 46 (19), 4828 – 4831 (Q1, IF 3.8).

Main contribution.

5. Timur Ermatov, Ivan Gnusov, Julia Skibina, Roman Noskov, Dmitry Gorin, «Noncontact characterization of microstructured optical fibers coating in real-time», *Optics Letters* **2021**, 46 (19), 4793 – 4796 (Q1, IF 3.8).

Main contribution.

6. Nikita Kaydanov, Stanislav Perevoschikov, Sergei V. German, Stepan A. Romanov, **Timur Ermatov**, Anton A. Kozyrev, Julijana Cvjetinovic, Roman E. Noskov, Sergey S. Kosolobov, Julia S. Skibina, Albert G. Nasibulin, Christian Zakian, Pavlos G. Lagoudakis, Dmitry A. Gorin, **«**Optoacoustic effect in a hybrid multilayered membrane deposited on a hollow-core microstructured optical waveguide», just accepted to *ACS Photonics* (Q1, IF 7.5).

Contribution: transmission spectra measurements of hollow-core microstructured optical fibers.

Review articles

1. T. Ermatov, J. S. Skibina, V. V. Tuchin, D. A. Gorin, «Functionalized Microstructured Optical Fibers: Materials Methods Applications», *Materials* **2020**, 13, 921 (Q2, IF 3.6).

Main contribution.

Patents

1. Microstructured optical fiber-based gas sensor, application № 2019140431, in collaboration with Nanostructured Glass Technology, **2019.**

2. Sensor device for recognition of mixtures of volatile compounds and methods of its production, application № 2019143523, in collaboration with Samsung Research Center Russia, **2020.**

3. Optoacoustic sensor based on structural optical fiber, application № 2020113886, in collaboration with Laboratory of Nanomaterials Skoltech, **2021.**

Conference proceedings

1. T Ermatov, J. S. Skibina, R. E. Noskov and D. A. Gorin, «Layer-by-layer assembled-composite nanocoating for functionalization of microstructured optical fibers», *Journal of Physics: Conference Series* **2020**, 1571, 012006 (Q4, IF 0.5).

Main contribution.

Participation in scientific conferences

1. 28th International Conference on Advanced Laser Technologies, 6 – 10 September 2021, talk with title *"Optical properties of functionalized microstructured fibers and their sensing capabilities"*, online format.

2. Novel Photonic, Optoelectronic and Electronic Materials SPb-POEM 2021, 25 – 28 May 2021, talk with title *"Optical properties of functionalized microstructured fibers and their sensing capabilities"*, online format.

3. Saratov Fall Meeting, International Conference on Optics and Photonics. VIII Symposium on optics & biophotonics, 29 September – 2 October 2020, talk with title *"Functionalized Microstructured Optical Fibers in Biophotonics",* online format.

4. Novel Photonic, Optoelectronic and Electronic Materials SPb-POEM 2020, 27 – 30 April 2020, talk with title *"Layer-by-layer deposition technique for the functionalization of microstructured optical fibers"*, online format.

5. Saratov Fall Meeting, International Conference on Optics and Photonics. VII Symposium on optics & biophotonics, 23 – 27 September 2019, talk with title *"Microstructured Optical Waveguide-Based Endoscopic Probe Coated with Silica Submicron Particles"*, Saratov, Russia.

Table of Contents

List of Symbols, Abbreviations

AFM – atomic force microscopy

BSA – bovine serum albumin

CTC – circulating tumor cells

FOM – figure of merit

FWHW – full width at half maximum

HC – hollow-core

HC-MOF – hollow-core microstructured optical fiber

IMOS – in-fiber multispectral optical sensing

LbL – layer-by-layer

LC – liquid cell

LMR – lossy mode resonance

LPG – long period grating

LSPR – localized surface plasmon resonance

MOF – microstructured optical fiber

MRI – magnetic resonance imaging

NA – numerical aperture

OF – optical fiber

OFS – optical fiber sensor

PAH – poly (allylamine hydrochloride)

PBGF – photonic band gap fiber

PBS – phosphate buffer saline

PC – photonic crystal

PCF – photonic crystal fiber

PDDA – poly (diallyldimethylammonium chloride)

PE – polyelectrolyte

PEI – polyethylenimine

PSS – poly (styrenesulfonate)

RI – refractive index

RIS – refractive index sensetivity

RIU – refractive index unit

QCM – quartz crystal microbalance

SC – solid-core

SC-MOF – solid-core microstructured optical fiber

SEM – scanning electron microscopy

SFM – surface force microscopy

SPR – surface plasmon resonance

TA – tannic acid

TFBG – tilted fiber Bragg grating

TIR – total internal reflection

List of Figures

14

List of Tables

1. Chapter 1. Introduction

1.1 Motivation

Since its inception in 1996 [1], microstructured optical fibers (MOFs) have been widely developed including the realization of advanced coatings on both the inner and outer fiber surface [2,3]. In contrast to all-solid optical fibers (OFs) made of silica and its counterparts, the structure of MOFs forming by an array of air channels allows the fabrication of single-material fibers with a high air-filling fraction (>90%) [4,5] giving rise to the appearance of separate classes of optical waveguides called hollow-core and solid core MOFs (HC-MOFs and SC-MOFs) [6]. Traditionally, conventional optical fibers are extensively used in various fields of photonics, communications, and remote sensing [7]. The realization of light guidance in the air-filled core, in turn, enables strong interaction between an injected medium and the light mode that opens new perspectives for applications of holey OFs, which are not possible with all-solid fibers. In particular, several technological breakthroughs such as the low-loss light guidance, guidance only of the fundamental mode at all frequencies, supercontinuum generation and transmittance in near- and middle-IR spectral ranges were reported for HC-MOFs [8–10].

The other important advantage of HC-MOFs is the accessibility of the fiber air channels for molecular and nanoscale functionalization that brings application-oriented functionalities into fibers in fields such as optics, biophotonics and healthcare [2,3]. Moreover, functional nanocoatings of HC-MOFs have extended the domain of their applications to biosensing and photochemistry [11]. These approaches include immobilization of plasmonic nanoparticles for Raman-assisted detection, antibody/antigen

biosensing and optofluidic refractive index (RI) sensing [12–15]. Moreover, naturally-derived materials [16] can be also incorporated into the self-assembled multilayers where nontoxic or even biocompatible materials are needed [17].

Besides, HC-MOFs represent an attractive playground for creation of in-fiber optical sensors featuring strong interaction between a guided mode and an analyte in a test [11]. The state of the art in optical biosensing is focused on reaching high sensitivity at a single wavelength by using any type of optical resonance. The latter include collective resonances in plasmonic and dielectric metasurfaces [18,19], plasmon polaritons in hyperbolic metamaterials [20] and many others [21]. Although some of these systems can support several resonances (typically less than 4), the single resonance is used for sensing, providing a maximum figure of merit and refractive index sensitivity. This common strategy, however, overlooks an interesting and promising possibility of simultaneous measurements of a bioanalyte's refractive index in a wide range of wavelengths that can act as a simple and cost-effective fingerprint of liquid biosamples providing crucial information about real-time variations in their composition without expensive and complex functionalization of sensing template nanostructures with antibodies, aptamers and other analyte binders. For this reason, the technique that allows the fast, precise and easy sensing of biological liquids in the broad spectral range is highly desirable and is a central part of this thesis [14].

Throughout this work, the author makes significant advances towards resolving this issue by introducing the method of in-fiber multispectral optical sensing (IMOS) for both the static and dynamic refractometric measurements of biological liquids. The operation

principle is based on detecting spectral shifts of multiple Fabry-Perot resonances in the core capillary wall of several functionalized HC-MOFs with slightly shifted transmission windows when a liquid sample is streamed through it via specially designed liquid chambers.

It is worth to mention, that regardless of the various experimental techniques applied for the creation of functional coatings on the fiber surfaces, no detailed characterization of transmission losses in functionalized fibers has been published yet. However, novel modalities typically come with increased optical losses since a significant surface roughness of functional layers gives rise to additional light scattering, restricting the performance of functionalization. Another problem is that the conventional strategies rely on using materials with poor biocompatibility and high toxicity which are not optimal for sensitive *in vivo* applications.

To solve this issue, the author introduces a novel type of biocompatible and removable nanocoating for HC-MOFs formed by layer-by-layer assembly of stimuli-responsive organic materials, thus decreasing the coated fiber optical losses by a factor of 3. Additionally, the creation of a reusable MOF-based biosensor has been demonstrated using organic multilayers deposited on the inner fiber surface.

The following chapters will try to give a detailed study of the functionalized HC-MOFs, discussing the possibilities and limitations of hybrid waveguide fabrication and presenting a series of optical experiments that illustrate practical usage and realization of the produced structures.

1.2 Outline of this thesis

After a brief introduction to the topic (chapter 1), the theoretical background required for a fundamental understanding of the reported questions is given in Chapter 2, including waveguide theory of the conventional step-index fibers based on total internal reflection phenomenon and microstructured optical fibers that allow for the light guidance in low refractive index materials. Chapter 2 continues with a brief description of the most widely used techniques used for functionalization of optical fibers emphasizing the key characteristics of layer-by-layer (LbL) assembly. One-dimensional (1D) and opal-like photonic crystals are discussed at the end of Chapter 2.

Chapter 3 describes a series of experimental fabrication techniques applied for the surface modification of fiber capillaries. They rely on the electrostatic attraction of inversely charged polyelectrolytes, hydrogen bonding and hydrophobic interactions of organic nanoparticles, with entropy factor playing a significant role. The fabrication chapter includes a study of coating growth depending on various assembly conditions and analysis of transmission losses induced by deposited structures. Additionally, post-processing techniques applied to the coated fibers are discussed in Chapter 5 on the example of pH-responsive organic films.

Chapter 4 is devoted to the experimental realization of the porous functional layer on the top of the sensitive surface of the 1D photonic crystal. The practical realization of the designed sensor structure has been demonstrated by monitoring the relative humidity change.

Chapter 6 dedicated the "proof-of-concept" work that presented the real-life application of functionalized HC-MOFs for multispectral refractometric measurements of biological liquids at different concentrations. All the experiments are done at both static and dynamic regimes.

Chapter 7 gives a short conclusion and the statement of primary outcomes along with the possible future applications based on functionalized MOFs.

2. Chapter 2. Theoretical background

In this chapter, the theoretical background required for a fundamental understanding of the topics presented in this thesis is introduced. A detailed discussion or derivation of the equations is beyond the scope of this work. A comprehensive description of electromagnetic theory and light-matter interaction can be found in textbooks such as [18, 19, 20].

2.1 Historical overview of fiber optics

The birth of modern fiber optics is associated with the discovery of the phenomenon of total internal reflection (TIR) for the light traveling at the border of two media that has been shown by Johannes Kepler, a German mathematician and astronomer, in 1611, ten years before Willebrord Snell derived his famous formula for the refraction of light [22].

One of the first experimental realizations demonstrating that light can be confined and guided inside a transparent curved medium goes back to the year 1842, when Jean-Daniel Colladon, a 39-year-old professor at the University of Geneva, published an article "On the reflections of a ray of light inside a parabolic liquid stream" [23]. He wanted to show fluid flow through various holes and the breaking up of water jets observed earlier by French physicist Felix Savart [24]. When the light rays in the water hit the edge of the jet at a glancing angle, TIR trapped them in the liquid (Figure 2.1).
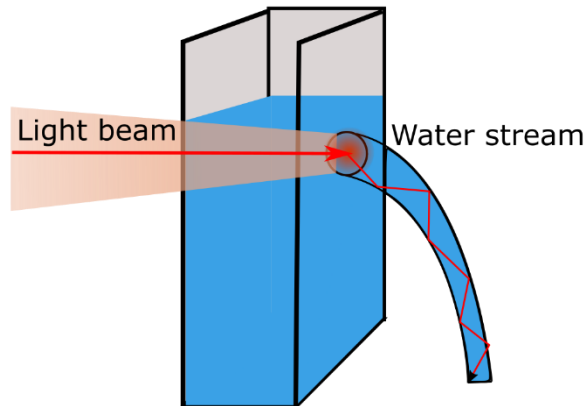
Figure 2-1: A beam of light is focused through a water-filled rectangular tank and onto an opening on the other side. The light is guided along the water jet by total internal reflection.

However, the first practical application of optical fibers was demonstrated almost one hundred years later in the form of fiber bundles without a cladding layer for medical imaging or endoscopy [25,26]. However, light can easily leak from unclad fibers where they touch other objects (Figure 2.2a) [24]. The use of different materials for waveguiding kept advancing the field over the decades, followed by the idea of embedding the high-index fiber core in a low-index glass cladding arose during the development of the first gastroscope by Lawrence Curtiss (Figure 2.2b) [24].
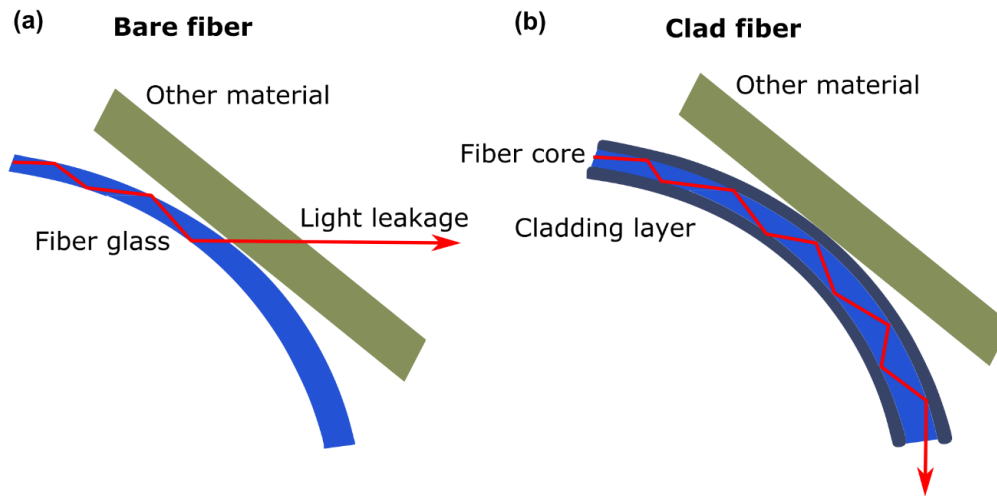
Figure 2-2: Light can leak from unclad fibers where they touch other objects. (b) Total internal reflection at the boundary between core and cladding guides light along a clad optical fiber. Adapted from [24].

Nevertheless, even after the advent of lasers in the early 1960s, the use of optical fibers for long-distance data transmission did not appear practicable since the optical losses of glasses were still too high for telecommunication purposes. It was Charles Kao and George Hockham [27] who theoretically analyzed what structural and material requirements needed to be fulfilled to reduce losses in silica giving rise to modern fiber optics, and earning Kao the Nobel prize in Physics in 2009 [28].

A major step in the field of fiber optics was the invention of microstructured optical fibers by Philip Russell, demonstrated experimentally in 1996 on solid-core MOFs whose structure is defined by an array of air-channels, running through the whole fiber length [1] (Figure 2.3). The idea to guide light by means of a photonic crystal cladding is based on the concept of photonic crystals proposed by Reinhard Ulrich [9], Philip Russell [10], Sajeev John [11] and Eli Yablonovich [12] in the 1980s. The first HC-MOF was experimentally realized in 1999 by Cregan *et al*. [29].
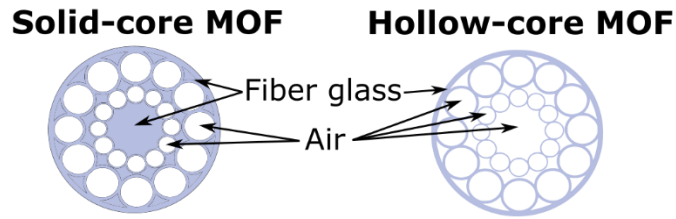
Figure 2-3: Schematic of solid-core and hollow-core MOFs.

Solid-core MOFs exploiting the principle of total internal reflection for light guidance in a high refractive index core, represent the major group of these fibers, however, they can also guide light in a low refractive index core based on the photonic bandgap guidance [3]. HC-MOFs represent a separate class of optical waveguides, in which confinement of transmitted light is ensured by an array of air-capillaries surrounding the central hollow core. In addition to all the other advantages and features of optical fibers, MOFs with their capability to guide light in the HC region and the strong interaction with an injected medium open new perspectives for their practical applications, which are not possible with all-solid fibers [3]. In such structures, light guidance can be achieved by two different methods, both, however, avoid the need for total internal reflection [30]. First is the two-dimensional photonic bandgap mechanism, which allows tight optical confinement and transmittance of the light inside HC and prevents its escape into the photonic-crystal cladding. These structures are referred to as hollow-core photonic bandgap fibers (PBGFs) and lie within the scope of photonic-crystal fibers (PCFs). The central light-guiding HC surrounded by a thin glass wall (50–150 nm) supports the transmission of a tiny wavelength band with low loss over the whole waveguide length [5,31]. Another method is based on an anti-resonant reflecting optical waveguide structure. These are so-called hollow-core anti-resonant fibers (or inhibited-coupling fibers) [5]. They, in turn, do not allow the

realization of photonic bandgap guidance because the glass wall thickness (typically hundreds of nanometers) is thicker than that required for broadband or multiband PBGFs. Nevertheless, featuring the relatively low loss operation [5,32,33] over the broad wavelength range, hollow-core anti-resonant fibers can further enhance the capability of HC-MOFs in various applications [10].

Sections 2.2 – 2.4 will introduce Maxwell equations, complex refractive index formula and the theory of effective medium approximation used for the extraction of refractive indices of single compounds out of complex mixtures.

2.2 Maxwell equations

Light propagation in periodic complex structures has aroused considerable interest in the past few years. This interest was largely stimulated by Yablonovitch and co-workers who suggested that diffraction by periodic structures might lead to a 'photonic insulator' or photonic bandgap in which light is forbidden to propagate in a certain range of frequencies [34]. Maxwell's equations describe the generation and propagation of electromagnetic waves and relate the corresponding fields ($\vec{D}(\vec{r}, t)$, $\vec{B}(\vec{r}, t)$, $\vec{E}(\vec{r}, t)$ and $\vec{H}(\vec{r}, t)$) to their sources (current density ($j(\vec{r}, t)$ and charge density $\rho(\vec{r}, t)$), depending on space $\vec{r}$ and time t [35]. In their final form, they were developed by James Maxwell in 1865 [21] and combine Gauss's laws, Faraday's law of induction and Ampere's law including the time-derivative of the displacement vector $\vec{D}$. Maxwell's equations in SI units are typically written as a set of four linear partial differential equations (Eqs. 2.1 – 2.4):

$$\vec{\nabla} \times \vec{E}(\vec{r}, t) = -\frac{\partial}{\partial t} \vec{B}(\vec{r}, t) \tag{2.1}$$

$$\vec{\nabla} \times \vec{H}(\vec{r}, t) = -\frac{\partial}{\partial t} \vec{D}(\vec{r}, t) + \vec{j}(\vec{r}, t) \tag{2.2}$$

$$\vec{\nabla} \cdot \vec{D}(\vec{r}, t) = \rho(\vec{r}, t) \tag{2.3}$$

$$\vec{\nabla} \cdot \vec{B}(\vec{r}, t) = 0 \tag{2.4}$$

where ρ is the external charge density, $\vec{j}$ corresponds to the macroscopic current density, $\vec{D}$ and $\vec{B}$ are electric displacement and magnetic flux density (or magnetic induction), respectively.

In a vacuum, the fields $\vec{D}$ and $\vec{E}$, and $\vec{B}$ and $\vec{H}$, respectively, are related through (Eqs. 2.5 – 2.6):

$$\vec{D} = \varepsilon_0 \vec{E} \tag{2.5}$$

$$\vec{B} = \mu_0 \vec{H} \tag{2.6}$$

In SI unit, $\varepsilon_0 = 8.8542 \times 10^{-12}$ F m^{-1} is the vacuum permittivity and $\mu_0 = 4\pi \times 10^{-7}$ H m^{-1} is the vacuum permeability which has a relationship with the vacuum speed of light as (Eq. 2.7):

$$c = \frac{1}{\sqrt{\varepsilon_0 \mu_0}} \tag{2.7}$$

In optics, we can assume $\vec{j} = 0$ and $\rho = 0$. For non-magnetic media, the magnetism is weak and $\mu \sim 1$.

2.3 Complex refractive index

The refractive index n of a medium can then be defined as a function of ε and μ (Eq. 2.8):

$$n = \sqrt{\varepsilon \mu} = n_{real} + i n_{imaginary} \tag{2.8}$$

where the real part, n_{real}, shows the ratio of the velocity of light in vacuum and the velocity of light in the medium, and the imaginary part, $n_{imaginary}$, is the extinction coefficient, related to the material absorption in a medium.

2.4 Effective medium approximation theory

Effective medium approximation (EMA) theory aims to approximate a complex electromagnetic medium such as a colloidal solution of micro- and nanoparticles in water with a homogeneous effective medium [36]. The EMA mixing formulas give the permittivity of this effective medium in terms of the permittivities and volume fractions of the individual constituents of the complex medium [36]. Two different cases might be highlighted in the framework of EMA theory. The first is when one of the components can be considered as a host in which inclusions of the other components are embedded (Figure 2.4a), whereas the second is more appropriate to microgeometries where the grains of the various components are symmetrically distributed, with no clear matrix component [37] (Figure 2.4b).
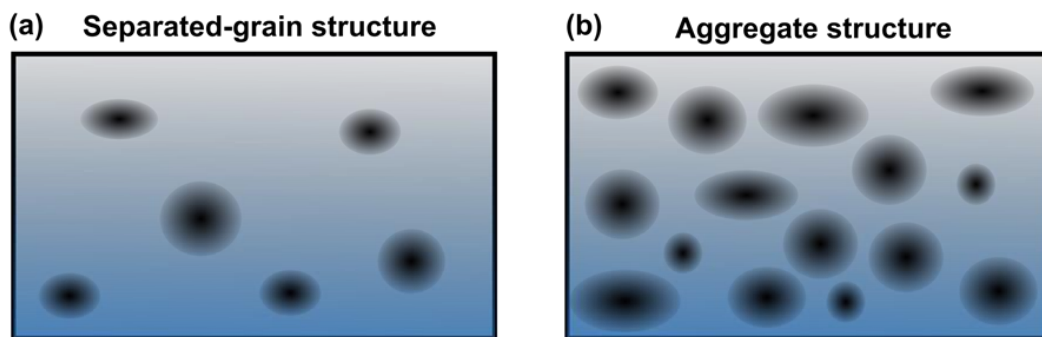
Figure 2-4:(a) separated-grain structure and (b) aggregate structure depict two microstructures for heterogeneous two-phase media.

These two approximations have been frequently used for investigating the properties of isotropic two-component mixtures, in which the components are isotropic materials with scalar dielectric coefficients and the components grains are assumed to be spherical. However, with simple generalization, EMA has been also adapted for isotropic mixtures including randomly oriented ellipsoidal grains [37].

Numerous expressions have been proposed to describe effective permittivity (ε_{eff}) in terms of the microstructural parameters and the dielectric functions of the constituents. The Maxwell Garnett mixing formula (Eq. 2.9) used for the cases when the volume fraction of the "host" or "environment" is much larger than that of the "inclusions".

$$\varepsilon_{eff} = \varepsilon_e + \varepsilon_e \frac{\frac{f_i}{3}\sum_{j=x,y,z}\frac{\varepsilon_i-\varepsilon_e}{\varepsilon_e+N_j(\varepsilon_i-\varepsilon_e)}}{1-\frac{f_i}{3}\sum_{j=x,y,z}\frac{N_j(\varepsilon_i-\varepsilon_e)}{\varepsilon_e+N_j(\varepsilon_i-\varepsilon_e)}} \qquad (2.9)$$

where ε_e and ε_i are the permittivities of the environment or host medium and the inclusions, respectively, f_i is the volume fraction of the inclusions, and N_x, N_y and N_z are the depolarization factors over the x, y and z axes, respectively.

Bruggeman formalism (Eq. 2.10), in turn, is symmetric with respect to all medium components and does not treat any one of them differently. There is no more host-versus-guest hierarchy.

$$(1 - f_1)\frac{\varepsilon_2-\varepsilon_{eff}}{\varepsilon_2+2\varepsilon_{eff}} + f_1 \frac{\varepsilon_1-\varepsilon_{eff}}{\varepsilon_1+2\varepsilon_{eff}} = 0 \qquad (2.10)$$

where ε_1 and ε_2 are permittivities of the 1st and 2nd compounds of the mixture, and f_1 is the volume fraction of the 1st compound.

Section 2.5 is devoted to the description of the light guidance of the conventional optical fibers. Sections 2.6 – 2.8 introduce the other type of optical fibers which is HC-

MOFs and give information about their fabrication technique along with the description of the main optical properties.

2.5 Light guidance in conventional optical fibers

In the most general case, the light guidance is achieved by the proper choice of fiber materials: a fiber core is made with a material whose refractive index is slightly higher than that of the surrounding cladding. For a step-index fiber, the light guidance can be explained using the model of the total internal reflection of light beams at the border between core and cladding zones (Figure 2.5).
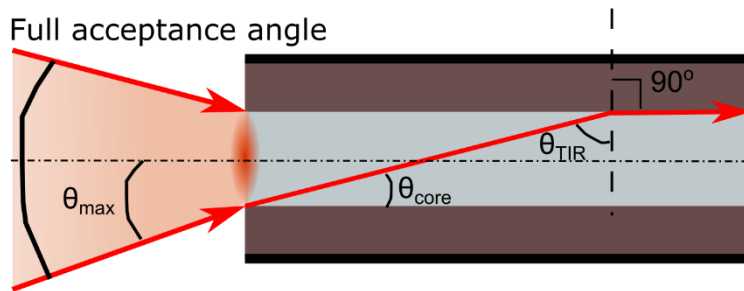
Figure 2-5: Schematic of light guidance in step-index optical fibers. The full acceptance angle illustrates the maximum light cone which is allowed to propagate in the fiber structure.

One easily concludes that total internal reflection at the interface occurs if the external beam angle θ (in the air) fulfills the condition (Eq. 2.11):

$$\sin \theta = \frac{n_{cladding}}{n_{core}} \qquad (2.11)$$

where θ is the external beam angle, and *sin θ* is also called numerical aperture of the fiber (NA), $n_{cladding}$ and n_{core} state for the RI of the fiber cladding and core, respectively.

For the comparatively large sizes of the fiber microstructure, the treatment of the light propagation in terms of geometrical optics gives reasonable results (strongly

multimode fibers), but is invalid for single-mode fibers consisting of smaller cores, where we should consider the wave nature of light (Figure 2.6).
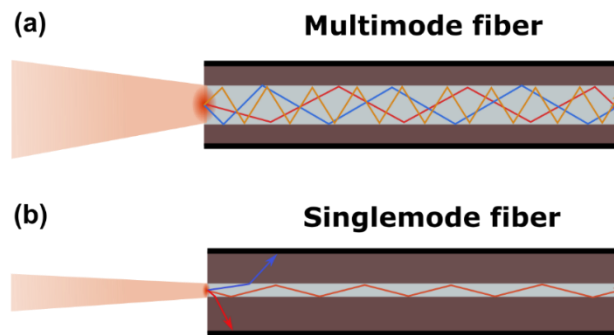
Figure 2-6: Schematic of multimode (a) and single-mode (b) OFs. Color arrows indicate light different modes. Multimode fibers consist of a relatively large core (~ hundreds of microns) surrounded by a cladding layer. Single-mode fibers are featured a smaller core with a typical size of few microns so the only fundamental light mode can propagate along the whole fiber length while the higher-order modes are escaped in the cladding.

The more detailed study of light propagation in optical fibers requires considering a wave phenomenon of light as well. A comprehensive description of the beam propagation method can be found in textbooks such as [38].

2.6 Fabrication of hollow-core microstructured optical fibers

The extensive development of HC-MOFs was driven by a novel fabrication method called the "stack-and-draw" technique. The technique was first introduced by Philip Russell in 1996 [1] and has become the favored fabrication tool for the production of holey fibers. The preform for MOF production is created by stacking several glass capillaries and rods to achieve the designed air-glass structure. Then MOF-preform is ready, the capillaries and glass rods are stacked together and fused during a drawing procedure. After that, the

preform is placed onto a conventional fiber drawing tower, greatly extending its length, while reducing its cross-section, from a diameter of tens of millimeters to hundreds of microns [39]. One can readily notice the versatility and simplicity of the "stack-and-draw" method that contributes to the development of various MOF designs, in particular, solid-core and hollow-core MOFs. Figure 2.7 illustrates this sequence of stack and draw. In particular, different suspended-core and Kagome fibers have been fabricated using this technique [11]. The precise fiber structure (such as the microstructured core-cladding interface) can be formed by direct adjustment of glass rods (solid-core waveguides) or by taking away several glass capillaries (hollow-core waveguides) [11].
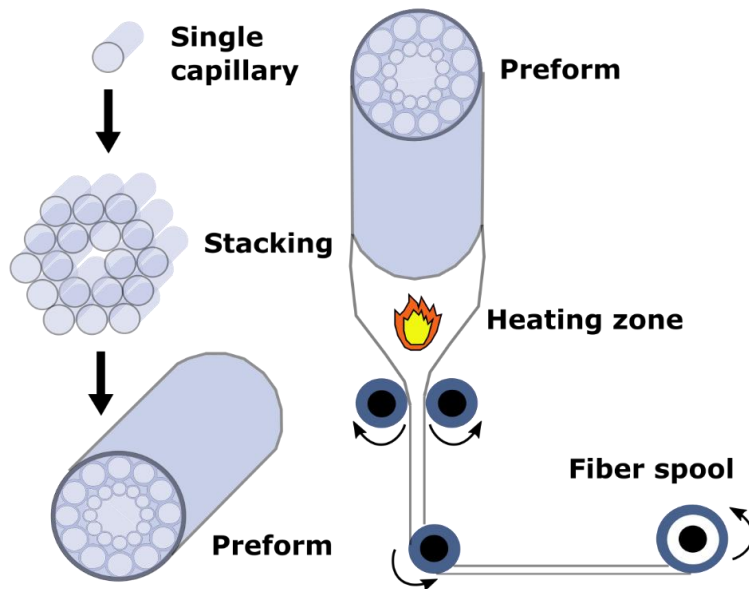
Figure 2-7: Schematic of the fabrication of microstructured optical fibers by the "stack-and-draw" method.

2.7 Physical demonstrative approach to the waveguiding properties of hollow fibers

As an initial approximation to hollow-core fibers, we can consider the simplest model of an optical waveguide consisting of a hole in a dielectric (the schematic is illustrated in Figure 2.8) [40,41]. Thus, the Fresnel reflection at the interface created by the surface separating the air-filled core with the dielectric determines the optical losses of this waveguide (Figure 2.8) [41]. However, it is possible to substantially decrease the fiber losses by increasing the reflection coefficient between the air-filled core and solid cladding interface e.g., by reflection from two media, using as a waveguide, a tube with a thin glass wall (tubular waveguide) and constructive interference of the light that is reflected from both surfaces of the capillary [41]. In this model the entire structure of the waveguide can be described within geometric optics in terms of a model of Fabry-Perot resonator, therefore, a band structure or the alteration of the resonances and antiresonances occur in the fiber transmission spectrum [41]. The reflection coefficient decreases when the light is perpendicular to the capillary wall (an incidence angle is almost $\pi/2$). As a result, that leads to high waveguiding losses. The reflection coefficient increases, when the resonance condition is violated (or the antiresonance condition is met), then the reflection coefficient from the capillary wall increases dramatically and the band structure in the transmission of optical fiber appears (Figure 2.8). Later, such a mechanism has been studied more extensively in [42] and the abbreviated name Antiresonant reflecting optical waveguide was introduced [41].
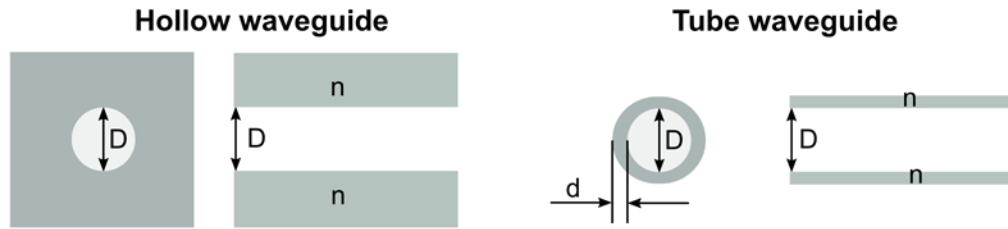
Figure 2-8: Cross- and longitudinal sections of the hollow (left) and tube (right) waveguides.

2.8 Light guidance in hollow-core microstructured optical fibers

Hollow-core microstructured optical fibers formed by a microstructured array of cladding capillaries running along the entire fiber length that prevent light escaping from the central hollow-core core due to a photonic bandgap (bandgap fibers), topological effect (kagome fibers), negative curvature phenomenon (antiresonant fibers) or coherent Bragg scattering from the air-glass interface (Bragg fibers) [43].

The soft-glass HC-MOFs employed in this work have a considerably thick wall of the central capillary of ~1.8 µm (Figure 2.9).
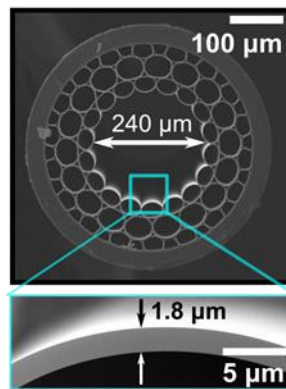
Figure 2-9: The SEM images of the fiber end face and the capillary wall of the first cladding ring.

Due to comparatively large characteristic scales of the fiber microstructure, the mechanism of light guidance in the investigated HC-MOF can be described within geometric optics. In this regime, the spectral position of the fiber transmission windows is described well by the Fabry-Perot resonances and antiresonances in the wall of the central capillary so that the fiber transmission maxima (Eq. 2.12) and minima (Eq. 2.13) occur at [42,44]:

$$\lambda_{j\,max} = \frac{4d}{2j+1}\sqrt{n_g^2 - n_c^2} \tag{2.12}$$

$$\lambda_{j\,min} = \frac{2d}{j}\sqrt{n_g^2 - n_c^2} \tag{2.13}$$

where j is an integer describing the resonance/antiresonance order ($j = 1, 2, 3, ...$), n_c is the refractive index (RI) of the medium filling the capillaries, n_g is the RI of the fiber glass, and d indicates the wall thickness for the first capillary layer.

Thus, at wavelengths other than λ_{min}, the light will be confined inside the air core with finite but low leakage loss [5]. In this spirit, the broadband and multiband light-guiding can be regarded as results of the slab shapes of the glass membranes [5]. Specifically, d = 1.8 μm and $n_c = 1$ results in 5 transmission windows in the visible and near-infrared spectral domains (400 - 900 nm), and the transmission maxima appear at 437, 488, 553, 639 and 755 nm (for j = 9, 8, 7, 6, 5). Figure 2.10 shows theoretical and experimental transmission spectra for an unmodified air-filled HC-MOF.
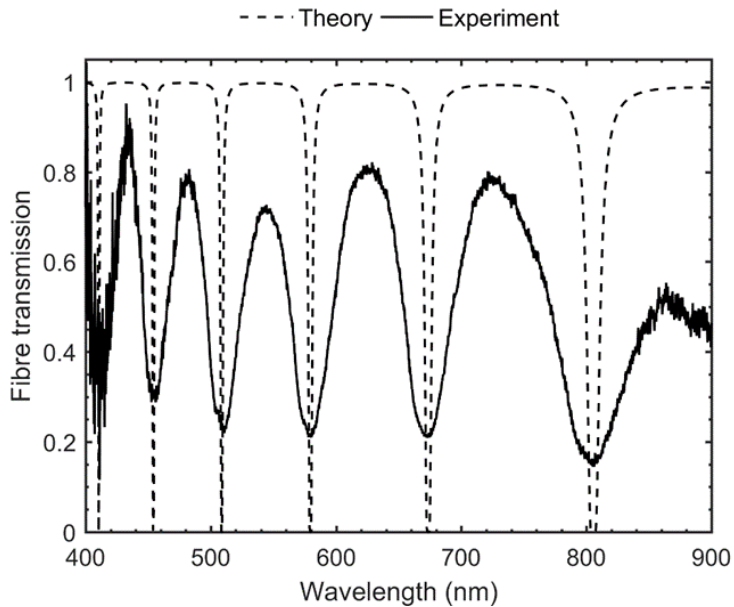
Figure 2-10: Theoretical vs experimental transmission for an unmodified and empty HC-MOF with a core diameter of 240 μm and the wall thickness for the first capillary layer of 1.8 μm [14].

The next section is devoted to the functionalized optical fibers and contains information about the materials, methods and applications of produced structures.

2.9 Functionalization of optical fibers

The recent development in thin films deposition technique enables the fiber surface modification with nano-coating layers and exploits the phenomena of surface plasmon resonance (SPR) [45,46], localized surface plasmon resonance (LSPR) [47,48] and lossy mode resonance (LMR)[49] for measuring changes in the surrounding medium through the shift of the plasmonic resonance position [50–52]. However, the strong influence of uniformity and thickness of the metal coating on sensing performance together with complicated and high-cost thin-films deposition process makes these types of sensors not always optimal for the applications there fast and easy sensing is needed [47,53]. The

necessity to cover the whole sensor surface prevents the work with low analyte volume that is crucial in bio-applications (Figure 2.11).
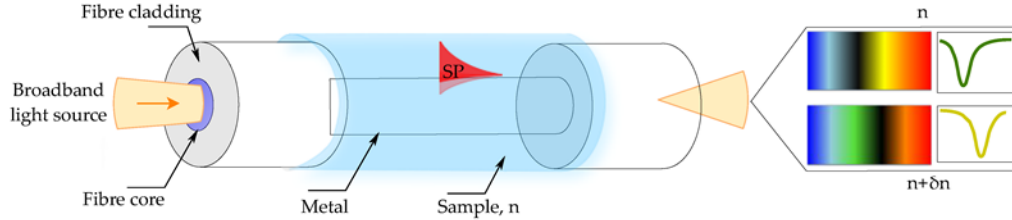
Figure 2-11: Optical fiber sensor based on SPR. Illustration of the working principle of the fiber-based SPR sensor. The shift of the plasmon resonant wavelength is associated with the change in the refractive index of the sample (δn) defining the resonant condition [52]

Among the different structures of optical fiber sensors (OFSs) and related microstructures [54], the sensors based on geometry-modified fibers (D-shaped, polished, etched and tapered) [50,55–57], grating-assisted fibers [58] and MOF [59,60] represent three the most developed OFS groups (Figure 2.12).
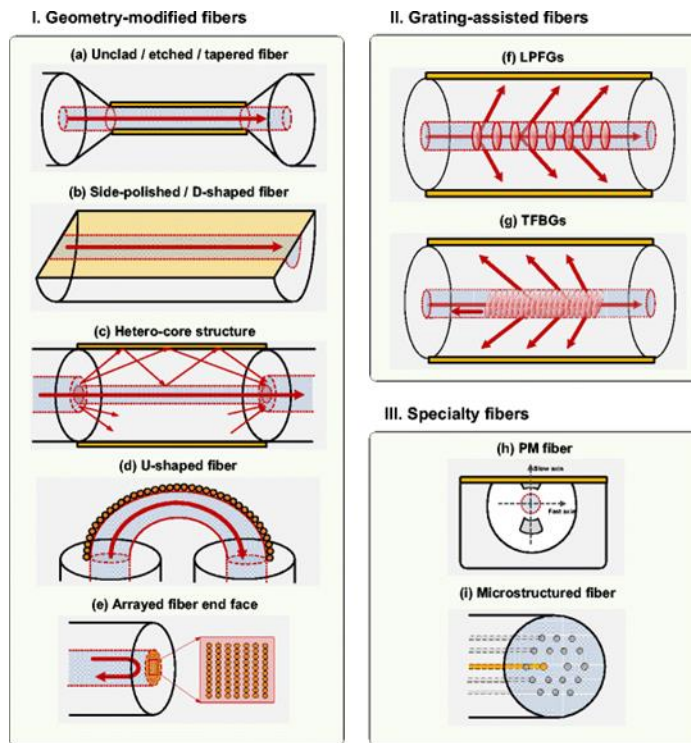
*Figure 2-12: An overview of different structure modified optical fibers. (**I**) Geometry-modified optical fibers: (a) unclad, etched, (b) side-polished, D-shaped fibers, (c) hetero-core structures, (d) U-shaped fibers and (e) arrayed fiber end face. (**II**) Grating-assisted fibers. (**III**) Specialty fibers. Adapted from [50].*

Nevertheless, the major challenge of the first two sensor structures is the low sensitivity for detecting small biomolecules and low analyte concentration. At the same time, such surface modifications as cladding removing, side polishing and fiber tapering leading to the enhanced detection sensitivity suffer from poor mechanical stability and complicated fabrication processes [11,53].

Recently, HC-MOFs or holey fibers with the structure defined by an array of air-channels, running through the whole fiber length, have been extensively studied, using their unique characteristics to create highly sensitive chemical and biological sensors with an application in different fields of biophotonics, chemistry, and life science.

To date, the major efforts in the functionalization of the hollow-core microstructured optical fibers (HC-MOFs) have been aimed at using three techniques: high pressure chemical vapor deposition, direct fiber drawing and layer-by-layer (LbL) assembly [2]. The first two methods are used to form coatings of plasmonic nanoparticles for Raman-microscopy-assisted and optofluidic refractive index sensing [21,61,62] while the LbL assembly allows coatings made of different functional nanoparticles and polymer nanofilms for in-fiber multispectral optical sensing [14] and label-free detection of target analytes [63].

MOF biosensitivity is achieved through the selective adsorption of target molecules onto fiber surfaces, that have been functionalized with antibodies in order to bind to specific antigens which are investigated [14,49–53]. Specific adsorption-based sensors are used for human disease diagnosis and prevention with a sensitivity that meets clinical needs [23,54] (Figure 2.13).
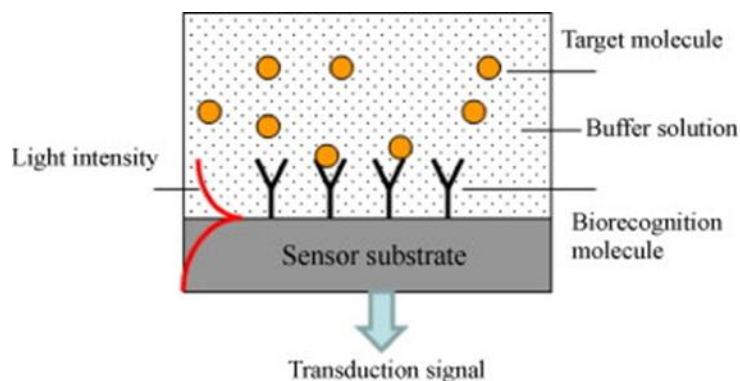
Figure 2-13: The illustration of the concept of label-free optical biosensor [64].

Dinish U.S. et al. reported a novel MOF-based surface-enhanced Raman scattering (SERS) sensor for the detection of cancer proteins in the very low sample volume [65] with a potential of the multiplex detection of biomarkers immobilized inside the hollow core

MOFs [66]. Ultrasensitive measurement of protein was achieved using anti-epidermal growth factor receptors (anti-EGFR) antibody conjugated SERS nanotag (Figure 2.14) and the simultaneous detection of hepatocellular carcinoma biomarkers-alpha fetoprotein and alpha-1-antitrypsin secreted in the supernatant from Hep3b cancer cell line was demonstrated [66]. It has been shown that the proposed detection method was sensitive to the low amount of proteins at ~100 pg in a sample volume of ~10 nL.
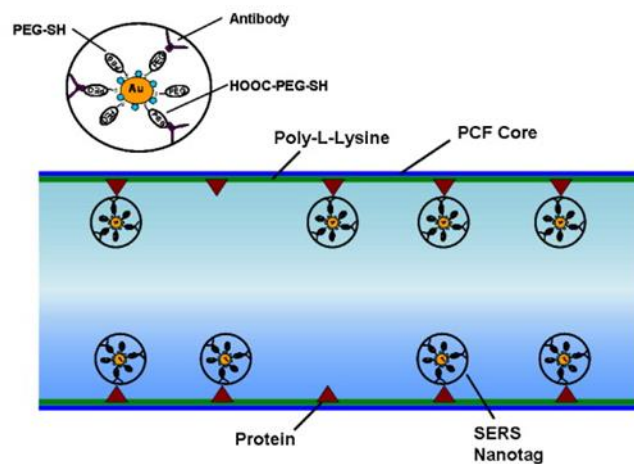
Figure 2-14: The sketch of the functionalized fiber surface showing the binding of anti-EGFR antibody conjugated SERS nanotag to the cancer protein (positive human epithelial carcinoma cells A431) immobilized on the inner wall of the core of MOF [65].

The biological sensors based on modified MOFs have found their applications for the selective detection of DNA. The functionalization of the fiber surface leads to the binding of biological species to the glass surface that is then proved through the measurement of the fluorescence signal created by the labeled sample [67].

Several groups reported feasibility of MOF-based biosensors for DNA detection [68,69]. Ngyuen L.V. et al. proposed that functionalized MOFs can act as a highly specific

DNA sensor and experimentally demonstrated detection of DNA in nanoliter-scale sample volumes [70]. The modification of the fiber surface consisted of a combination of the fuzzy nano assembly technique named also layer-by-layer assembly method [71] and the biotin-streptavidin binding mechanism. The authors showed that the created sensor allows for the detection of DNA solutions at a concentration of 4 µM with the potential for further improvement.

The major advantage of using hollow-core MOFs rather than other techniques based on geometry-modified optical fibers, cuvettes, and bulk optics, lies in combining the long interaction lengths with strong overlap between the light mode, that penetrates deeply into the air capillaries via its evanescent field, and the injected analyte [16]. More practical approaches of using the accessibility of the air capillaries for the functionalization of the MOF surface were shown by Sukhishvili S. et al. on the example of solid and hollow-core MOFs [72]. Basically, the proposed methods combine both the advantages of microfluidics and fiber optics in a single MOF sample allowing light guidance with simultaneous liquid flow inside the hollow capillaries. The authors showed the fine accumulative SERS signal from the full-length Ag-nanoparticle functionalized MOFs as well as the potential for fine control of the density of deposited Ag nanoparticles and studied the SERS gain and light attenuation in the Raman intensity with MOF samples of different lengths [73].

The possibility of integrating colloidal bimetallic nanoparticles with predefined parameters into HC-MOFs was demonstrated by Ponce S. et al. [66]. With the proposed method, PtNi clusters became strongly attached to the inner surface of the hollow-core and

could be used as active catalysts for the hydrogenation of an azobenzene dye, opening new perspectives for *in situ* catalysts monitoring.

An overview of the existing functionalization techniques and applied materials [74], their comparison, and the application areas can be found in References [11,75–79] and Table 2.1 summarizes the reviewed techniques applied for MOFs functionalization, their potential applications and describes the used MOF types including suspended core microstructured optical fibers where the core is effectively suspended in air by thin membranes connected to a robust solid jacket [80].

Table 2-1: Summary of the MOF functionalization techniques and their potential applications [3].

MOF type	Functionalization	Application	Ref.
Suspended core	Selective deposition of different plasmonic nanoparticles into different hollow channels surrounding the central solid core	Simultaneous detection of two different biomolecules	[81]
Hollow-core	Selective filling of core and cladding air channels	Control of the number of guided modes; Single-mode guidance	[82,83]
Hollow-core and suspended core	Functionalization of fiber surfaces with antibodies specific binding to antigens under test	Specific adsorption-based sensors for human disease diagnosis and prevention; Selective adsorption of the target molecules onto fiber surfaces; MOF-based SERS sensor	[65,66]
Suspended core	Combination of the fuzzy nano assembly technique and the biotin-streptavidin binding mechanism; hybridization of immobilized peptide nucleic acid probes	Biosensor for selective DNA detection based on suspended-core MOF	[67–70]
Hollow-core	Silanization of the fiber inner walls	Creation of bio sensitive structure on the example of the covalent binding of horseradish peroxidase to the obtained silanol-modified fiber surface	[84]
Solid core and hollow-core	Finely tuned plasmonic layers of Ag-nanoparticles inside the air capillaries of MOFs; a combination of microfluidics and self-assembled monolayer method, leading to a uniform deposition of silver nanoparticles	Fine accumulative SERS signal from the full-length Ag-nanoparticle functionalized MOFs and fine control of the density of deposited Ag nanoparticles	[73,85–87]

Hollow-core	Integration of colloidal bimetallic nanoparticles with predefined parameters into HC-MOFs	In situ catalyst monitoring	[88]
Suspended core	Gold nanoparticles-functionalized suspended core MOF	Efficient RI sensing featuring the real-time analyte monitoring	[13,89]
Suspended core and exposed core	Functionalization of hollow channels with a monoazacrown bearing spiropyran; attachment of the fluorophore to a polyelectrolyte-coated fiber's surface	Biosensors for the reversible and low volume scale measurement of metal ions; real-time detection of zinc, aluminum and lithium ions	[90–92]
Solid core	Integrated micron-sized Ge wire inside the air channel of modified step-index MOF	In-fiber detector and sensor	[93]
Solid core and hollow-core	Silver metaphosphate/silica step-index fiber and an arsenic trisulphide waveguide embedded in silica produced by pressure-assisted melt filling	Supercontinuum generation	[94,95]
Hollow-core	Doping glass materials with Thulium (Tm) and Erbium (Yb)	Generation of high power CW-lasing and the amplification of nanosecond pulses	[96–98]
Hollow-core	LbL assembly of inversely charged polyelectrolytes and magnetite or silica particles at different diameters	Magnetic resonance imaging of hollow-core MOF; increased effective sensing area and the provision of a convenient scaffold for the binding of specific molecules	[44,99]
Suspended core and hollow-core	Coating with quantum dots on the inner surfaces of hollow channels	Temperature sensor based on modified MOF sample by the CdSe/ZnS nanocrystals; detection of nitric oxide by using an exposed core MOF coated with CdTe/CdS core/shell quantum dots	[100–102]

Sections 2.7 – 2.9 are devoted to the properties of layer-by-layer assembled multilayers.

2.10 Polyelectrolytes

Polyelectrolytes are macromolecules that, when dissolved in a polar solvent like water, have a (large) number of charged groups covalently linked to them, and equivalent numbers of counter ions released to the solvent during the dissolution process [103]. Depending on the sign of charged groups positive or negative the polyelectrolytes can be

divided into two types polycations and polyanions, respectively. These groups dissociate in aqueous solutions (water), making the polymers charged and release the counter ions into the solvent. Therefore, the properties of polyelectrolytes are similar to both electrolytes and polymers. The salts, i.e. the products of a polyacids (polyanions) with a monomeric base and vice versa are called polysalts. Like regular salts, their solutions are electrically conductive and like polymers, their viscosity strongly depends on the molecular weight and polymer concentration. The combination of polymeric and electrolyte behavior gives them many useful properties but also poses problems of characterization [104]. There are strong and weak polyelectrolytes. Strong polyelectrolytes are charged over a wide pH range [105]. Hence, it is a difficult task to manipulate the properties of the assembled film unless one takes specific measures to control the polymer-polymer interactions by adjusting other stimuli such as ionic strength, temperature, and polarity. Unlike strong polyelectrolytes, weak polyelectrolytes are charged only in a smaller pH window; hence, their polymeric conformations can be easily modulated upon changing the pH of the external environment. The unique feature of polyelectrolyte multilayers (PEMs) films assembled from weak polyelectrolytes is that they can be destroyed at extreme pH conditions as the pH-induced charge imbalances in the film overcompensate the attractive polymer-polymer interactions [105,106].

Hong and Decher first proved the concept, i.e. the alternating exposure of a charged planar substrate to solutions of positive (cationic) and negative (anionic) polyelectrolytes [71,107,108]. Provided that each adsorption step leads to charge inversion of the surface,

the subsequent deposition finally results in a layered complex, stabilized by strong electrostatic forces, so-called self-assembled PEMs [108].

2.11 Layer-by-layer assembly

The layer-by-layer deposition method is a powerful and reliable technique used to modify nanostructured materials and surfaces by various functional nanoparticles and multilayers [71,109]. In contrast to other fabrication tools, the LbL assembly offers excellent control and versatility and allows surface functionalization without the need for bulky and expensive laboratory equipment and complicated protocols [110,111]. The sequential deposition of self-assembled multilayers and the adsorption of target nanoparticles ensures the creation of advanced coatings with multiple functionalities in a highly controllable and reproducible way. Nano-scale accuracy of the film thickness of produced structures relies on the number of sequentially deposited cycles and can be tailored [112] by several assembly conditions such as surface charge [113], concentration, ionic strength [114] and pH level [115,116] of the applied solutions.
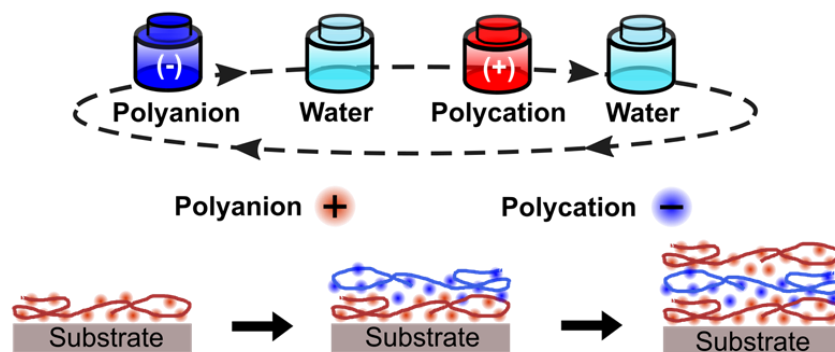
Figure 2-15: Schematic of layer-by-layer assembly of inversely charged polyelectrolytes onto the planar substrate. The immersion into water solution in between the deposition cycles ensures elimination of unbounded particles. The deposition cycles are repeated until the desired number of layers is achieved.

Originally, self-assembled multilayers were developed to modify planar substrates by oppositely charged polyelectrolytes (Figure 2.15) [71], later on, this approach was successfully implemented for the production of various particulate composite structures based on hybrid organic−inorganic multilayers including advanced core-shell models of submicron and nanoparticles [117,118]. Nowadays, LbL engineered structures with a wide range of properties have found their applications in many different fields, ranging from "smart" materials for optics and biotechnology [119] to drug delivery and medicine [118,120,121] and the potential to which this technique can be developed still motivates further research [109,111,122]. Such rapid development has been driven by an extensive choice of available materials and advanced assembly techniques, as well as the utilization of modern film characterization tools [111].

2.12 Stimuli-responsive layer-by-layer complexes

Although these LbL assembled multilayers are often uniform to the naked eye, scale roughness is usually observed under microscopic investigation [123]. For a deposition with a constant thickness increment, the surface roughness increases with the overall number of layers [14,123]. Thus, after substantial height variation, the rough coating appears extra light scattering due to surface topologies on the order of the wavelength of light that results in additional waveguiding losses that are unwanted in some applications based on optical properties of functional coatings [123].

To this extend, postmodification of multilayer films may result in the appearance of novel structures or advantageous structural changes in the film. The surface morphology of polymer layers is usually controlled through postprocessing by "annealing" in aqueous

solutions of different salt concentrations or pH levels. By controlling pH and ionic strength, it is possible to vary the thickness of adsorbed layers from ~1 to ~10 nm or, in some cases, completely prevent the multilayer deposition process [112,124]. Several research groups showed that treatment of polyelectrolyte multilayers in salt solutions caused swelling and led to smoother surfaces showing faster annealing for higher salt concentrations[123,125]. Treatment of multilayers with solutions at varying pH-induced morphological irreversible and reversible changes in both weak polyelectrolytes [106,124] and in H-bonded multilayers [126,127]. The intrinsic property of multilayers composed of weak polyelectrolyte complexes is that they can be destroyed at extreme pH conditions, as the pH-induced imbalance of charges overcompensates the attractive polymer-polymer ionic binding[128].

Sections 2.13 – 2.15 introduce the concept for the creation of sensors based on photonic crystals modified by porous layers.

2.13 1D photonic crystal based sensing

Plasmonic biosensors realized on the platform of one dimensional (1D) photonic crystals demonstrate outstanding performance and sensitivity to detect alteration of the environment refractive index that rank them among the best candidates for different applications [129]. The operating principle of the surface plasmon resonance (SPR) sensor is based on the registration of the resonance associated with the excitation of surface plasmon-polaritons which are electromagnetic waves propagating along the metal-dielectric interface [129]. The spectral and angular positions of this resonance depend strongly on the optical properties of the surrounding medium.

The typical configuration of an SPR sensor is based on the Kretschmann or Otto architecture, both depicted in Figure 2.16. The high refractive index prism is used to match the wavevector of the evanescent wave to the surface plasmon polariton at the interface between the conductor and analyte. In the Otto configuration, the conductive material is pressed towards the prism, with the dielectric-analyte sandwiched between them [130]. In the Kretschmann configuration, the conductor is deposited as a thin film on the prism and the analyte is placed on the top. In both the cases, SPR optical technique measures the refractive index changes in the vicinity of thin metal layers (i.e., gold, silver, or other plasmonic films) in response to the surrounding medium.
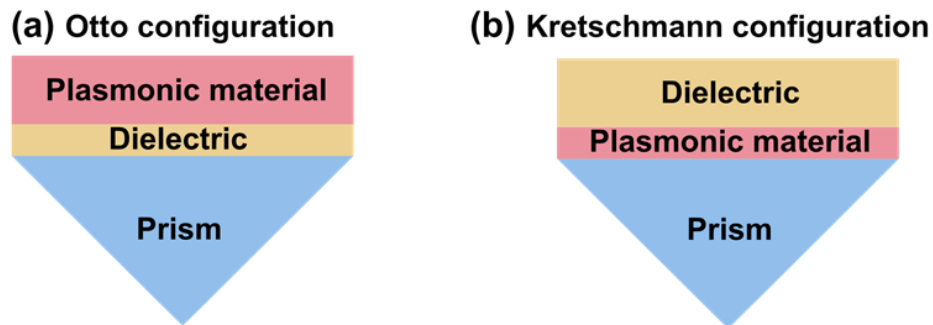
Figure 2-16: In the Otto configuration uses a bulk plasmonic material is separated from the prism by a thin layer of a dielectric analyte. In the Kretschmann configuration, the plasmonic material is deposited as a thin film on the prism, with the dielectric analyte on top. In both cases, the prism is used to match the wavevector of the incident light to the wavevector of the surface plasmon polariton at the interface between the dielectric analyte and plasmonic material. Adapted from [130].

Since the dielectric permittivity of the prism is greater than that of the analyte under test, there is a critical angle at which total internal reflection occurs [131]. At some angle greater than the angle of total internal reflection, a sharp minimum is observed in the reflection coefficient, due to losses in the metal [131].

2.14 Capillary condensation phenomena

Water adsorption technologies have attracted a tremendous amount of interest due to their extensive applications in various research fields [132]. Condensation is the process where water vapor or gas substances become liquid. It is a reversible process to evaporation, where liquid water becomes a vapor. Gases can condense according to three different mechanisms: in the air (homogeneous nucleation), on the surface (heterogeneous nucleation) and inside the pores. However, gas condensation in the pores occurs at the lowest partial gas pressures [133]. The pore diameter, where capillary condensation takes place, can be calculated via Kelvin equation (Eq. 2.14):

$$ln\frac{p}{p_0} = -\frac{2\sigma V_l}{\gamma_m RT},$$
$$(2.14)$$

where p is the vapor partial pressure, p_0 is the saturated vapor pressure, σ is the surface tension, V_l is the molar volume of the liquid, R is the universal gas constant (8.314 J mol^{-1} K^{-1}), γ_m is the Kelvin radius of the mesopores, and T is Kelvin's temperature.

As mentioned above, the condensation process depends on the pore size, which in turn depends on the size of the individual particle forming the porous layer. For example, for a pore of 3 nm, the size of the spheres forming such a pore should be 25 - 30 nm. And for a micropore size of 17 nm, the diameter of the spheres should be 150 - 180 nm.

2.15 Opal-like photonic crystals

Photonic crystals are periodic optical nanostructures that influence the propagation of light by their periodic variation in dielectric contrast or refractive index with periods on the scale of visible light wavelengths [134]. Photonic crystals exist throughout the natural world from opal gemstones and beetles to bird feathers and butterfly wings with the common characteristic between all is their iridescent color [134]. Traditionally, researchers

have used two methods to fabricate photonic crystals: nanolithography and self-assembly of colloidal crystals [135]. The self-assembly of colloidal crystals is the preferred way as it is a simple and inexpensive technique. This can yield crystalline samples of a few to several hundred structural layers thickness. The approach involves crystallization of a colloidal suspension of monodisperse spheres of silica, polystyrene or polymethylmethacrylate to form a material with a three-dimensional periodic structure in which 24% of the volume is air (a colloidal crystal or opal). Photonic crystals exist throughout the natural world from opal gemstones and beetles to bird feathers and butterfly wings and the common characteristic between all is their iridescent color [136].
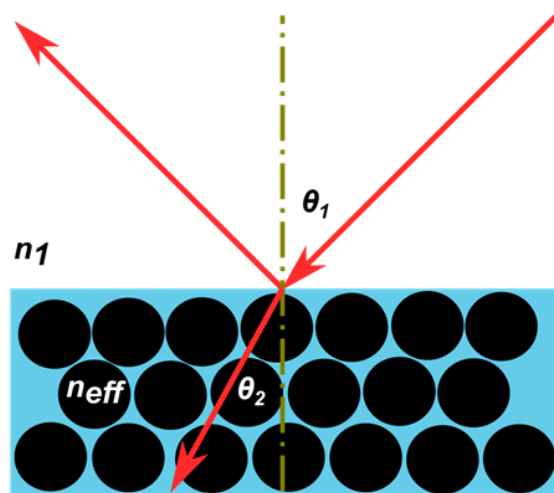
Figure 2-17: Schematic outlining the interaction of light with the periodic material (opal-like photonic crystal) with an effective refractive index, and the light scattered by the sphere planes. θ_1 and θ_2 are the angles between the normal to the sample surface and the direction of the incident and refracted light beams, respectively; n_{eff} and n_1 is the effective refractive index of the photonic crystal and the external medium, respectively. Adapted from [134].

A modification to Snell's law for refraction of light between media of dissimilar refractive index, and Bragg's law for optical diffraction can be used to describe the

wavelength-dependent 'structural color' observable in colloidal opals or opal-like photonic crystals. As outlined in Figure 2.17, the opal film is formed as a multilayer of two media with different refractive indices (n_1 is typically denoted to vacuum, air or a liquid, and n_{eff} that of the photonic crystal. In the case of constructive interference of diffracted photons, Bragg's law for 1D structures can be written as (Eq. 2.15) [134]:

$$m\lambda_m = 2n_{eff}dcos\theta_2 \tag{2.15}$$

where m is the resonance order, d is the interplanar spacing defining the centroids of the spheres.

The effective refractive index, n_{eff}, of the photonic crystal (Eq. 2.16) depends on the refractive index of the embedded particles ($n_{particles}$), the refractive index of surrounding media, n_{medium}, ($n_{air} = 1$) and the packing density, f, (for an ideal close-packed structure of spheres $f = 0.7405$) [137]:

$$n_{eff} = \sqrt{n_{particles}^2 f + n_{medium}^2(1 - f)} \tag{2.16}$$

The corresponding Snell's law criterion for the light incident at an angle θ_1 can be expressed as (Eq. 2.17):

$$n_1 sin\theta_1 = n_2 sin\theta_2 \tag{2.17}$$

Thus, the angle-dependent diffraction or wavelength can be written in terms of the incident angle generally as the Bragg–Snell law (Eq. 2.18):

$$m\lambda_m = 2d\sqrt{n_{eff} - sin^2\theta_1}. \tag{2.18}$$

Bragg–Snell law takes into account refraction of light in the composite structure and the incident angle of the incoming light [134,136]:

3. Chapter 3. Functionalized optical fibers

Experimental and theoretical results obtained in the scope of this Ph.D. thesis are presented in the following chapters. Chapter 3 covers the surface functionalization of HC-MOFs and the material and optical characterization of the produced structures, including an overview of the different environmental conditions while LbL assembly with their specific advantages and disadvantages. Loss analysis of functionalized HC-MOFs concludes the fabrication chapter. Chapter 4 introduces silica particles functionalized photonic crystal-based sensors. Chapter 5 is devoted to different post-processing techniques directing to the smoothing of the original films and the creation of biocompatible and removable nanocoating. In chapter 6, refractometric measurements based on the set of functionalized are presented on the example of bovine serum albumin (BSA) at different concentrations.

3.1 Introduction

To date, the major efforts in the functionalization of HC-MOFs have been aimed at using three techniques: high-pressure chemical vapor deposition, direct fiber drawing and LbL assembly. The first two methods are used to form coatings of plasmonic nanoparticles for Raman-microscopy-assisted and optofluidic refractive index sensing [2,21,61,62] while the LbL assembly [71] allows coatings made of different functional nanoparticles and polymer nanofilms for in-fiber multispectral optical sensing [14] and label-free detection of target analytes [63]. Despite the challenges of coating fabrication on a non-conventional substrate formed by curved fiber surfaces, LbL assembled multilayers were successfully applied for the functionalization of different kinds of OFs [138] with the materials which

were traditionally not used in fiber optics [3]. Depending on the coating function, that can be either buffer layers with a predefined value of surface potential [113] for selective capture of target particles and better adsorption of specific molecules and functional nanoparticles [63,65,66] or the complete bioresponsive layers [139] with predefined released characteristics.

Diverse fiber structures give a rise to various deposition approaches, differing by location of host materials integration. Functional films can be deposited onto both the outer surface [139] and the inner regions of hollow capillaries of MOFs as well as onto the fiber tip. In both cases, the produced films became a key feature of functionalized OFs since they control and dictate interactions of the guided light with the surrounding environment that defines the optical properties of modified OFs [111].

Among the variety of produced structures, HC-MOFs, which consist of air channels running along their whole length, represent an attractive playground for the creation of multifunctional in-fiber optical sensors [14]. The major advantage of HC-MOFs lies in combining the long interaction length with strong overlap between light and the analyte within small sample volumes, giving rise to high sensitivity [11]. Thus, any variations in the composition of the fiber surface and/or the filled media can be detected by measuring the shifts of maxima and minima in the transmission spectrum of HC-MOF [11]. The feasibility of the LbL assembly technique for an accurate coating of fiber capillaries with polymer nanofilms consisting of polyelectrolyte multilayers and creation of HC-MOF-based multispectral optical sensor was recently demonstrated [14]. Furthermore, experimental conditions can be adopted to load submicron silica particles into the central

hollow-core of MOFs which were initially modified with polyelectrolyte multilayers [99] serving as a substrate for particle adsorption. However, LbL functionalization of the inner surface of the light-guiding hollow-core induces additional fiber losses. This remains negligible for thin films and does not significantly disturb light guidance inside the fiber as long as the number of bilayers is limited [14]. Nevertheless, extra light scattering due to surface features on the order of the wavelength of light decreases the sensitivity at a single or multiple wavelengths followed by a spectral broadening of any type of optical resonances [99].

3.2 Motivation

Spectral properties of HC-MOFs are defined in the fabrication step and are mainly depend on the refractive index of glass material and the thickness of the first cladding ring. Thus, due to the limited number of accessible materials satisfying the fiber optics needs, variation of the capillary thickness has been found as the only way to control the optical properties of HC-MOFs. However, reproducibly drawing fiber families with slightly different thicknesses ($\Delta \sim 10$ nm) of the first cladding ring is technically quite a challenging task that would inevitably increase the cost of fiber production. Therefore, the postprocessing technique that could tune in a reproducible and highly controllable way the transmission windows in both visible and IR-spectral range through the modification of the fiber surface is highly disirable. In the next section, this issue has been addressed by presenting a simple and inexpensive technique applied for surface functionalization. This allows a small increase in the thickness of capillary walls leading to production of several

MOFs with slightly shifted transmission windows that were originally drawn from the same preform [14].

However, any modification of the internal structure of fiber capillaries changes the conditions for the light guidance since any imperfections (defects) and height variations featuring rough surfaces give a rise to extra scattering losses. Therefore, the analysis of transmission losses in the functionalized fibers is required to study the effect of such modification on light propagation. All the previously published works disregard this evaluation which is crucial for understanding the limitations of functionalization from the point when it has a negligible effect to the case of complete disruption of light guidance. Here, a detailed study of the light propagation in functionalized fibers with polymer nanocoating at different thicknesses has been performed.

Besides, all the previous works on this topic have demonstrated sensing functionalities of MOFs for capillaries with smooth walls [3,11]. In this contribution, the technique for HC-MOFs coating with chemically and mechanically stable, monodisperse submicron silica particles by the layer-by-layer deposition approach has been developed. The proposed method of MOF functionalization allows one to reach novel sensing capabilities, including an increase in the effective sensing area, providing a convenient scaffold for the attachment of long molecules such as proteins, and combining in-fiber liquid sensing and high-performance liquid chromatography [140]. The surfaces, which are covered with closely packed spherical particles, can also serve as promising sensitive elements of gas sensors [141] due to capillary condensation in the gap formed with particles in contact.

3.3 Materials and methods

3.3.1 HC-MOF samples

The reported HC-MOFs were produced by a stack-and-draw method described in [142]. Three concentric capillary layers surround the central hollow-core and define the overall fiber structure. The geometrical features of the HC-MOF are detailed in Figure 3.1.
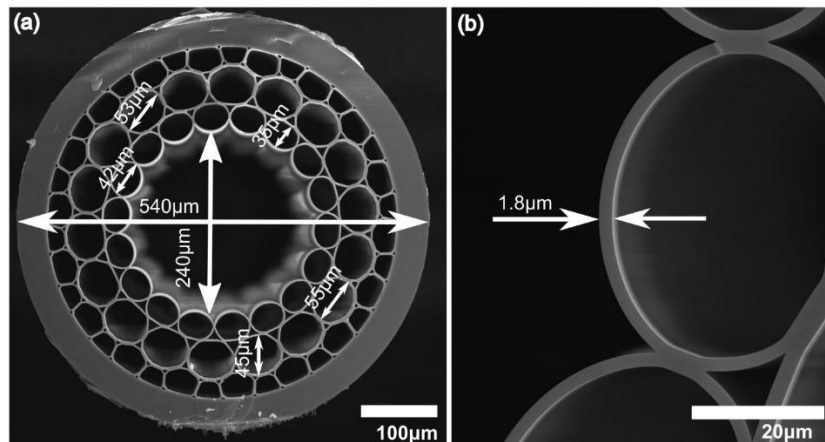
Figure 3-1: SEM images of the HC-MOF used in the experiments. (a) General view. (b) Wall thickness of the central capillary.

The wall thickness of the capillaries forming the first cladding layer was ~1.8 μm, the diameter of the hollow-core was ~240 μm, and the outer diameter was ~600 μm. Such a fiber structure supports multimode guidance. Spectral properties of HC-MOFs have been discussed in detail in [6,143].

The optical dispersion of glass material is illustrated in Figure 3.2.
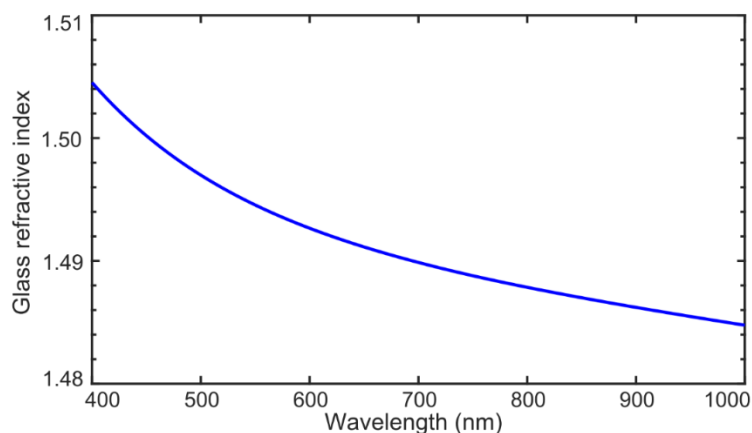
Figure 3-2: Optical dispersion of the fiber glass used for fabrication of investigated HC-MOFs.

The numerical analysis of the guiding properties at the similar structures can be found at references [144–146].

3.3.2 Chemical reagents

All applied PEs were purchased from Sigma-Aldrich: poly (allylamine hydrochloride) (PAH) (MW = 50,000), poly (styrene sulfonate) (PSS) (MW = 70,000), poly (diallyldimethylammonium chloride) (PDDA) (MW = 400,000 – 500,000) and polyethylenimine (PEI) (MW = 2,000,000). Chemical structures of the applied polyelectrolytes are illustrated in Figure 3.3.
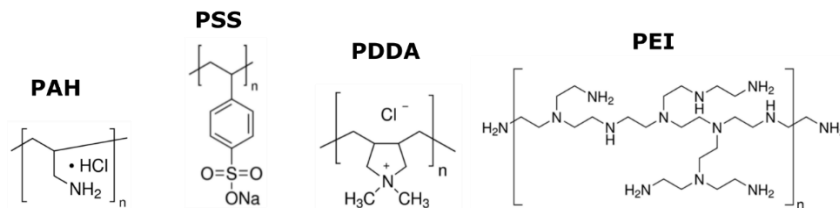
Figure 3-3: Chemical structure of the polyeletcrolytesused for the creation of functional coatings (PAH - poly (allylamine hydrochloride), PSS - poly (styrene sulfonate), PDDA - poly (diallyldimethylammonium chloride) and PEI - polyethylenimine).

60

Magnetic nanoparticles (MNPs) were prepared by chemical precipitation from a solution of $FeCl_3$ and $FeCl_2$ salts under sodium hydroxide [147]. Super monodispersed silica nanoparticles were prepared by using the multistep method described in Reference [148]. Deionized water was produced by a Millipore Milli-Q Plus 185 system.

3.3.3 Multilayered deposition process

The basic principle of our approach is the LbL assembly of oppositely charged PEs onto the glass surface. Figure 3.4 shows the setup used for coating the fiber capillaries [99].
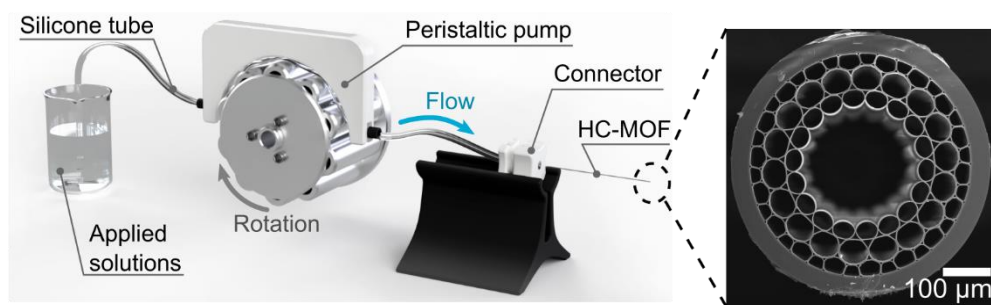
Figure 3-4: The setup for functionalization of HC-MOFs with LbL assembly. A peristaltic pump drives the flow of applied solutions (polyelectrolyte water solution, silica particles colloid solution, magnetite particles colloid solution and pure water) through the full fiber length, leading to the formation of the polymer coating on the inner surface of the core capillary. The procedure is repeated to create the desired number of bilayers. The insets depict the scanning electron microscopy (SEM) images of the fiber end face. Adapted from [14].

The peristaltic pump creates a flow of PE solutions through the fiber with a controllable and persistent rate for a pre-determined volume. This procedure results in the uniform deposition of PE layers inside the fiber capillaries. As polyelectrolytes, aqueous solutions of polycationic PAH, PEI or PDDA and polyanionic PSS [149] have been used.

As functional materials, silica submicron particles at different diameters and magnetite nanoparticles were incorporated into polymer substrate formed by PE multilayers [99,150].

Prior to PE layer assembly, the fibers were washed with deionized water for 2 min with a speed of 500 μL min^{-1} to ensure that small dust particles were removed; then, the fibers were subjected to the LBL technique by a combination of inversely charged PEs and/or functional particles. The very first deposited PE layer consists of polyethylenimine (PEI) serving as an adhesive or anchor agent that provides a high surface charge density with a homogenous distribution due to its high molecular weight and branched structure [151,152]. Then, three material combinations were used to finalize the LbL assembled nanocoating. First is the combination of inversely charged PE solutions consisted of PAH and PSS which were prepared in water buffer and in the presence of 0.15 M NaCl. The second combination includes the positively charged PDDA polyelectrolyte and negatively charged silica particles at different submicron diameters. As the third set of applied materials, polycationic PAH and polyanionic magnetite nanoparticles has been applied for the LbL assembly. Deionized water was applied after each deposited layer of functional materials with a speed of 200 μL min^{-1} for 2 min to wash the samples and to remove unadsorbed molecules. This setup was used to modify the fibers with a length of 6 cm, however, potentially based on the same strategy the longer sample can be also functionalized successfully.

The other possible material combinations used for the creation of advanced functional coatings onto fiber capillaries are discussed in Refs. [2,3,72,84,139]

3.3.4 Optical transmission of functionalized MOFs

Optical measurements of MOFs samples were performed by the transmission setup based on CCD-spectrometer Ocean Optics QE Pro operating in the extended wavelength range and a broadband light source - Thorlabs SLS201L halogen lamp. The light was launched into a MOF sample by the 10X Olympus objective and the output signal was collected by the 10X Olympus objective and then send to the spectrometer for spectral analysis (Figure 3.5). Thus, the size of fiber hollow-core in the range of ~240 µm allows the easy focusing of the incoming light by 10X objective minimizing the coupling losses.
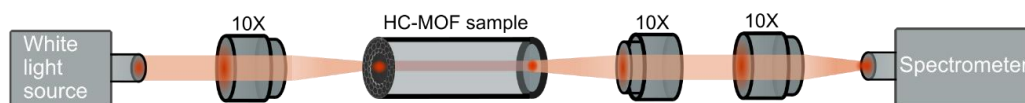
Figure 3-5: Schematics of the transmission measurement setup. 10X denotes a 10X Olympus objective.

For the near-IR spectral domain, Ocean Optics QE Pro spectrometer has been replaced by a NIR spectrometer with 900 – 1700 nm wavelength range (NIRQuest, Ocean Optics, USA). In this case, silica-based auxiliary fiber cables (Art photonics GmbH, Germany) with 200/220 µm core/cladding diameters and 600/660 µm were utilized for the delivery of lamp illumination and the collection of light transmitted through MOF samples, respectively. To ensure the effective face-to-face connection between auxiliary fibers and MOF samples, the waveguide end faces were sealed into special SMA terminators and mounted into SMA/SMA connection sleeves, enabling their optical alignment. Measurements in the mid-IR spectral range were conducted with a Fourier-transform infrared (FTIR) spectrometer, operating in the broad spectral domain from 1.45 to 20 µm (Matrix-F, Bruker, Germany). Chalcogenide IR-fibers 180/280 µm and polycrystalline IR-fibers 240/300 µm (both supplied by Art photonics GmbH, Germany) were used for the light delivery in the ranges 1.1 - 6.5 µm and 3 - 18 µm, respectively. Chalcogenide 500/550 µm and polycrystalline IR-fibers 900/1000 µm (both supplied by Art photonics GmbH, Germany) ensured the effective light collection.

3.4 Results and discussion

In this section, the designed coatings are characterized from both structural and optical points of view. Scanning electron microscopy (SEM) images of the fiber cross-sections help to evaluate the morphology of produced structures; average thickness and roughness are extracted based on the analysis of different fiber parts. Transmission spectra measurements of functionalized fibers allow tracking the shift of the transmission windows during the multicycle coating formation. The cut-back method is performed for the analysis of the waveguiding losses induced by deposited layers.

3.4.1 Morphology of PAH-PSS multilayers

It has been shown for the planar substrates that the thickness of LbL assembled coatings is linearly proportional to the number of deposited layers [153,154]. Moreover, the thickness of LbL-assembled layers on a planar substrate is proportional to the square root of the ionic strength that, in turn, is the square function of the molar concentration of ions [155]. Hence, the ionic strength is typically supported by sodium and chlorine ions. For example, the thickness per single layer is 1.3 ± 0.1 nm at 0.05 M NaCl but is 2.2 ± 0.1 nm at 0.5 M NaCl [155]. In addition, the higher concentration of sodium chloride gives rise to an increased roughness caused by altering the molecular conformation from a linear to globular structure [14].

To gain insight into the impact of the solution ionic strength on the coating performance, thickness and morphology of assembled PAH/PSS films with PEs at the same concentration dissolved in deionized water and in buffer containing 0.15 M NaCl were studied systematically. Figure 3.6 shows the thickness of the coatings prepared by the

64

alternating deposition of PAH and PSS layers from PE solutions with and without NaCl as a function of the number of deposited PE bilayers. The coating thickness linearly depends on the number of assembled PAH/PSS bilayers. However, the average thickness increase is 1.8 ± 0.3 nm and 7.0 ± 1.3 nm per bilayer for the salt-free PE solutions and in the presence of 0.15 M NaCl, respectively. These values differ from previously published data for LbL coating of planar substrates, where the average thickness per PE layer was ~1–3 nm [154,156,157]. This discrepancy is attributed to different hydrodynamic conditions for PE adsorption in our study and the effect of the charged capillary surface. An increase in the film thicknesses with increasing ionic strength in the PE solutions was also observed. This result is in good agreement with previously published works on the LbL coating of planar substrates.
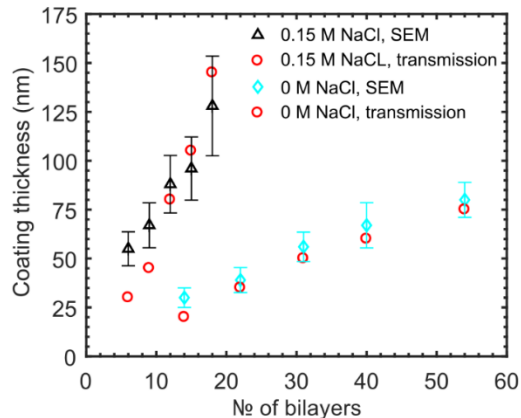
Figure 3-6: Polymer coating thickness versus the number of PE bilayers. The thickness is fitted to obtain the coincidence of the minima positions for both the experimental and calculated transmission spectra using MATLAB software (Equation 2.13). The thickness of polymer coating was extracted by SEM analysis of dried samples. Error bars show the coating roughness. Adapted from [14].

The thickness of fiber coating was evaluated from SEM micrographs of the HC-MOF cross-section (as showed in Figure 3.6 above) and adjustment of the polymer coating

thickness in the theoretical transmission model to get coincidence with the experimental transmission spectrum (Figure 3.7). Both approaches are in good agreement with each other.
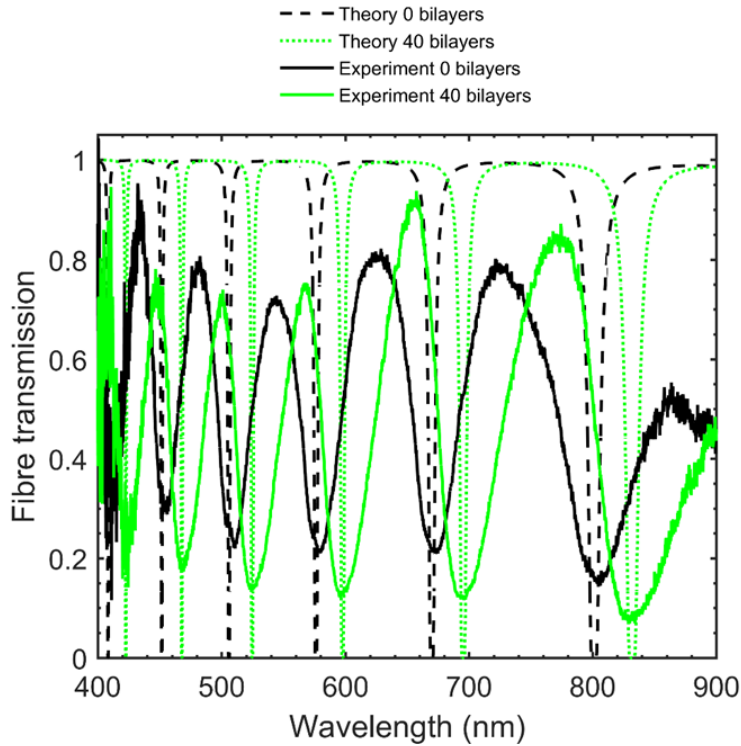
Figure 3-7: Comparison of the experimental fiber transmission spectra with the theoretical ones obtained by adjusting the thickness of the polymer coating (60 nm per 40 polymer bilayers) [14].

The stability of the polymer coating has been validated under various conditions [14]. First, the fiber transmission spectra in 1 day and in 4 months after coating were compared. No degradation was revealed except for slight variations in the spectral positions of the minima and maxima, which, however, do not exceed 3 nm. This effect has been attributed to a tiny reduction of the coating thickness caused by drying due to changing ambient humidity. Next, the stability of PE layers was checked at various temperatures (from 22 °C to 120 °C). The value of 37 °C has been chosen as the closest one to the normal body temperature, 60 °C corresponds to an average temperature for protein, 80 °C and 90 °C lye near the glass transition temperature for PAH/PSS layers (similar to rearrangement of PAH/PSS multilayers at capsules) and 120 °C is the temperature that results in

evaporation of unbound (free) water. The fiber transmission spectra show that the polymer coating has not been influenced or damaged. Finally, the stability of PE layers with respect to various pH levels and the ionic strength of the sample liquid was verified. The measurements show that the polymer coating remains stable since there are no spectral shifts in fiber transmission in the wide range of pH levels from 4 to 10 as well as concentrations of NaCl up to 1M which is suitable for the majority of bioanalytical applications. So robust stability with respect to various conditions manifests that any adsorbed molecules can be just washed out at denaturation conditions and the functionalized HC-MOFs can be reused again.

3.4.2 The structure of silica particle-based fiber coating

LBL deposition is based on alternative adsorption of oppositely charged polyelectrolytes and silica particles. The very first layer includes three polyelectrolytes PEI/PSS/PDDA. Then four PSS/PDDA bilayers were applied to finalize the formation of the buffer layer aimed at strong adhesion for SiO_2 particles. SiO_2 particles with diameters of 300 nm, 420 nm and 900 nm have been utilized in the experiment [99]. The final concentration for all samples of the silica particles was equal to 12.8 mg/mL and was measured by the dry residue method.

Silica nanoparticles of diameters 300 nm and 420 nm homogeneously cover almost the full surface of the core capillary after a single layer is deposited (Figure 3.8).
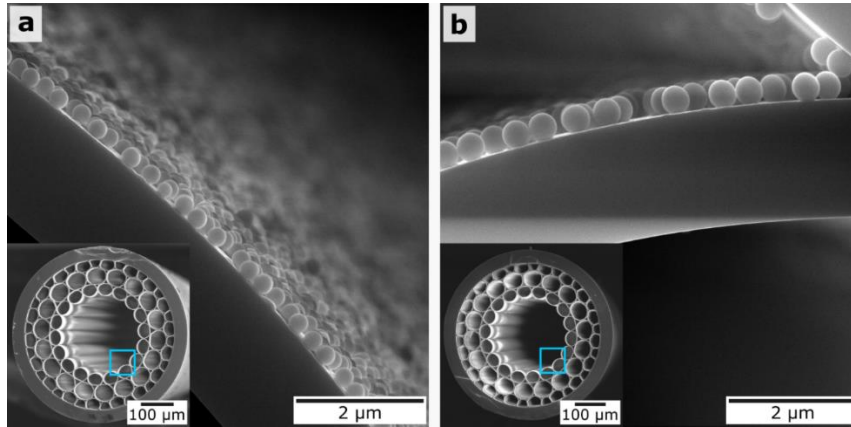
Figure 3-8: SEM images of MOF end faces and magnified capillary surfaces. (a) MOF sample after deposition of one layer of 300-nm silica particles. (b) MOF sample after deposition of one layer of 420-nm silica particles [99].

In contrast to smaller particles of 300 nm and 420 nm, the bigger silica particles of 900-nm form layers on both sides of the first cladding ring (Figure 3.9).
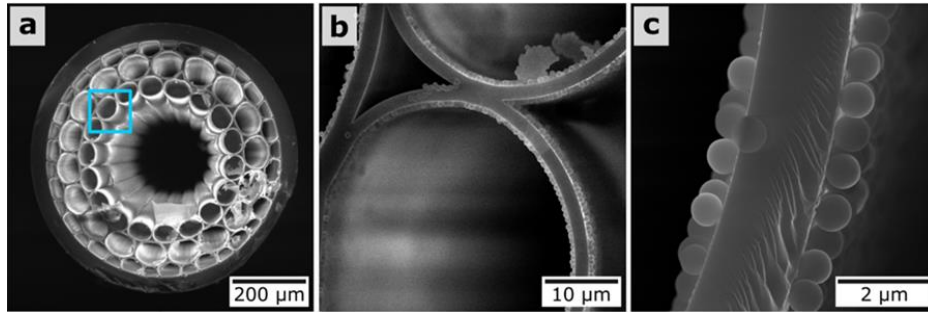
Figure 3-9: SEM images of MOF end face (a) and magnified capillaries (b,c) with one deposited layer of 900-nm silica particles [99].

This can be explained by Stoke's law. The viscosity force *F* which describes particle flow inside the capillaries is proportional to their size and velocity (3.1):

$$F = 6\pi\mu R\upsilon, \tag{3.1}$$

where μ is the dynamic viscosity, R is particle radius, υ is the flow velocity.

The bigger silica particles are affected by the stronger viscosity force (Eq. 4), leading to slowing them down and, as a result, to a higher chance of their adsorption onto capillary walls. This is well-illustrated by the clear difference between the deposition of small (300-nm and 420-nm) and large (900-nm) silica particles. In the first case, particles

68

adhere to the internal surface of the central capillary only; where is in the second case particles additionally adsorb to the first layer capillaries.

Next, MOF coating with three deposited layers of 300 nm silica nanoparticles has been analyzed (Figure 3.10). It should be noted that silica particle adsorption to a buffer polyelectrolyte layer is more efficient than deposition of the second and the third SiO_2 particle layers. The intermediate PDDA layer applied between silica particles serves as a recharger and is deposited to improve the adsorption of silica particles. However, due to small thickness of a single PDDA layer (in the range of 3 nm), the deposition of the intermediate PDDA layer between the silica particles does not create the necessary substrate layer contributing to the following adsorption of silica particles.
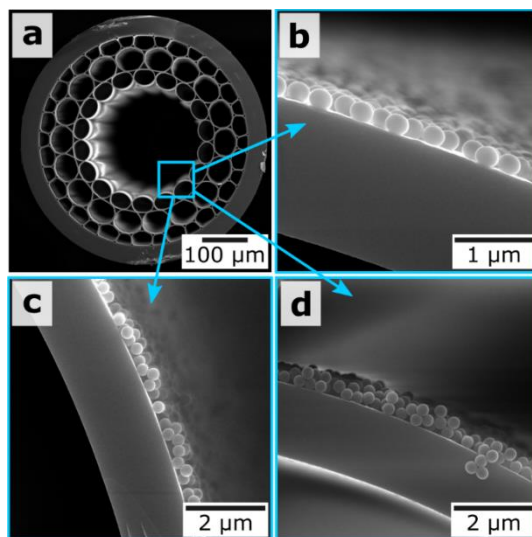
Figure 3-10: (a) SEM image of MOF end face; (b,c,d) magnified SEM images of capillaries with one, two and three deposited layers of 300-nm silica particles, respectively [99].

To increase the concentration of adsorbed silica particles for multilayer deposition, the effect of intermediate polyelectrolyte layers has been studied and the two material combinations have been compared: single PDDA layer and combination of PDDA/PSS/PDDA applied between SiO_2 particles. The triple polyelectrolyte layer was chosen to form the necessary thickness for better silica particle adsorption. The higher concentration of SiO_2 particles deposited on the core surface is shown in Figure 3.11.
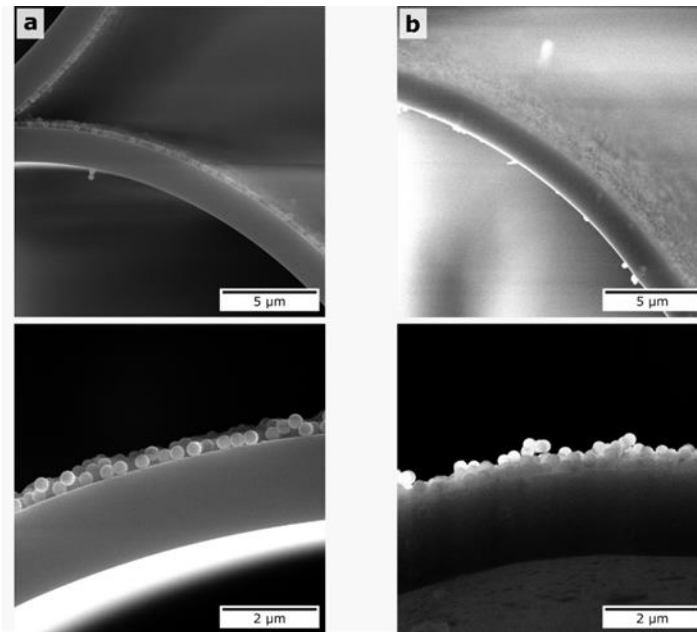
Figure 3-11: SEM image of MOF capillaries with two layers of 300-nm SiO$_2$ nanoparticles for the cases of (a) PDDA/PSS/PDDA and (b) PDDA intermediate layers, respectively at different magnifications top and bottom [99].

SEM images of MOF hollow-core regions proved the concept of silica layer formation and showed the higher particle concentration for two deposited layers with a triple layer of PDDA/PSS/PDDA than the silica concentration with a single PDDA layer deposited.

3.4.3 Magnetite-based nanocoating for functionalization of microstructured optical fibers

A simple and cheap method of making HC-MOFs visible in magnetic resonance imaging (MRI) has been introduced in the example of fiber coated with magnetite-based nanoparticles which pave the way for combing MRI and optical bioimaging [44]. The proposed approach is based on the LbL assembly of oppositely charged polycationic polyelectrolytes and polyanionic magnetite nanoparticles (MNPs) on the inner core surface of HC-MFs. In this work, the formation of the composite nanocoating has been studied further for the increasing number of deposited bilayers. From SEM images of MOF cross-sections focusing on the inner surface of the hollow-core, one can observe the clear formation of the nanocoating resulted from the deposition of PEs and MNPs (Figure 3.12).
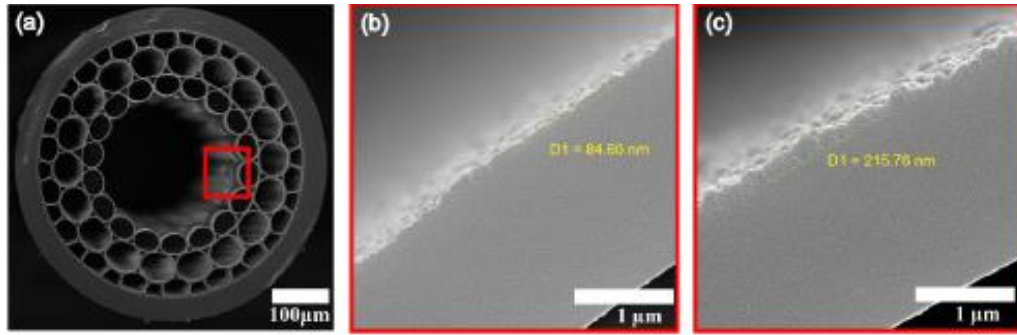
Figure 3-12: (a) SEM image of MOF end face with the highlighted region of the inner surface of the hollow-core. (b,c) Magnified regions of the capillary walls illustrating the formation of composite nanocoating on the example of MOF samples modified with (b) 13 PAH/MNPs bilayers and (c) 28 PAH/MNPs bilayers [150].

The average thickness of the coating formed by the deposition of 13 PAH/MNPs bilayers is equal to 85 nm and the one for the sample modified with 28 PAH/MNPs bilayer is 216 nm.

3.4.4 Optical characterization of HC-MOFs functionalized by polymer multilayers

HC-MOF functionalization with an nm-thick polymer coating leads to fine-tuning of their optical transmission windows, as shown in Figures 3.13 and 3.14. Specifically, shifts in maxima and minima of the transmission appear to be almost a linear function of the number of deposited bilayers for both the buffer combinations (in salt-free PE solution and in the presence of 0.15M NaCl). This fact results from the similar RIs of the fiber glass [158,159] and PAH/PSS [160,161]; thus, polymer coatings can be considered an effective instrument to vary the thickness of the core fiber capillary.
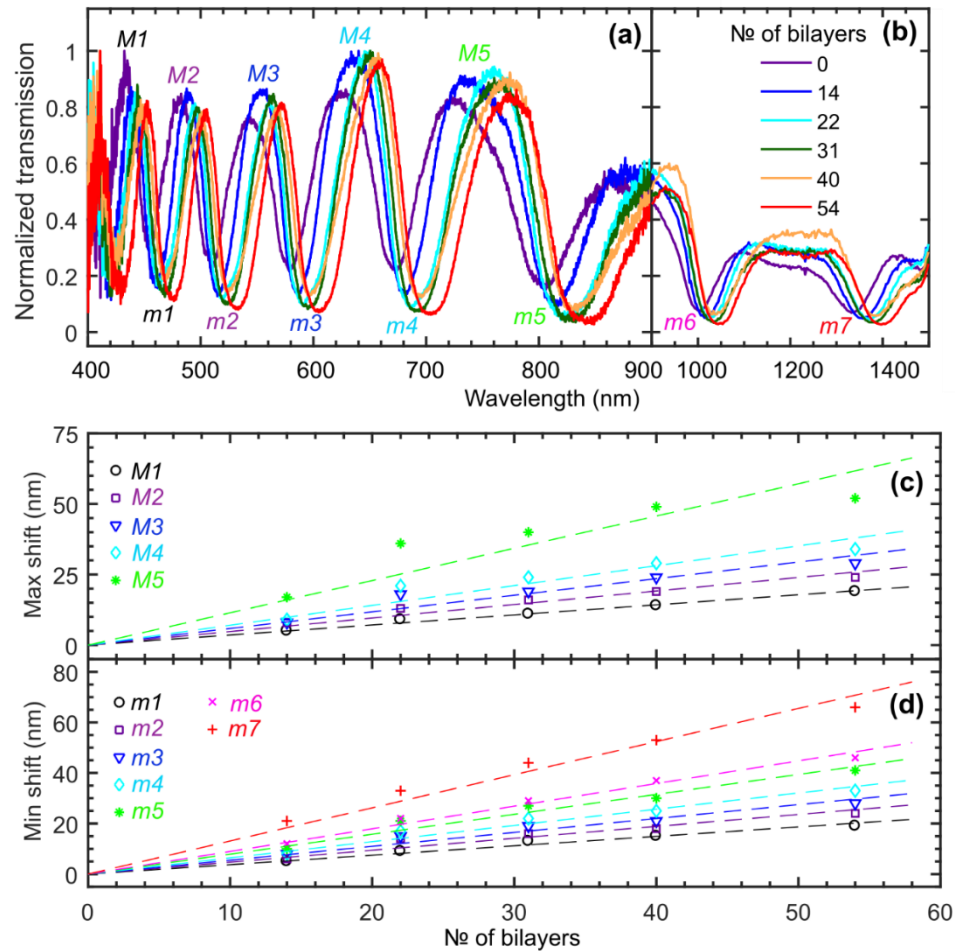
Figure 3-13: Optical characterization of HC-MOFs functionalized by PEs adsorbed from the salt-free buffer (see Fabrication chapter). (a,b) Transmission spectra in the visible (400 nm – 900 nm) and near-infrared (900 nm – 1500 nm) ranges. M1 – M5 and m1 – m7 designate positions of maxima and minima, respectively. The results for 6 samples with various numbers of PE bilayers are presented. Note the different scales along the x-axis for (a) and (b). Shifts of maxima (c) and minima (d) of the transmission along with the linear fits. The length of all the samples was 6 cm. Adapted from [14].
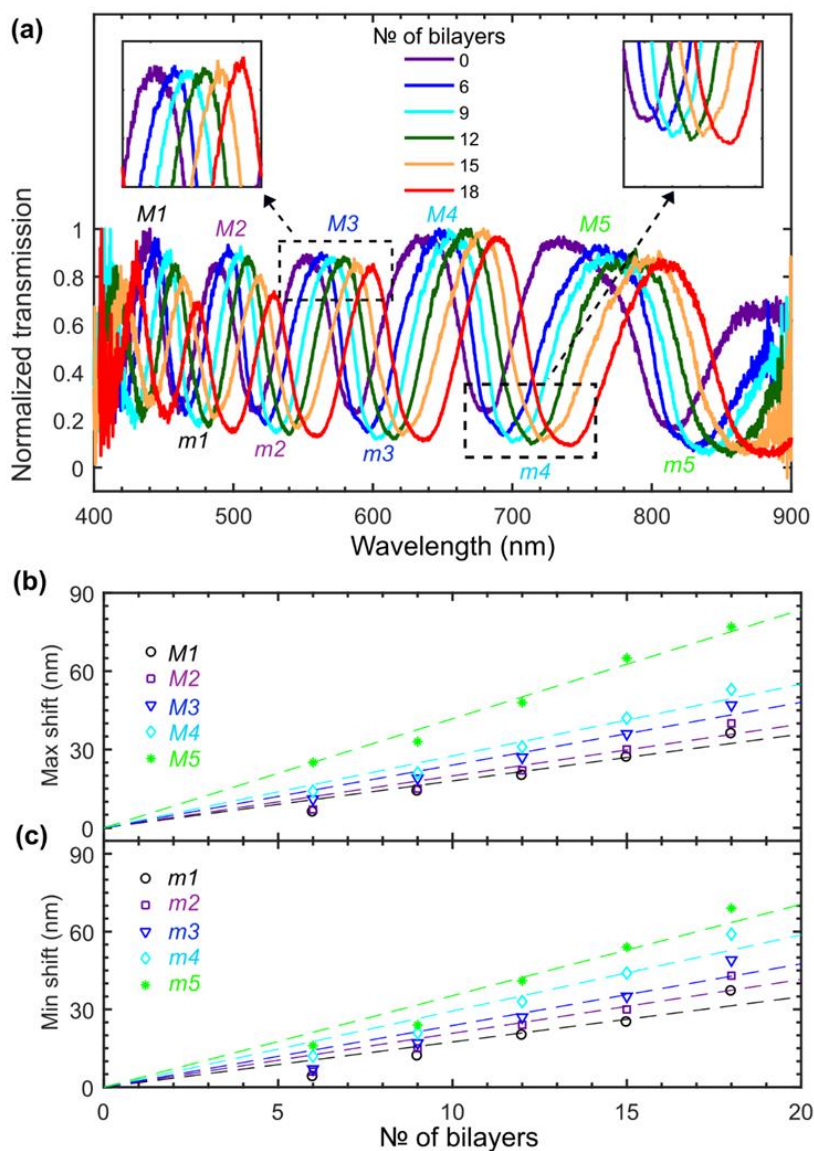
Figure 3-14: Optical characterization of HC-MOFs functionalized by PEs dissolved in saline buffer (0.15 M NaCl). (a) Transmission spectra in the visible range. The results for 6 samples with a different number of PE bilayers are presented. Shifts of maxima (b) and minima (c) of the transmission along with the linear fits [14].

However, LbL functionalization results in additional transmission losses. The results of cut-back measurements for the samples modified in the salt-free PE solution are presented in Figure 3.15. One can observe that the polymer coating leads to an average extra attenuation of ~0.02 dB cm^{-1} per single assembled PAH/PSS bilayer. However, this

73

issue does not significantly disturb light guidance inside the fiber as long as the number of bilayers is limited.
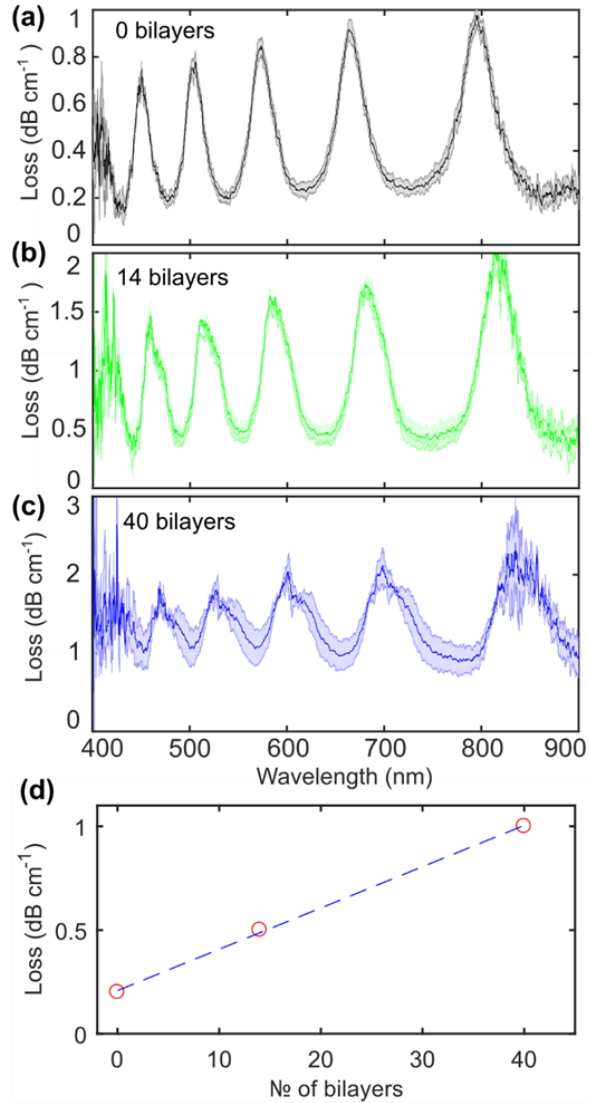
Figure 3-15: Characterization of optical losses in functionalized HC-MOFs by the cut-back technique. (a) Unmodified MOF. Fibers coated with 14 (b) and 40 (c) PE bilayers in the salt-free solution. Shadow areas show the error range. (d) The minimal optical losses in the transmission windows (400 – 900 nm) as a function of the bilayer quantity. The analysis of the losses induced by deposited PE layers was performed by the cut-back method. The light was coupled into the fibre, and four cut-back steps were performed with a 6-cm-long sample under fixed coupling. Adapted from [14].

3.4.5 Optical characterization of HC-MOFs functionalized by silica particles

Figure 3.16 exhibits transmission spectra of MOFs coated with the buffer layer only and 300-nm and 420-nm silica nanoparticles. Deposition time and flow rate were equal for SiO_2 particles of both sizes. A layer of silica nanoparticles impacts on the position of optical resonances (Eqs. 2.12 and 2.13) similarly to the polymer layers, i.e. they induce the redshift of transmission spectra of functionalized MOFs. Experimentally measured spectral shifts agree with this explanation and are in good agreement (see Table 3.1) with the ones calculated from Equations 2.12 and 2.13 for the deposition of 300-nm and 420-nm silica particles and the effective thickness of applied layers of 106 nm and 125 nm, respectively.
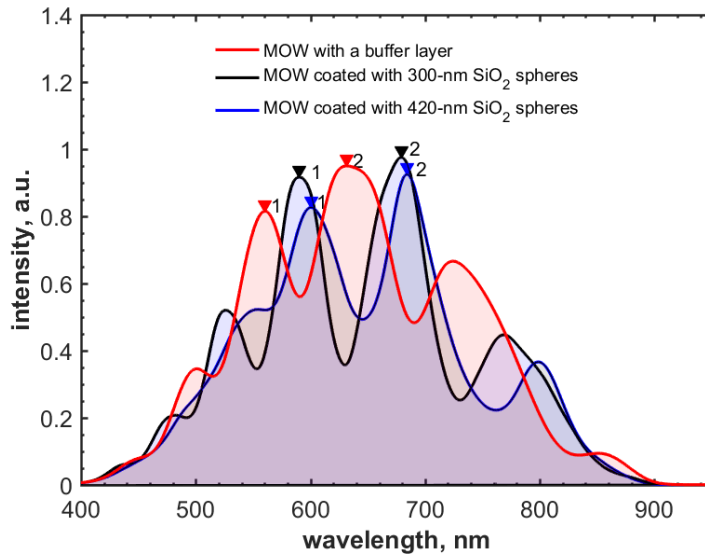
Figure 3-16: Spectral shift of transmission bands for MOF samples with one deposited layer of 300-nm and 420-nm SiO₂ particles into MOFs with an internal buffer layer. The length of all the fibers was 6 cm. Adapted from [99].

Table 3-1: Transmission peaks shift of MOF samples with one deposited layer of 300-nm and 420-nm SiO₂ particles [99].

	Spectral shift measured, nm		Spectral shift calculated (Equation 2.13), nm	
Peak number	300-nm SiO₂	420-nm SiO₂	300-nm SiO₂	420-nm SiO₂
peak1	31 ± 2	38 ± 2	33	39
peak2	39 ± 2	45 ± 2	38	45

It is instructive to note that the adsorption of nanoparticles of different (larger) size leads to deterioration of the shape of the MOF transmission curve as a result of strong light scattering. For example, MOF coating by a suspension of 900-nm silica nanoparticles leads to significant changes of the spectral shape (Figure 3.17).
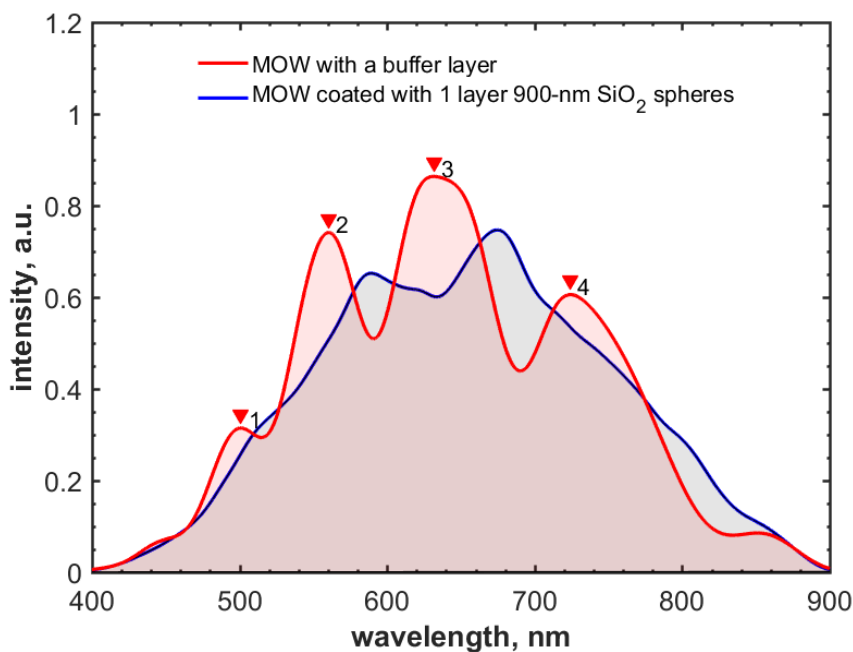
Figure 3-17: Transmission spectrum of MOF sample with one deposited layer of 900-nm silica particles (blue). MOF spectrum with a buffer layer (red) [99].

Such double coating of silica particles on the first cladding ring (Figure 3.17) results in the disappearance of the Fabry-Perot anti-resonances, associated with local bands in the transmission spectra.

Next MOF coating with three layers of 300 nm silica nanoparticles has been analyzed (Figure 3.18). It should be noted that silica particle adsorption to a buffer polyelectrolyte layer is more efficient than deposition of the second and the third SiO_2 particle layers. The intermediate PDDA layer applied between silica particles serves as a recharger and is aimed at their better adsorption. However, due to its small thickness (in the range of 3 nm), fewer silica particles are adsorbed. This effect is illustrated in Figure 3.18 where the highest spectral shift was measured for the first deposited silica particles layer (Table 3.2).
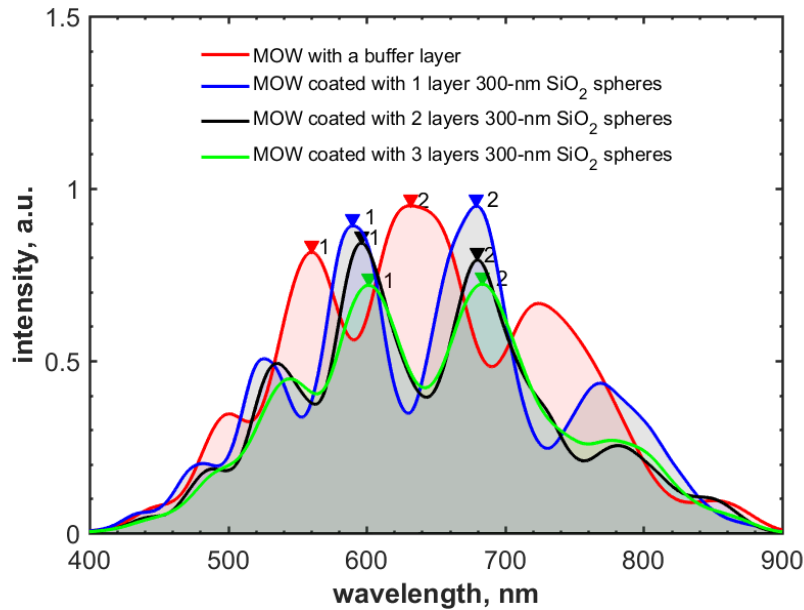
Figure 3-18: Transmission spectra for MOFs coated with the buffer layer only (red) and with one (blue), two (black) and three (green) layers of 300-nm SiO₂ particles [99].

Table 3-2: Spectral shift of local transmission bands for MOF samples with multiple deposited silica particle layers. The diameter of silica particles is 300-nm [99].

	Spectral shift, nm		
Band number	1 layer	2 layers	3 layers
peak1	31 ± 2	37 ± 2	42 ± 2
peak2	39 ± 2	42 ± 2	46 ± 2

3.4.6 Optical characterization of MOFs functionalized by composite multilayers

Optical transmission and fiber losses of HC-MOF samples functionalized by composite nanocoating formed by polyelectrolytes and magnetite nanoparticles have been also studied (Figure 3.19a). Thus, the set of MOF samples modified with a different number of PAH/MNPs bilayers was investigated and the position of maxima located near 550 nm was tracked down (Figure 3.19b).
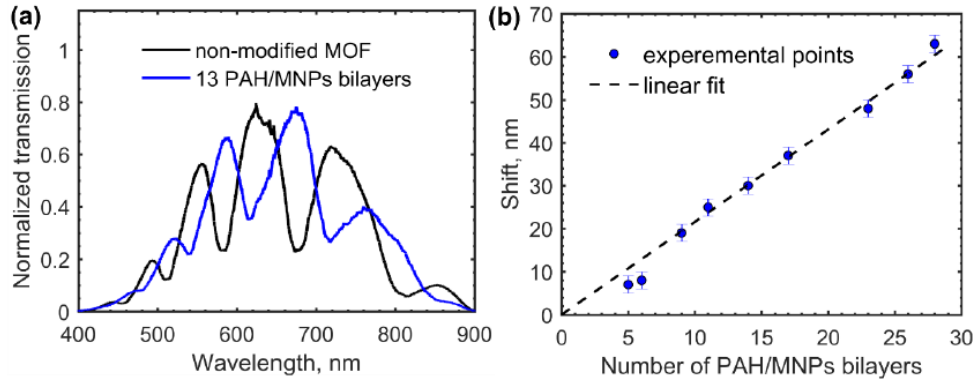
Figure 3-19: (a) Comparision on transmission spectra of non-modified and modified MOFs. (b) The spectral shift of the maximum transmission spectrum located at 550 nm induced by the deposition of composite nano-coating on the inner surface of MOF hollow-core. The dashed line shows the linear fit of the experimental points. The error bars correspond to the spectrometer's optical resolution. Adapted from [150]*.*

3.4.7 Demonstration of mid-IR guidance in designed HC-MOFs

To finalize optical characterization mid-IR guidance has been demonstrated. Figure 3.20 summarizes the results of transmission spectra measurements and loss analysis of investigated MOFs. The broadband guidance was observed from 400 nm to 14 µm (where signal-to-noise ratio was adequate) with clearly defined optical resonances in the mid-IR spectral domain and minimum loss of ~1 dB cm^{-1} (2 - 4 µm transmission window) (Figure 3.20). Minimal losses in the near-IR region were observed in 0.8 - 1 µm transmission window and were equal to ~0.6 dB cm^{-1}. Although the produced waveguides suffered from high material absorption beyond ~7 µm, clearly defined optical resonances in the wide wavelength range of 400 nm – 6.5 µm can open previously unreachable horizons for the soft glass-based MOFs applications.

Using the general transfer matrix method and taking into account the model of the Fabry-Perot resonator [44], the resonance positions of the investigated HC-MOFs have been calculated (Equation 2.13) using MATLAB software referring to the minima of transmission spectra.
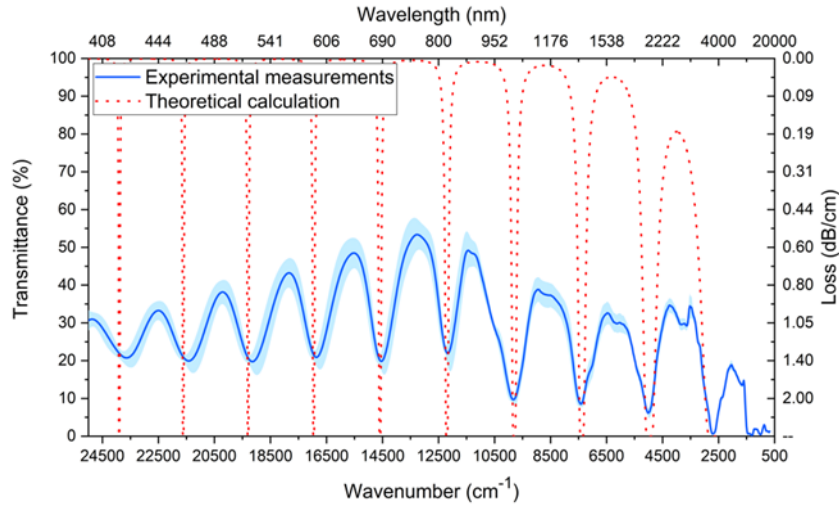
Figure 3-200: Demonstration of broadband VIS – mid-IR light guidance. Blue curve states for the transmission spectrum of investigated MOFs, the shaded region illustrates the estimated loss interval summarizing the results of 4 samples of MOFs. The red dotted line is the calculated spectrum referred to the positions of minima in MOFs transmission (Equation 2.13) [10].

A comparison of the designed borosilicate soft glass-based HC-MOFs and previously reported works is given in Table 3.3, emphasizing the microstructured and holey waveguides. HC and SC state for hollow- and solid-core, NC F means negative curvature fiber. Very few works report the effective fabrication and mid-IR guidance with HC-MOFs made from soft glasses. Russell et al. [162] achieved photonic bandgap guidance with soft-glass hollow-core PCF in the range of 750 – 1050 nm. Other groups concentrated on soft glass solid-core PCFs and achieved broadband transmittance up to 3 µm [163–165]. Dianov et al. succeeded in the production of silica negative curvature fibers and demonstrated mid-IR transmittance up to 7.9 µm [166]. Despite high material absorption in the IR spectral domain, several research groups received outstanding results in the fabrication of silica-based hollow-core fibers for mid-IR applications [33,167].

Table 3-3: Comparison of the optical performance of reported microstructured optical fibers [10].

Waveguide type	Material	Guidance, nm	Loss	Authors	Year
HC MOF	soft glass	400 – 6500	1 dB/cm	This work [10,142]	2020
HC PCF	soft glass	750 – 1050	0.74 dB/m	Russell et al. [162]	2011

79

SC PCF	soft glass	900 – 2300	2 – 5 dB/m	Klimczak et al. [164]	2014
SC PCF	soft glass	350 – 3000	-	Russell et al. [163]	2006
SC PCF	soft glass	800 - 2600	-	Klimczak et al. [165]	2014
NC HC F	silica	2500 - 7900	50 dB/km	Dianov et al. [166]	2013
HC PCF	silica	2900 - 3250	2.6 dB/m	Knight et al. [168]	2005
NC HC MOF	silica	>3500	1 – 10 dB/m	Dianov et al. [169]	2011
HC PCF	-	1450 - 2100	6.5 dB/km	Zhang et al. [167]	2019
HC PCF	silica	1400 - 2300	9.5 dB/km	Roberts et al. [170]	2009
HC PCF	silica	3100 - 3700	0.05 – 0.13 dB/m	Richardson et al. [33]	2014
HC F	silica	3000 - 4000	34 dB/km	Knight et al. [171]	2012
3D HC MOF	polymer	3500 – 500	10 – 25 dB/mm	Talataisong et al. [172]	2018
Kagome HC F	silica	1000 - 3000	10 – 14 dB/km	Richardson et al. [173]	2017
SC PCF	ZBLAN	200 - 2500	-	Russell et al. [174]	2015

3.5 Summary

In this chapter, layer-by-layer assembly of polymers and/or inorganic nano- and submicron particles has been successfully adapted for the functionalization of the inner surface of HC-MOFs. A detailed explanation of the experimental techniques along with the necessary study of the coating performance versus the number of deposited bilayers confirmed the concept of high level of control and repeatability of produced structures. we have adapted the LbL technique to accurately coat fiber capillaries with polymer nanofilms. The effect of salt presence in the applied PE solutions on the coating performance has been considered. In contrast to the salt-enriched PEs, the salt-free PE solutions yield the smallest roughness and coating thickness per single bilayer. The average thickness increasing of 1.8 ± 0.3 nm and 7.0 ± 1.3 nm per PAH/PSS bilayer for the salt-free PE solutions and in the presence of 0.15 M NaCl, respectively, has been observed [14]. Thus, the polymer coating leads to an average extra attenuation of ~ 0.02 dB cm^{-1} per single assembled PAH/PSS bilayer formed in salt-free PE solution [14]. The proposed LbL deposition technique can be extended further, allowing one to reach novel sensing capabilities including HC-MOF functionalization by specific molecules to capture biomolecules (DNA, antibodies, aptamers, Fab, etc.) and target particles.

For the first time to our knowledge, the LBL technique for HC-MOF modification through the deposition of silica particles with different sizes (300, 420, and 900 nm) onto capillary surfaces has been presented [99]. The potential for the creation of multilayer

porous coating was demonstrated on the example of one, two, and three layers of 300-nm silica particles. The largest spectral shift in the transmission is induced by the first deposited silica layer (31 nm and 39 nm, for the first and the second transmission bands, respectively), while additional silica layers are worse-adsorbed on the first layer of particles, resulting in the additional transmission spectral shifts (11 nm and 7 nm). Additionally, the synergy of MRI and optical fiber-based endoscopic probe was presented in HC-MOFs functionalized with magnetite nanoparticles [150].

Additionally, the transmittance of investigated HC-MOFs was characterized in a broad spectral range. Effective light guidance in the spectral region of 400 nm - 6.5 μm with the minimum loss of ~0.6 dB cm^{-1} in the near-IR spectral domain (0.8 - 1 μm transmission window) and minimum loss ~1 dB cm^{-1} in the mid-IR region (2 - 4 μm transmission window) was observed [10].

4. Chapter 4. Silica particles functionalized photonic crystal based sensor

4.1 Motivation

In a commercial SPR biosensor configuration, incident light is employed by using a high-reflective index glass prism in the Kretschmann geometry (Figure 2.16b). The defined SPR angle, at which resonance occurs, is dependent on the refractive index of the material of the metal surface. Consequently, when there is a small change in the refractive index of the sensing medium (e.g., through biomolecule attachment or gas condensation on the sensor surface) the surface concentration of the analyte can be quantified by monitoring the reflected light intensity or tracking the resonance angle shifts. Typically, an SPR biosensor has a detection limit on the order of 10 pg mL^{-1} [175].

In this work, the combination of 1D SPR photonic crystal and the LBL assembled submicron silica particles is introduced [176]. The deposition of the silica spheres on the sensor surface creates the porous structure which covers homogeneously the sensitive area. Gases can condense according to three different mechanisms: in the air (homogeneous nucleation), on the surface (heterogeneous nucleation) and inside the pores. Taking into account that the gas condensation in the pores occurs at the lowest partial gas pressures [133], the designed functional coating allows increasing the detection limit of the modified SPR sensor. Development of a sensor is based on silica spheres of various diameters, as well as of different nature - hydrophobic and hydrophilic. Detection is based on measuring the parameters of the sensitive layer, such as the refractive index and thickness, of a layer consisting of silica particles and condensed gases.

4.2 Experimental section

4.2.1 The structure of the photonic crystal

The 1D photonic crystal consists of alternating Ta_2O_5/SiO_2 layers deposited onto a silica substrate using the technique of atomic layer deposition. The detailed parameters of fabricated samples are as follows. The widths of SiO_2 layers in the photonic crystal are 270 nm and Ta_2O_5 layers - 155 nm plus the most external additional waveguide SiO_2 layer with

a thickness of 370 nm. The widths of all layers, as well as the number of pairs of alternating layers, see Figure 4.1.
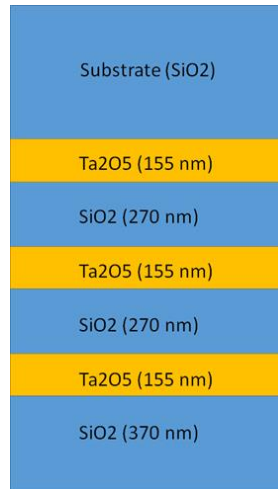
Figure 4-1: The scheme of the photonic crystal providing the resonance at 780 nm.

These specific values were selected to optimize the ultralong surface plasmon propagation conditions for the case when the structure is exposed to laser radiation at 780 nm. Hydrophilic and hydrophobic silica submicron particles were deposited on the waveguide layer, creating a developed surface and promoting the adsorption of matter on the waveguide layer of the photonic crystal, which makes it sensitive to the presence of water vapor and gases of different nature contacting with the sensor.

The described structures are designed in such a way that the waveguide mode can be effectively excited in the silica waveguide layer, and due to the small thickness of this layer (370 nm), the electromagnetic field of this mode is quasi-surface in nature, thus, it effectively penetrates the adsorption-selective layer, providing high resonance sensitivity to changes, associated with the adsorption or condensation onto the sensor surface. Therefore, the center of resonance associated with the excitation of the waveguide mode shifts along the wavelength and angle.

4.2.2 Calibration of fabricated structures

The experimental setup comprises the laser diode, the plasmonic heterostructure (1D photonic crystal) placed onto the BK-7 glass prism and the CMOS matrix (IDS UI-3360CP-M-GL) having the 2048×1088 pixel screen with the sizes

11.264 mm × 5.984 mm and pixel size 5.5 μm [129]. Laser light is focused onto the crystal surface in such a manner that the central angle of incidence corresponds to the resonant surface plasmon excitation angle in the Kretschmann scheme. Angular interrogation is used: light reflected from the heterostructure surface forms a divergent beam which without any focusing is detected by the CMOS matrix.
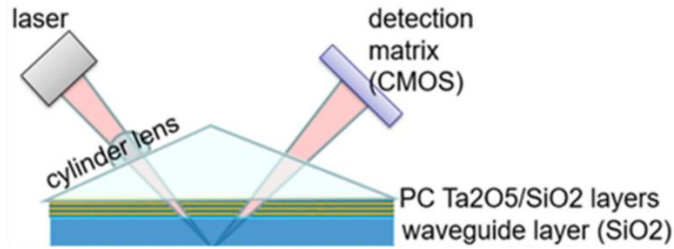
Figure 4-2: Schematic representation of the experimental setup.

After fabrication, the photonic crystals were tested without silica porous coating with water ($n = 1.33$) covering the whole sensor surface. It allowed to measure the reflectance spectra and to determine the structure quality itself, without the influence of the possible differences in silica coating quality. All 8 fabricated photonic crystal structures showed equally good resonances under the illumination of 780 nm laser light (Figure 4.3).
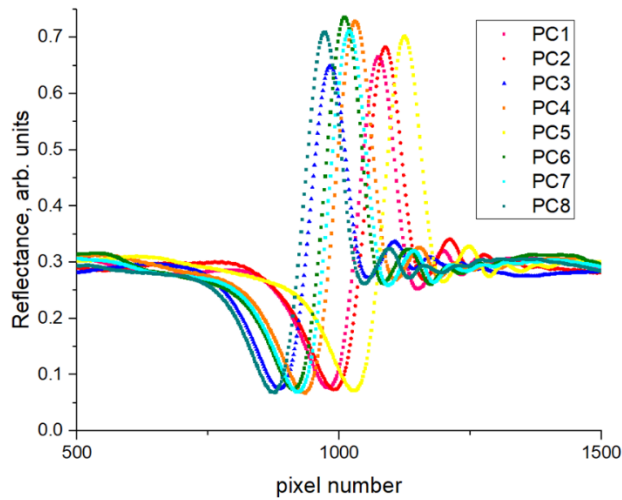
Figure 4-3: Reflectance spectra of 8 fabricated PC samples. The same shape denotes equal sensitivity of the samples.

Some small shifts observed for experimental curves corresponding to different samples are due to the changes of the experimental conditions (temperature, surface

cleaning quality, etc.) rather than due to the difference in the structures themselves. All curves have the same angular width that corresponds to nearly equal sensitivity of the photonic crystal-based structures. The oscillatory angular pattern implies that in the absence of the nanoparticle coating, the excited quasi surface wave is long-range propagating. The origin of such a pattern is the interference of the light, reflected from the structure and the light, transferred in the quasi surface mode, and then coupled back via prism to radiation propagating collinearly to the reflected light.

4.2.3 Silica particles coating on the surface of photonic crystal

Deposition of the hydrophilic silica particles onto the surface of photonic crystals ensures the creation of porous functional layer supporting condensation of water and water-soluble gases at the lower partial gas pressures comparing to planar (smooth) surface. Silica particles form the pores at two interfaces which are the particle-particle and particle–photonic crystal contact (Figure 4.4).
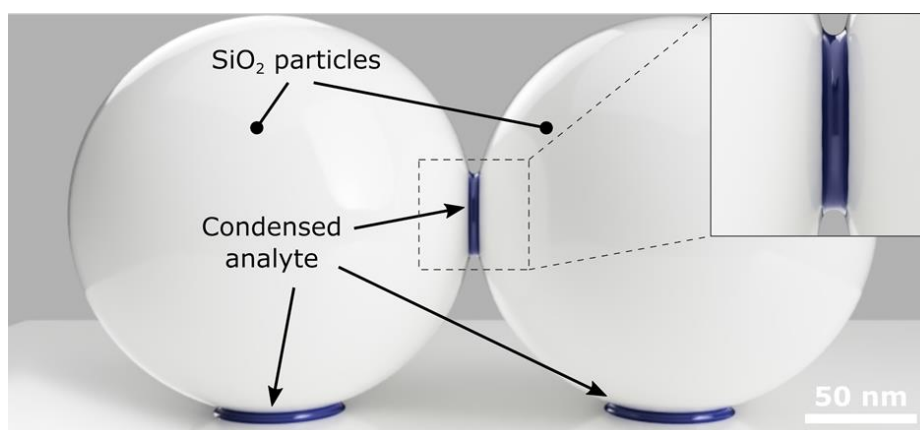
Figure 4-4: Schematic of an area of analyte condensation between 180 nm particles and substrate (under normal conditions).

The important thing is the analysis of the effect of particle size on the amount of condensed gas (the volume of recovered liquid). For this study, the volume of condensed analyte into pores between particles and substrate was calculated for silica particles of different sizes (available after the synthesis). A total amount of condensed analyte per unit area was calculated using the equation (Eq. 4.1):

$$V_{total} = N_{particles}(V_1 + V_2) \qquad (4.1)$$

where V_{total} - the total volume of the condensed analyte, $N_{particles}$ - number of particles per unit of area, V_1 - volume of condensed analyte between particles, V_2 - volume of condensed analyte between the particle and the substrate (photonic crystal).

It has been found, that the total amount of condensed analyte between 180 nm particles and the substrate is 1.6 times higher than one between 300 nm particles and substrate. Based on the obtained data and possible particle variants, silica particles with a diameter of 180 nm were chosen as optimal for further experiments.

The formation of silica coating onto the surface of photonic crystals consists of three main stages: sample cleaning, preparation of the substrate and adsorption of silica particles. The deep coating method (Figure 4.5) has been chosen due to its versatility, reproducibility and simplicity.
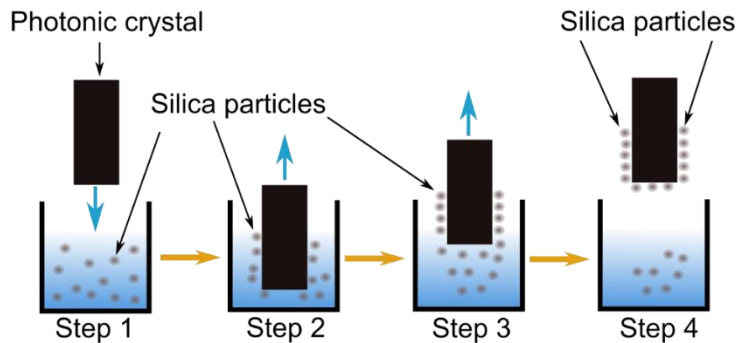
Figure 4-5: Schematic of dip-coating technique.

At the cleaning stage, it was shown that for effective cleaning, it is necessary to treat the crystal with an acid solution, alkaline, as well as a mixture of organic solvents (toluene, acetone, alcohol). Next, the crystal is processed in plasma for 1 minute on each side (longer processing is not possible due to the instability of the coating of the photonic crystal). For adsorption of hydrophobic silica particles, the surface of the photonic crystal needs the pre-hydrophobization.

The morphology of the resulted hydrophilic and hydrophobic surfaces is presented in Figure 4.6. It can be seen from the SEM images that the hydrophobic coating is more uniform than the hydrophilic one. Optical measurements based on the produced structures are provided in the next section.
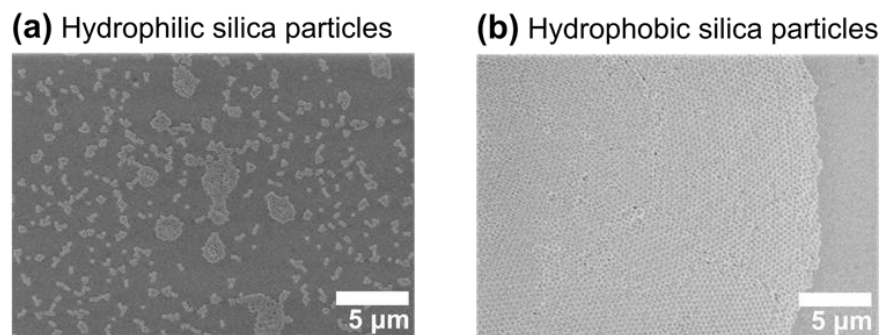
Figure 4-6: SEM images of photonic crystal surface prepared by the dip-coating method: (a) – hydrophilic and (b) - hydrophobic.

4.2.4 Optical characteristics of water condensation on the sensor surface

The gas circulation setup contains a sealed chamber made from poly(methyl methacrylate), a membrane pump, and fitting for optical gas sensor. These units are connected by silicone tubes. The commercially available humidity meter (Center 311 rs 232, Center Technology corp.) has been used for temperature and humidity monitoring. The schematic of the experimental setup is illustrated in Figure 4.7.
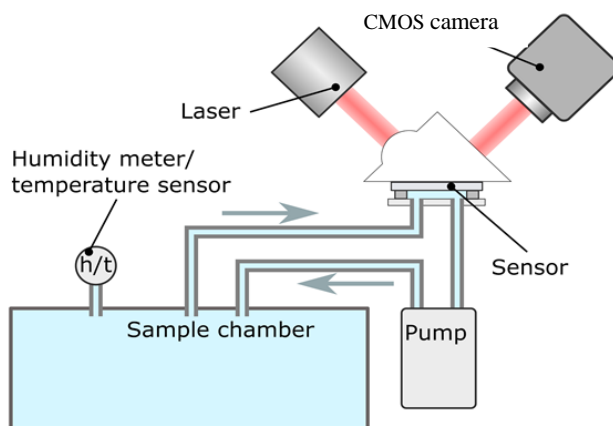
Figure 4-7: Experimental gas circulation setup.

To demonstrate the sensing capability of the produced structures, the response to both water condensation and changing humidity has been recorded for the photonic crystals functionalized with hydrophilic and hydrophobic silica particles.

As can be seen in the graphs, the response to humidity changes is different for the photonic crystals coated with silica particles of different nature (Figure 4.8).

87
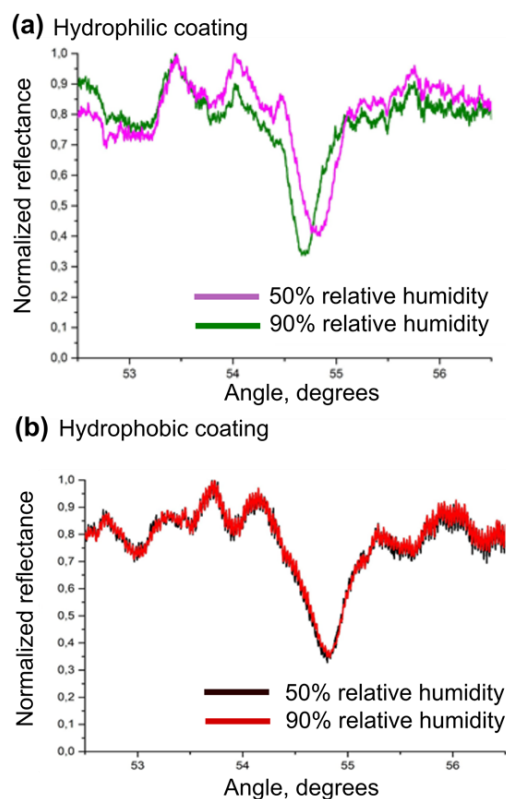
Figure 4-8: Dependence of reflection on an angle for (a) – hydrophilic and (b) – hydrophobic coatings.

The hydrophilic system has been shown to detect changes in humidity. It was established, that responses to humidity are significantly higher for hydrophilic particles in comparison with hydrophobic ones. The main advantage of the proposed sensor structures is the potential for the realization of multiple-zones sensitive surfaces based on hydrophilic and hydrophobic particles. Also, the designed coating allows the relative humidity detection in a wide range starting from ~5% and up to 95%. Moreover, the stability of the signal on the hydrophobic part makes it possible to simultaneously detect different gasses with no interference to the outside humidity level. Moreover, the psychical adsorption of water vapor allows its evaporation at the end of experiments and therefore a single sensor can be used multiple times.

4.3 Summary

In this chapter, the development of the one-dimensional photonic crystal-based gas sensor has been described. The functional coating of the designed structure was fabricated by silica submicron particles of different nature - hydrophobic and hydrophilic ones. The detection is based on measuring the amount of condensed gases in the pores formed by silica particles on the sensitive area of the photonic crystal. Gases can condense according to three different mechanisms: in the air (homogeneous nucleation), on the surface (heterogeneous nucleation) and inside the pores [177]. Condensation in the pores occurs at the lowest partial gas pressures. The size of the silica particles defines the size of the pores which, in turn, is responsible for the amount of the condensed gases inside. It has been shown, that the total amount of condensed analyte between 180 nm particles and the substrate is 1.6 times higher than one between 300 nm particles and substrate.

5. Chapter 5. Postmodification of functional nanocoating

5.1 Introduction

Novel modalities of hybrid or functionalized optical fibers [2] typically come with increased optical losses since a significant surface roughness of functional layers gives rise to additional light scattering, restricting the performance of functionalization. For a deposition of functional materials (PE multilayers) onto planar substrates with a constant thickness increment, the surface roughness increases with the overall number of layers [14,123]. Thus, after substantial height variation, the rough coating induces extra light scattering due to surface topographies on the order of the wavelength of light that results in additional waveguiding losses that are unwanted in some applications based on optical properties of functional coatings [123]. To this extend, postmodification of multilayer films may also result in the appearance of novel structures or advantageous structural changes in the film. The surface morphology of polymer layers is usually controlled through postprocessing by "annealing" in aqueous solutions of different salt concentrations or pH levels. By controlling pH and ionic strength, it is possible to vary the thickness of adsorbed layers from ~1 to ~10 nm or, in some cases, completely prevent the multilayer deposition process [112,124]. Several research groups showed that treatment of polyelectrolyte multilayers in salt solutions caused swelling and led to smoother surfaces showing faster annealing for higher salt concentrations [123,125]. Treatment of multilayers with solutions at varying pH-induced morphological irreversible and reversible changes in both weak polyelectrolyte [106,124] and in H-bonded multilayers [126,127]. The intrinsic property of multilayers composed of weak polyelectrolyte complexes is that they can be destroyed at extreme pH conditions, as the pH-induced imbalance of charges overcompensates the attractive polymer-polymer ionic binding [128].

Another problem is that the conventional strategies rely on using materials with poor biocompatibility and high toxicity which are not optimal for sensitive in vivo applications.

5.2 Motivation

Here, a novel type of ultrasmooth, biocompatible and removable functional nanocoating for HC-MOFs formed by LbL assembly of bovine serum albumin (BSA) and tannic acid (TA) is introduced. The mechanism of the film deposition is based on the natural ability of tannins to precipitate proteins through hydrogen bonding and hydrophobic interactions [178].

Being the most abundant blood plasma protein, BSA is fully biocompatible [179]. In turn, the presence of galloyl groups [180] supplies TA with anti-inflammatory, antibacterial, antioxidant, and antifouling properties [180–182] that is extensively used for treating many diseases, tissue engineering [183], and wound healing [184]. Thus, functionalization with BSA/TA multilayers opens for HC-MOFs promising perspectives for using in *in vivo* biophotonic applications, including neurophotonics and biosensing.

The important benefit of the sequential LbL deposition technique is its versatility and cost-efficiency. The film formation occurs in water at ambient temperature and does not require any special equipment and expensive material components. Although cheap and simple, this entirely aqueous-based process creates multifunctional self-assembled films engineered at the nanoscale accuracy in a highly controllable, reproducible and reliable way.

5.3 Experimental section

For the creation of BSA/TA functional multilayers on the inner surface of HC-MOF, the modified version of the coating setup (Figure 3.4) has been used with connected suppliers of BSA and TA solutions. Solutions of BSA, TA and pure deionized water are streamed successively through the fiber by a peristaltic pump until the desired number of BSA/TA bilayers is formed. The pump creates a controllable and persistent liquid flow through the fiber, and the coating is formed by hydrophobic interactions and hydrogen bonding of protein-phenolic complexes at a neutral condition (pH 7) [117,178,185].

Morphology of the resulted coating is investigated via statistical analysis of 10 SEM micrographs for the fiber cross-sections taken at various positions along the fiber (Figure 5.1).

91
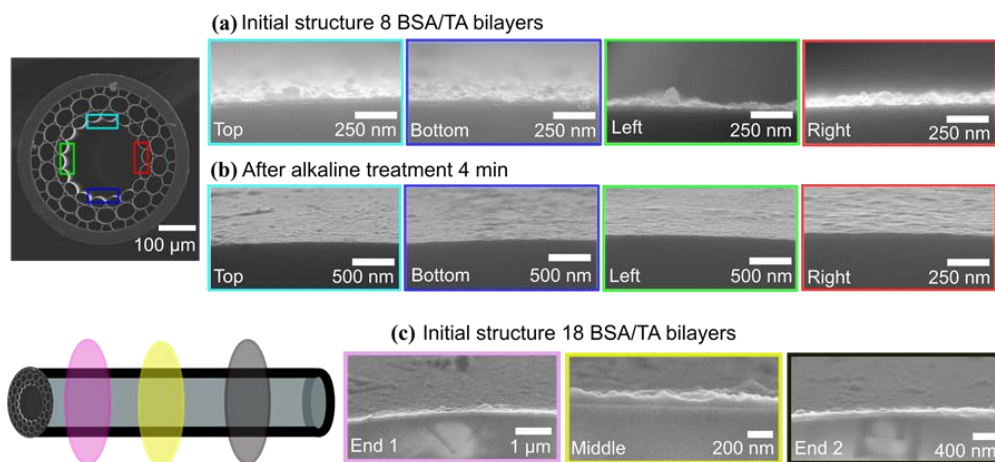
Figure 5-1: Evaluation of the coating roughness and thickness. (a) and (b) The structure of 8 BSA/TA bilayers before and after the alkaline treatment across the fiber cross-section. (c) The structure of 18 BSA/TA not-etched bilayers along the fiber. The frame color corresponds to the position where the SEM images were taken. The initial length of all the fibers was 6 cm, then three equidistantly located cuts were taken.

The coating thickness as a function of the number of bilayers is well described by a linear fit with the slope of 5.2 ± 0.3 nm per bilayer (Figure 5.2a,b). To gain insight into this result, one should account for an ellipsoidal structure of BSA molecules with dimensions 4 nm x 4 nm x 14 nm in an aqueous solution which alongside 1-nm-thick TA molecules is expected to yield a BSA/TA bilayer as thick as ~5 nm for a side-on alignment and ~15 nm for an end-on alignment [186]. At pH 7 both BSA and TA molecules keep negative charges so that the formation of BSA/TA complexes is driven by hydrogen bonding and hydrophobic interactions only [117]. Hence, a side-on scenario is more likely in the considered case, and it is clearly confirmed by the abovementioned evaluation of the bilayer thickness. Additionally, this evaluation is in good agreement with previously published data for the LbL coating of planar substrates, where the thickness per BSA/TA bilayer formed at pH 7 was ~7 nm [117].
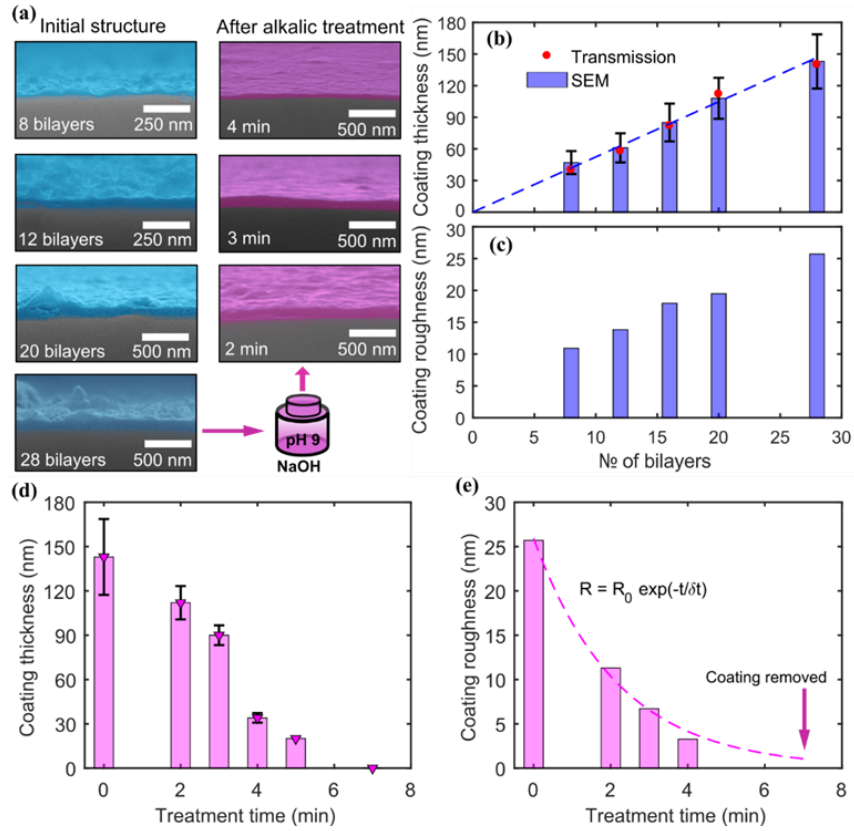
Figure 5-2: Characterization of the BSA/TA coating. (a) SEM micrographs of BSA/TA multilayers (indicated by the pseudocolor) before and after the etching. The coating (b) thickness and (c) roughness before etching as a function of the number of bilayers. The coating (d) thickness and (e) roughness versus the treatment time. The coating thickness is evaluated from SEM images (bars) and the shifts in the fiber transmission windows (red points). Error bars denote the coating roughness. The linear fit in (b) corresponds to the thickness of 5.2 nm per single bilayer. The coating roughness in (e) is fitted by the exponential function with the initial roughness $R_0 = 25.9$ nm and the decay time $\delta t = 2.2$ min.

Finally, SEM micrographs show that BSA/TA coating is formed in the internal surface of the central capillary only even though injection of the solutions is performed in all fiber capillaries. This effect is attributed to the enormous difference in the hydraulic resistance of the central and side capillaries. In the framework of the Hagen−Poiseuille model [187], the capillary hydraulic resistance is inversely proportional to its radius to the fourth power that means that a flow rate in the side channels is at least 1000 times slower

than in the core channel (see the detailed fiber geometry in Figure 3.1). The capillary hydraulic resistance can be expressed as:

$$R = \frac{8\mu L}{\pi r^4} \qquad (5.1)$$

where μ is dynamic viscosity, L is capillary length, r is the capillary radius.

For this reason, the coating is formed on the inner surface of the central capillary mostly. The coating formation in the side capillaries is possible but its thickness is less than the minimal structures of BSA/TA that SEM can resolve on the glass substrate (~10 nm) [14,99] which almost does not affect its optical properties.

Figures 5.2a and 5.2c show that the coating roughness increases with a growth in the number of bilayers, reaching 25 nm for a 140-nm substrate (28 bilayers). This is a general property of the LbL-deposited substrates, leading, specifically, to a significant rise in the fiber optical losses. To smooth the BSA/TA coating, we use its high sensitivity to the alkaline pH level of the ambient media, reducing protein binding accompanied by the coating dissociation [188]. Specifically, we post-process the coated samples by injection of the aqueous solution of NaOH at pH 9. Figures 5.2d and 5.2e show the evolution of the coating topography in the time when the initial structure is formed by 28 BSA/TA bilayers. Importantly, while the coating thickness decreases almost linearly, the roughness manifests an exponential decay as $R = R_0 \exp(-t/\delta t)$, where $R_0 = 25.9$ nm is the initial roughness and $\delta t = 2.2$ min is the roughness decay time. Hence, the smoothing is performed much faster than the dissolution which is also confirmed by the SEM images of multilayers with close thicknesses before and after the post-processing (Figure 5.2a). Finally, we reach the roughness of 3 nm at the substrate thickness of 30 nm that is 7 times smaller than the roughness of the initial substrate with the same thickness (Figure 5.3).
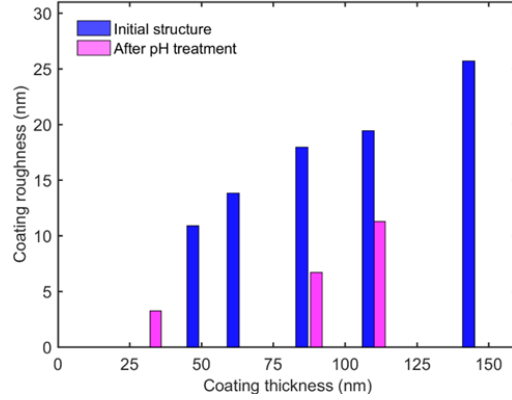
Figure 5-3: Coating roughness vs coating thickness.

To describe the optical properties of the BSA/TA multilayer, we employ the effective medium approximation within the Bruggeman formulation which introduces the effective permittivity of a two-phase mixture ε_{eff}, in the assumption that TA molecules in the form of spherical inclusions are randomly located in a homogeneous environment formed by BSA, as follows [189]

$$(1 - f_{TA}) \frac{\varepsilon_{BSA} - \varepsilon_{eff}}{\varepsilon_{BSA} + 2\varepsilon_{eff}} + f_{TA} \frac{\varepsilon_{TA} - \varepsilon_{eff}}{\varepsilon_{TA} + 2\varepsilon_{eff}} = 0, \tag{5.3}$$

where ε_{TA} and ε_{BSA} are permittivities of TA and BSA, and f_{TA} is the volume fraction of TA. Taking into account that $\varepsilon_{TA} = 3.71$ [190] and $\varepsilon_{BSA} = 2.25$ [14], we note that Eq. 5.3 still contains two unknown variables $- \varepsilon_{eff}$ and f_{TA} – which leads to multiple possible solutions.

To resolve this issue, the HC-MOF transmission spectrum was calculated by the transfer-matrix approach, following Noskov et al. [44]. Taking into consideration the fiber geometrical parameters alongside the glass refractive index and the coating thickness extracted from SEM micrographs, we evaluate the coating effective permittivity through fitting the theoretical fiber transmission spectrum to the measured one and find that $\varepsilon_{eff} = 2.56$. Hence, Eq. 5.3 yields $f_{TA} = 0.24$ and, consequently, $f_{BSA} = 1 - f_{TA} = 0.76$. Importantly, these values are in a good agreement with 4-nm and 1-nm thicknesses of BSA and TA molecules forming a 5.2-nm single bilayer in a side-on alignment.

Deposition of the BSA/TA coating shifts the fiber transmission windows towards longer wavelengths (Figure 5.4a) (Eq. 2.12) because of the growth in *d*, albeit with increased optical loss caused mainly by the layer roughness [14]. On the contrary, pH-treatment dissolves the BSA/TA coating associated with the blue shift of the transmission windows (Figures 5.4b and 5.4c). The transmission spectrum is returned to the case of an uncoated fiber in 7 min of the etching when the substrate is fully removed.
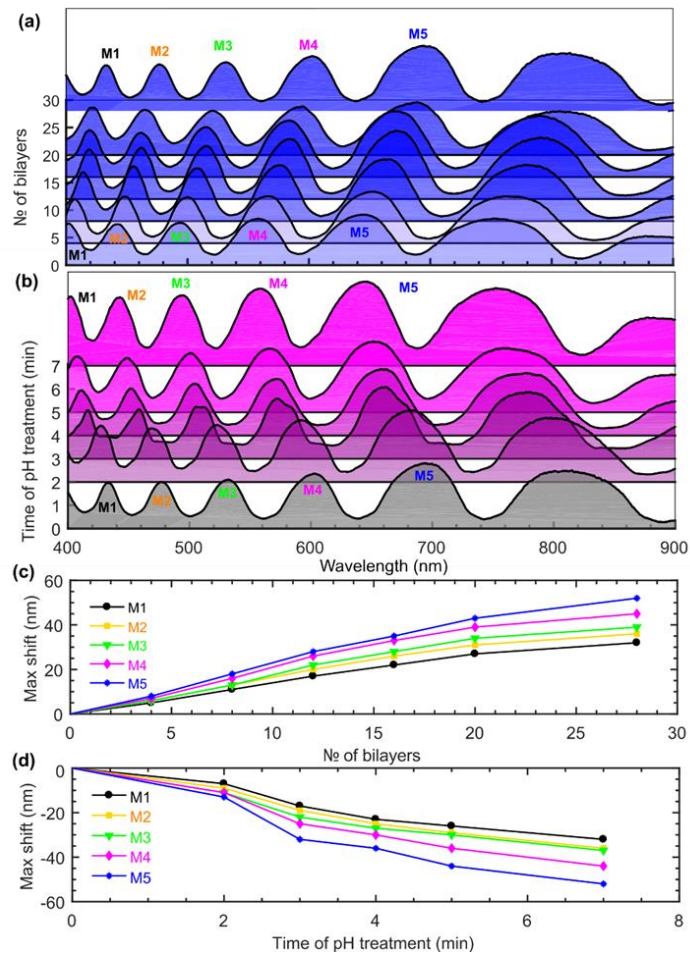
Figure 5-4: Evolution of the fiber transmission spectrum (a) with growth in the number of BSA/TA bilayers deposited and (b) in time upon the alkaline treatment for the HC-MOF coated with 28 BSA/TA bilayers. Relative shifts of the transmission maxima vs (c) the number of BSA/TA bilayers deposited and (d) the treatment time for the initial coating with 28 BSA/TA bilayers. The measured values are denoted by points joined with lines as guides for the eye.

Additionally, the alkaline etching gives rise to an exponential temporal decrease in the fiber loss with the decay time $\delta t = 4.1$ min (Figure 5.5a). It is important to note that the decreased fiber loss can be obtained for any predefined coating thickness. As an example, Figure 5.5b compares the fiber loss for not etched and etched samples, supplementing data on the coating morphology shown in Figure 5.2a. 2 min etching of HC-MOF with 28 bilayers decreases the fiber loss by ~40% from 1.2 dB cm^{-1} to 0.7 dB cm^{-1} that is 30% less than the loss for the not-etched fiber with the equal coating thickness ~115 nm. Furthermore, 4-min etching results in the loss drop by three times up to 0.41 dB cm^{-1} with the coating thickness ~ 30 nm and roughness ~ 3 nm (see also Figure 2a).
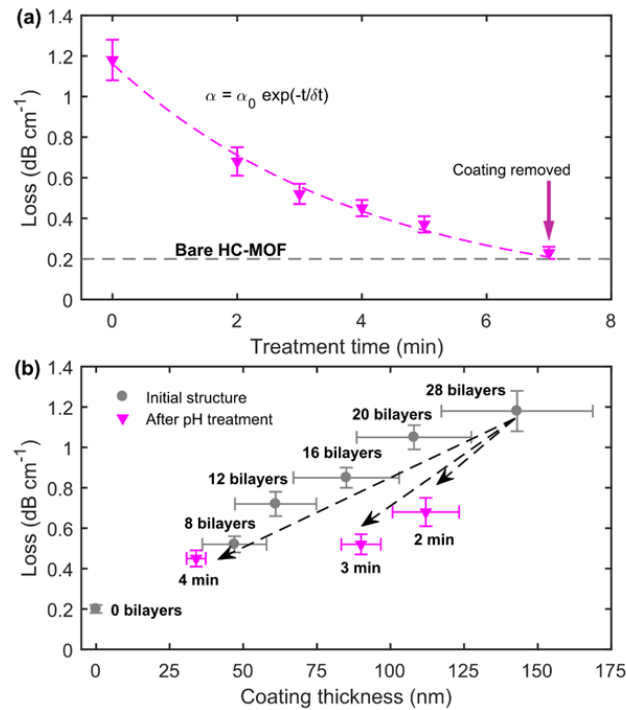
Figure 5-5: Optical fiber loss as a function of (a) treatment time and (b) coating thickness. Fiber losses are calculated by averaging across minimal losses for all transmission windows, and the error bars correspond to the standard deviation. The substrate with 28 initial BSA/TA bilayers was etched. The fiber optical loss in (a) is fitted by the exponential function with the initial fiber loss $\alpha_0 = 1.16$ dB cm^{-1} and the decay time $\delta t = 4.1$ min. The loss measurements were performed by the cut-back technique.

5.4 Summary

In summary, a novel type of functional nanocoating for HC-MOFs formed by LbL assembly of BSA and TA has been demonstrated. Tuning the HC-MOF transmission spectrum with the BSA/TA multilayers is a highly controllable and fully reversible operation. The resulted BSA/TA multilayers are characterized by the thickness of 5.2 nm per single bilayer with a surface roughness reaching 26 nm for the 140 nm thick layer. The average thickness per single bilayer has a good correlation with previously published data for planar layers [117]. To smooth the BSA/TA substrate, alkaline etching has been applied. The temporal kinetics of the coating dissolution shows that the alkali drops the surface roughness to 3 nm within 4 min of the treatment, resulting in decreasing the fiber optical losses by a factor of 3. The coating is fully removed after 7 min of the treatment.

The simplicity, speed, and efficiency make the presented technique stand out from other similar techniques of producing LbL-assembled multilayers from polymers whose smoothing calls for the time ranging from several hours to several days [123,125,191].

Additionally, full biocompatibility alongside anti-inflammatory and antibacterial properties makes it possible to implant HC-MOFs functionalized with BSA/TA multilayers into living tissue which could serve as a promising neurophotonic interface providing enhanced light-neuron interactions for efficient optical manipulations of neuronal structures and monitoring brain functions [192]. Beyond that, TA-functionalized planar films have recently been found to efficiently capture circulating tumor cells (CTC) [180]. This suggests that, being incorporated into a medical endoscope, the considered system would potentially enable real-time monitoring of CTC in bodily liquids.

6. Chapter 6. In-fiber multispectral optical sensing

6.1 Introduction

The interaction mechanisms of light with tissues, cells and liquids are the basis for the most extensive development of novel optical methods for use in biology and medicine. These methods allow one to obtain information about the structure, state, and transformation of various components of biological systems [193]. The increasing medical need for robust techniques suitable for real-time diagnostics at the place of patient care is at the cutting edge of modern biosensing. Among the variety of available sensing devices, optical label-free sensors demonstrate high sensitivity to ambient refractive index variations, attracting considerable attention from the chemical, biomedical and food processing industries. The main efforts in the development of such sensors are focused on increasing refractive index sensitivity (RIS) through the employment of cavity resonances (including surface plasmon resonances, Mie resonances, whispering gallery modes, etc.) and propagating eigenmodes in dielectric and plasmonic nanostructures. Conceptually, another approach is realized by HC-MOFs, which allow sensing of liquid analytes by monitoring the changes in the optical transmission; HC-MOFs have a great advantage of enabling high volume for measuring light-analyte interactions, which improves the RIS in comparison to that with cavity-based counterparts. An overview of point-of-care devices and optical label-free sensors based on optical fibers can be found in references [18,194–197].

6.2 Motivation

The refractive index of any biological liquid is a basic material parameter that characterizes how light interacts with liquids. Refractive index is a nonlinear parameter and strongly depends on wavelength, in the visible range, a decrease of the RI comes with an increase of the wavelength. This dependency is called optical dispersion [193]. In spite of the existence of comprehensive RI measuring systems and techniques, for many biological liquids and blood components, the data for RI in a wide spectral range and concentrations are not yet available or available only for a single wavelength [23]. In many optical studies, a rough estimate of RI of the biological liquids under study, based on the

99

fact that the main constituent of any solution is water or more precisely a mixture of water and other materials, is often used. Therefore, these data are not used in practice especially for optical diagnostics by using different lasers and at tissue heating in the course of various laser therapies.

However, monitoring of the RI in the broad spectral range could be a simple and cost-effective fingerprint of liquid biosamples to enable real-time analysis of changes in their composition. These features are also important to provide rapid diagnostics of pathological changes in cells, tissues and other biological samples. In particular, variations in the optical dispersion of blood serum may indicate some diseases since it is directly related to changes in blood components, specifically the concentration of albumin and the appearance of its conjugated forms. Recently, it was shown [198] that variations in the blood serum RI could be used as an additional criterion in the analysis of antitumor therapy and RI monitoring for glycated hemoglobin and albumin enables diagnostics of type 2 diabetes and pre-diabetic status. Serum albumin is the most abundant blood plasma protein and plays a pivotal role in maintaining oncotic pressure as well as in transporting poorly soluble molecules, including lipid-soluble hormones, bile salts, unconjugated bilirubin and many others. The normal concentration of albumin in the serum of human adults is 35–54 g L^{-1}, while its deviations indicate various abnormal conditions and diseases. Since albumin is optically transparent, direct determination of the analyte concentration by measuring the optical absorption is not applicable. The typical detection of the albumin concentration is based on the changes in dye absorbance (such as bromocresol green or bromocresol purple) upon binding to albumin. Alternatively, it was proposed to detect low concentrations of albumin with the optical spring effect in an optomechanical oscillator and plasmon polaritons in a hyperbolic metamaterial. Such techniques, however, are time-consuming and do not allow instantaneous monitoring of albumin in biological fluids in real-time.

Here, the concept of in-fiber multispectral optical sensing (IMOS) for liquid biological samples in both static and real-time modes was introduced. The sensing principle relies on detecting spectral shifts of maxima and minima in the transmission spectrum of

100

HC-MOF when a liquid bioanalyte is streamed through it via specially designed liquid chambers. These resonant features are associated with Fabry–Perot resonances in the core capillary wall, and their spectral positions can be affected to the bioanalyte refractive index. IMOS offers a unique opportunity to measure the refractive index at 42 wavelengths, with a sensitivity up to ~3000 nm per refractive index unit (RIU) and a figure of merit reaching 99 RIU^{-1} in the visible and near-infrared spectral ranges. We apply this technique to determine the concentration and refractive index dispersion for bovine serum albumin (BSA) and show that the accuracy meets clinical needs.

6.3 Results and discussion

6.3.1 Empirical extraction of RI for liquid filling

The validity of the proposed approach of IMOS was demonstrated by measurements of the RI for BSA at different concentrations dissolved in a water buffer. A single HC-MOF allows simultaneous measurement of an analyte's RI synchronously at seven wavelengths (4 minima and 3 peak centroids) in the visible and near-infrared spectral domains. However, such a number of wavelengths is still insufficient for accurate retrieval of RI optical dispersion, especially in cases when data are contradictory to each other or not available. The number of discrete wavelengths available for measuring RI can be increased by using several HC-MOFs with slightly shifted transmission windows with the help of six functionalized HC-MOFs with 0, 14, 22, 31, 40 and 54 PAH/PSS bilayers (see Section 3.4.4).

The measurements start with calibration of the system by recording the transmission of the water-filled fiber and associate the spectral positions of the minima and the peak centroids with the water RIs by using Eqs. (2.12) and (2.13). The stability of the experimental technique was confirmed by the excellent agreement of the measurements with the well-known optical dispersion of deionized water adopted from Ref. [199].

Figure 6.1 shows the transmission spectra of the liquid-filled HC-MOF with different concentrations of BSA solution (0 and 20 g L^{-1}). Optical dispersion of water is taken from Ref. [199] and follows (Eq. 6.1):

$$n_{water} = \sqrt{1 + \frac{0.5670093832 * \lambda^2}{\lambda^2 - 0.004610301794} + \frac{0.1719708856 * \lambda^2}{\lambda^2 - 0.01825180155} + \frac{0.01992501582 * \lambda^2}{\lambda^2 - 0.02224158904} + \frac{0.1193965424 * \lambda^2}{\lambda^2 - 13.27505178}} \qquad (6.1)$$
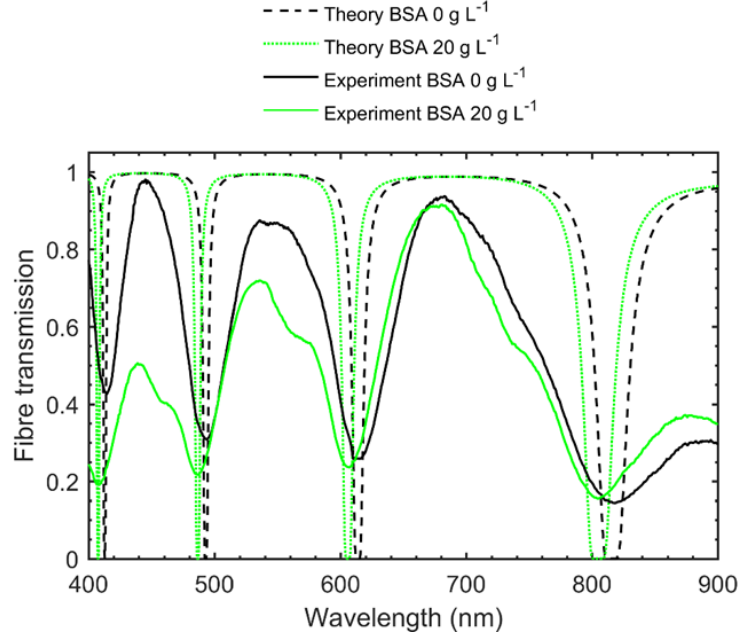
Figure 6-1: Theoretical and experimental transmission spectra of HC-MOF filled with water and the BSA-water solution at the concentration of 20 g L^{-1} [14].

RI of the BSA-water solution can be extracted empirically by adding a correction (Δn) to n_{water} to obtain coincidence in the positions of transmission minima and maxima (or maxima centroids) for theoretical (dotted green line) and experimental (solid green line) transmission spectra. The positions of the centroids have been found to be more sensitive to the variations in an analyte RI than the maxima and were used for further measurements.

6.3.2 Transmission of HC-MOFs filled with a water-BSA solution

In the static regime, HC-MOFs were integrated into a smart cuvette [44] and filled by the solutions in the test through capillary action. Once the fiber was filled completely and no air bubbles appeared, the transmission spectrum was recorded successively for each fiber sample. In addition to fiber holding, the smart cuvette can also control meniscus formation that is important for light coupling when the fiber is filled with liquid. Each of the BSA-filled samples has four well-defined minima of the transmission spectra in the

visible and near-IR spectral ranges (400 nm – 900 nm) while the peaks are distorted (Figure 6.2) and for that reason, we use the centroids of the transmission windows in the analysis.
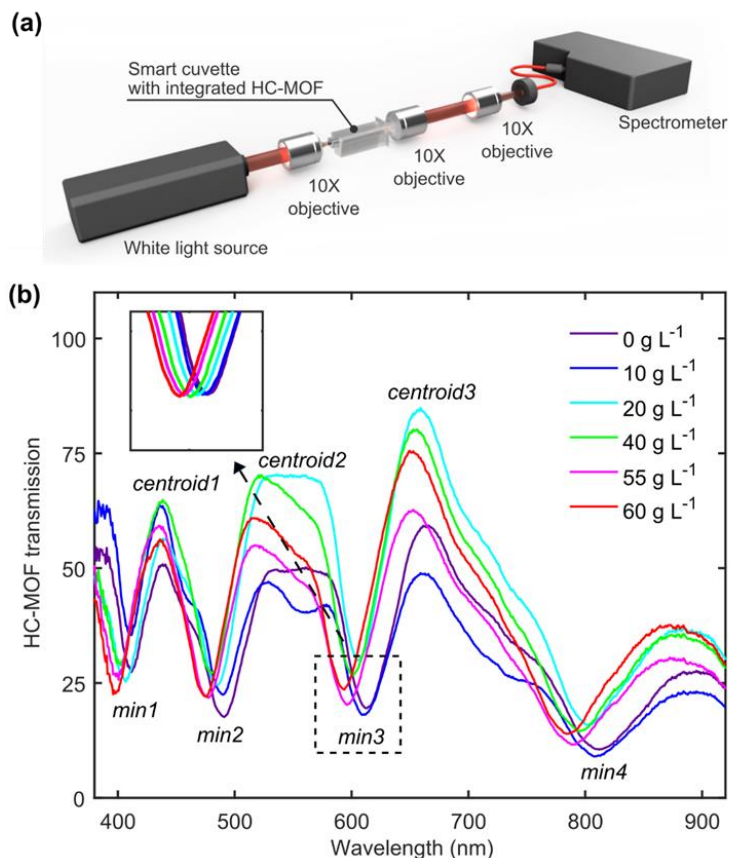
Figure 6-2: Static measurements of the transmission for HC-MOFs filled with a water-BSA solution. (a) The schematic of the optical setup. (b) The transmission of liquid-filled HC-MOF for different concentrations of BSA [14].

6.3.3 IMOS in static mode

Figure 6.3a shows the evolution of transmission spectra caused by an increase in BSA concentration in a water buffer. Using these data, we obtained RIs by the same algorithm (Figure 6.4) as that for pure water and plot them along with the Sellmeier fits, as shown in Figure 6.3b. To verify our results independently, we also measure the RIs of these samples by a multiwavelength Abbe refractometer (DR-M2/1550, Atago, Japan) (denoted by the stars in Figure 6.3b) and find very good agreement with the IMOS results.
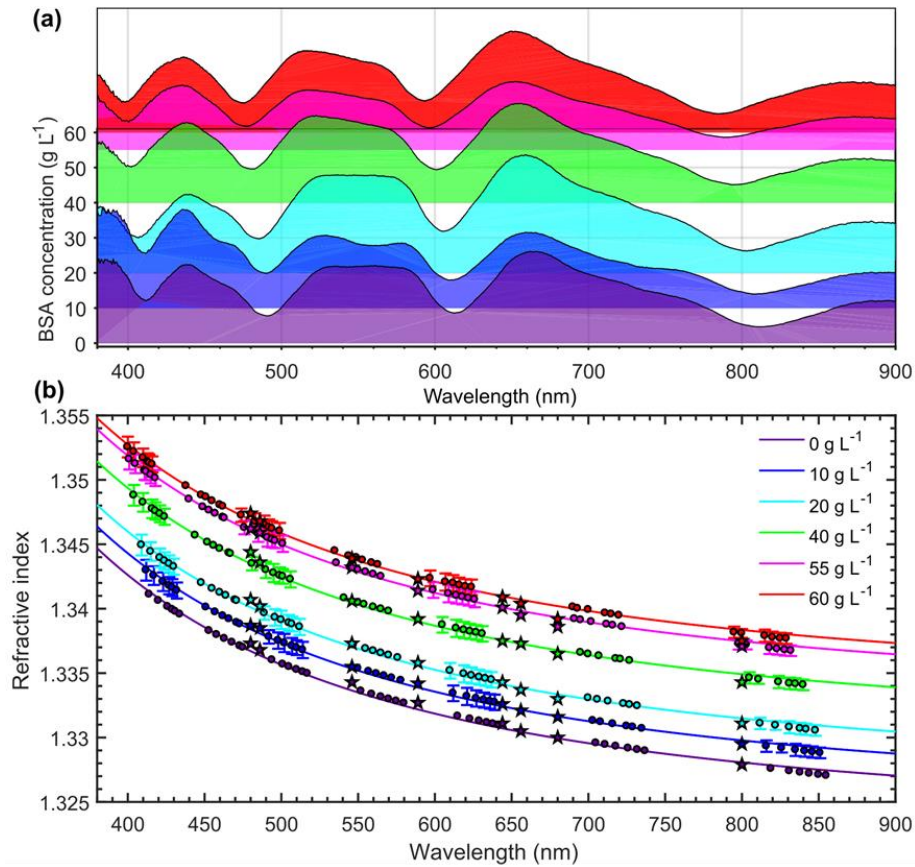
Figure 6-3: Performance of IMOS for BSA dissolved in deionized water in static mode. (a) Transmission spectrum evolution with increasing BSA concentration for the non-modified HC-MOF. (b) Optical dispersion of BSA in a water buffer with different concentrations. The colored points indicate the RI values extracted from the shifts in the minima and the peak centroids of the fiber transmission spectra, and the solid lines mark their Sellmeier fits. For pure water, the Sellmeier fit describes the water dispersion adopted from Ref. [199]. *The error bars are obtained from the spectrometer's optical resolution. The stars mark RIs measured by the Abbe refractometer, provided for comparison* [14].

104
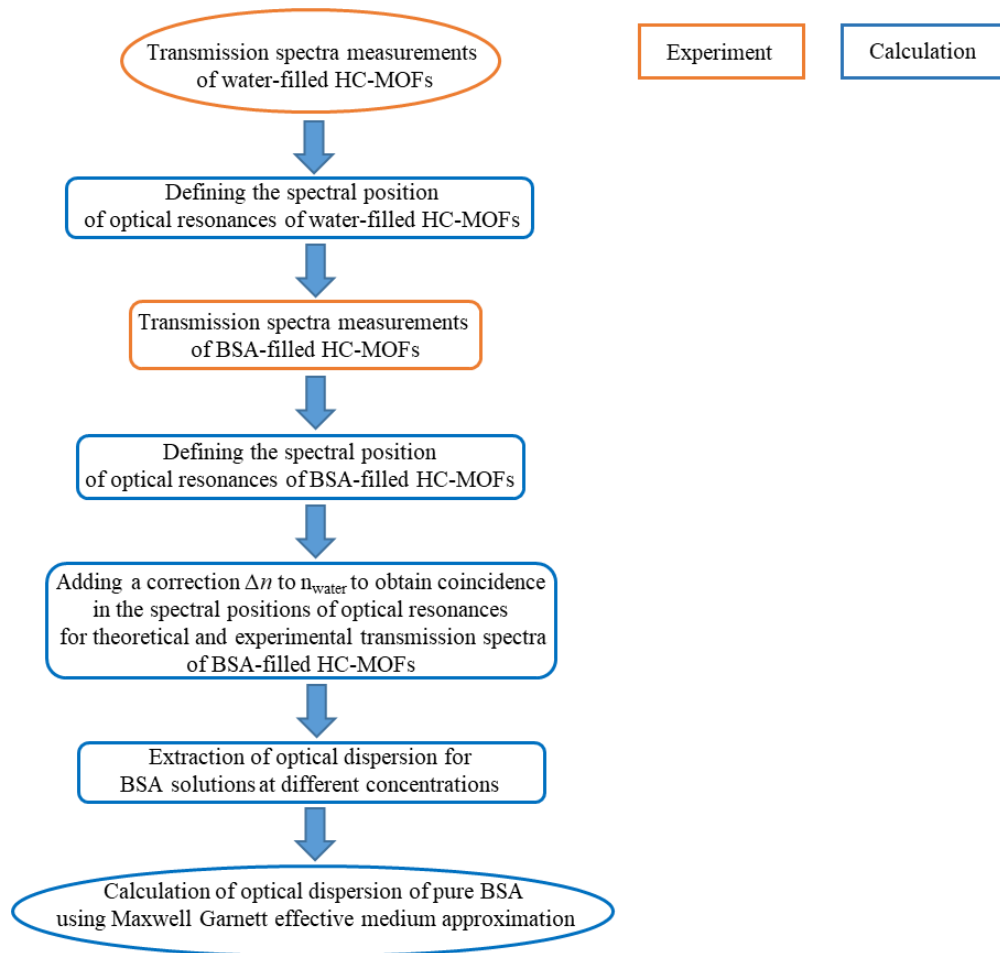
Figure 6-4: Algorithm for the extraction of optical dispersion of BSA solution at different concentrations.

In practical applications, it is important not only to determine the RIs of a biological liquid but also to quantify the concentration of target biomolecules. To this end, we calibrate our system by associating the RIs of the samples at different wavelengths with the concentration of BSA (Figure 6.5). Since the concentration of BSA is quite low, these dependencies are linear.
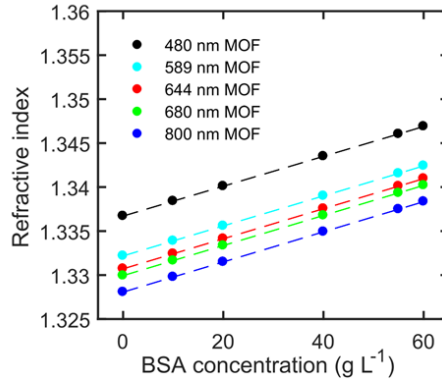
Figure 6-5: Calibration relating the concentration of BSA and RIs of the BSA-water solution at different wavelengths. The RIs of BSA are extracted from the Sellmeier fits of the experimental points [14].

6.3.4 Impact of the liquid sample internal losses on the HC-MOF transmission

It should be noted that solutions with strongly absorbing analytes can be investigated only with preliminary preparation of the probe via dilution. The higher optical losses introduced by the low-transparency filling media result in minima and maxima distortion. Increasing optical losses of the sample will lead to eroding the maxima and minima of the fiber transmission spectra, deteriorating the IMOS performance. Figure 6.6 provides quantitative evaluations, showing the transmission spectra of a 6-cm-long fiber for various imaginary parts of the sample refractive index (n''). Importantly, while the maxima are well distinguished up to $n'' = 0.01$, the minima get markedly eroded for longer wavelengths at $n'' \geq 0.001$. Thus, IMOS is best performed for sufficiently transparent liquids.
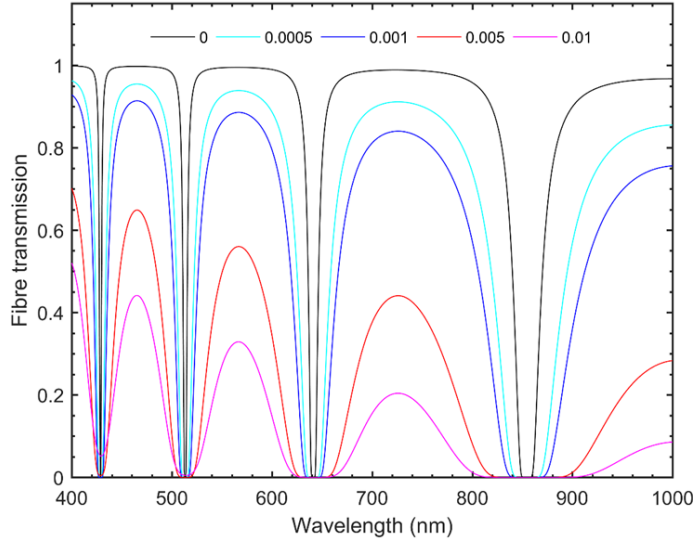
Figure 6-6: Fiber transmission spectra for a various imaginary part of the sample refractive index: 0 (black), 0.0005 (cyan), 0.001 (blue), 0.005 (red) and 0.01 (magenta). The real part of RI equals to 1.33 [14].

6.3.5 Refractive index sensitivity and figure of merit

The key characteristics of label-free optical sensors are the RIS, defined as the ratio of the change in sensor output (the shift of the resonant wavelength) to the analyte RI variation, and the figure of merit (FOM), which normalizes the RIS to the width of the tracked resonance characterized by the full width at half maximum (FWHM). Figure 6.7 shows the transmission minima as a function of analyte RI along with RIS and FOM. The slope of the linear fit corresponds to RIS as (Eq. 6.2):

$$RIS = \frac{\Delta \lambda}{\Delta n} \tag{6.2}$$

FOM is RIS normalized by FWHM of a resonance (Eq. 6.3):

$$FOM = \frac{RIS}{FWHM} \tag{6.3}$$

Using the fiber transmission spectra (Figure 6.3a) and the determined RIs of the BSA-water solutions (Figure 6.3b), the transmission spectra minima versus the analyte RI were plotted. The slopes of the linear fits show the RIS of the MOF-based sensor, which varies from 1100 nm RIU^{-1} for the blue light to 3000 nm RIU^{-1} for infra-red light. The corresponding FOM varies from 60 to 99 RIU^{-1}. These values along with the working spectral range are typical for surface plasmon and 2D material sensors. However, the

107

proposed approach provides a great benefit of multispectral analysis in a broad spectral range.
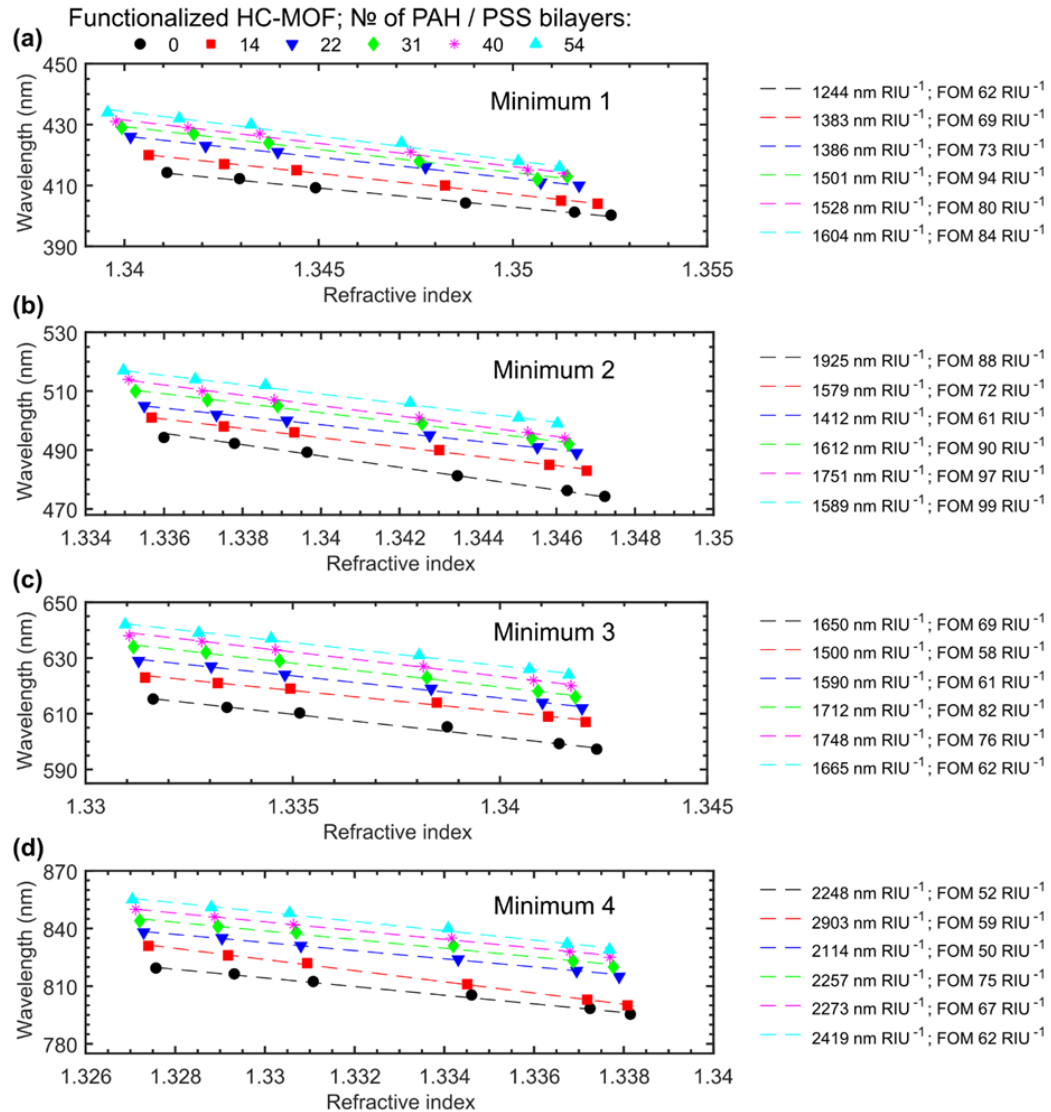
Figure 6-7: (a,b,c,d) The minima positions extracted from the transmission spectra of HC-MOFs as a function of the filling refractive index obtained by variations in the concentration of BSA. The error bars are smaller than the data points [14].

The comparison of the desighned sensor performance and the existing fiber-based sensors can be found in Refs. [200,201].

6.3.6 Optical dispersion of refractive index for bovine serum albumin

It is important to note that the optical dispersion for a solution containing an investigated substance dissolved in a water buffer can be used to determine the optical dispersion of the pure substance. Such a possibility is of special interest in cases when the substance of interest is difficult to synthesize in the form of thin films, which are normally suitable for analysis with standard techniques such as ellipsometry or refractometry. This is the case for BSA, whose RI has been reported for only a few wavelengths: 436 nm [202–205], 546 nm [202,203,205], 578 nm [205–207], 589 nm [202,207], and 840 nm [208]. Accounting for BSA molecules as uniaxial ellipsoids with overall dimensions of 4 nm x 4 nm x 14 nm [209,210], the extraction can be performed by using the effective medium approximation, which describes the effective permittivity ε_{eff} of the solution by the Maxwell Garnett equation as follows (Eq. 6.4) [189,211]:

$$\varepsilon_{eff} = \varepsilon_e + \varepsilon_e \frac{\frac{f_{BSA}}{3}\sum_{j=x,y,z}\frac{\varepsilon_i-\varepsilon_e}{\varepsilon_e+N_j(\varepsilon_i-\varepsilon_e)}}{1-\frac{f_{BSA}}{3}\sum_{j=x,y,z}\frac{N_j(\varepsilon_i-\varepsilon_e)}{\varepsilon_e+N_j(\varepsilon_i-\varepsilon_e)}} \tag{6.4}$$

where ε_e and ε_i are the permittivities of the water buffer and the inclusions (BSA molecules), respectively, f_{BSA} is the volume fraction of the BSA molecules, and N_x, N_y and N_z are the depolarization factors over the x, y and z axes, respectively. The molecular weight of 66.5 kDa [209,210] and dimensions of BSA molecules allow us to translate the mass concentration of BSA into the volume filling factor f_{BSA}. By using the known optical dispersion of water and the measured RIs of the BSA-water mixtures, we determine the optical dispersion of BSA (Figure 6.8). To verify the repeatability of this process, we perform this procedure for 3 concentrations of BSA, 20 g L^{-1} (f_{BSA} = 0.0213), 40 g L^{-1} (f_{BSA} = 0.0425), and 60 g L^{-1} (f_{BSA} = 0.0638), resulting in almost identical dispersion curves. The discrepancy falls within the range of the measurement accuracy.
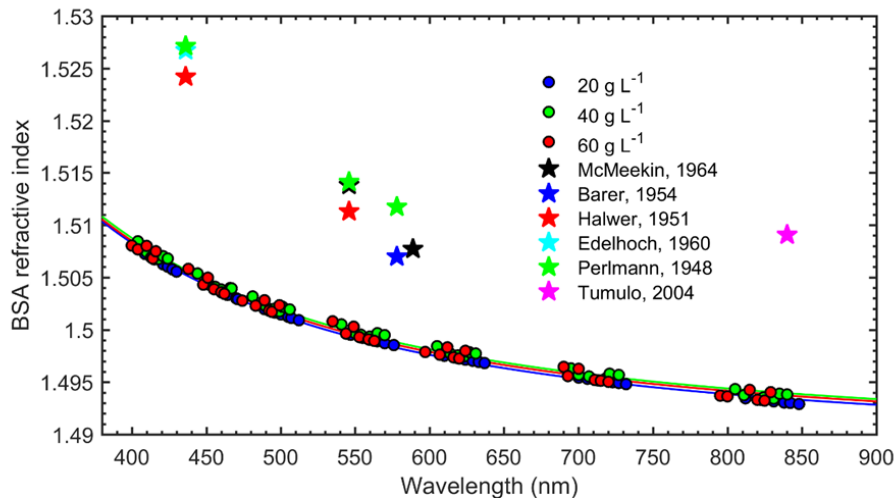
Figure 6-8: The refractive index of BSA determined via the Maxwell Garnett approximation. Points correspond to the measurements of RI for BSA-water, and solid lines mark the Sellmeier fits. The extraction was performed for 3 concentrations of BSA to show the repeatability of the result [14]. *The error bars are smaller than the marker size. The stars mark BSA RI values adopted from Refs.* [202–206,208].

It is instructive to compare the RI dispersion of BSA obtained by IMOS with the data available in the literature [202–206,208] (Figure 6.8). All previous measurements of BSA RI have been performed by refractometry of water-BSA solutions, and they show deviations from each other and from our results. However, the difference between the results is in the range of less than 0.025 RIU. These dissimilarities can be attributed to the distinct purity of BSA used in different measurements. In the current experiments, BSA produced by Sigma-Aldrich with a purity above 96% was utilized, while the purity of BSA measured in previous works was not reported. However, purity is a critical parameter that can significantly affect the measurement results. To this end, we compare the results for BSA produced by Sigma-Aldrich (>96% purity) [212] (St. Louis, MO, USA) and Agat-Med (50% purity) [213] (Moscow, Russia) and find a discrepancy of ~0.05 RIU (Figure 6.9). The purity of the samples has been verified by sodium dodecyl sulfate-polyacrylamide gel electrophoresis analysis.
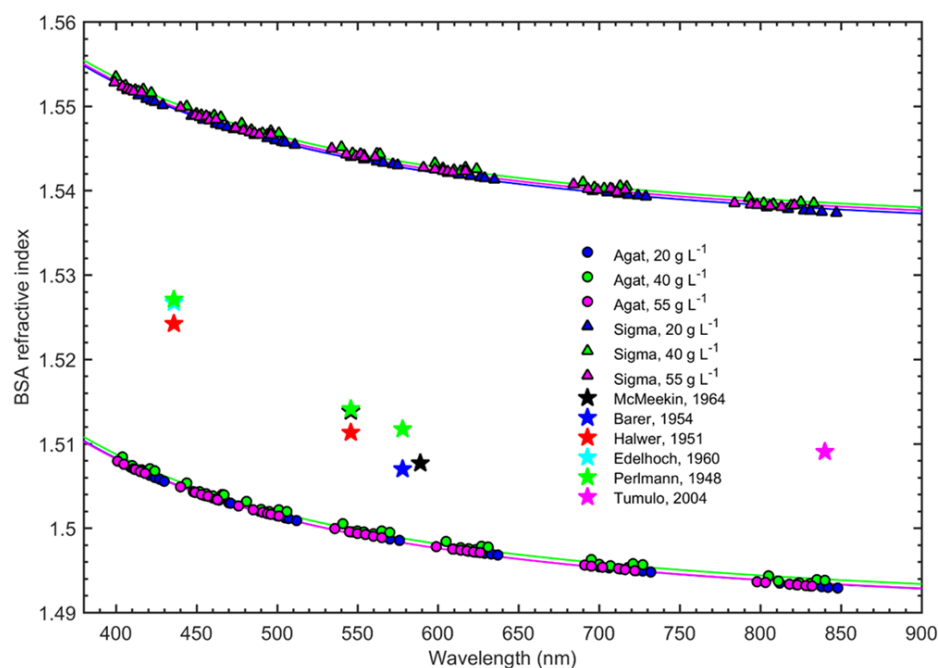
Figure 6-9: The refractive index of BSA extracted via the Maxwell Garnett approximation. Circles correspond to the measurements of RI for the BSA supplied by Sigma-Aldrich (>96% purity) and triangles to the BSA supplied by Agat-Med (50% purity), and solid lines mark the Sellmeier fits. The extraction is performed for 3 concentrations of BSA to show repeatability of the result [14]. *The pentagrams mark BSA RI extracted from Refs* [202–205,208,214].

6.3.7 IMOS in real-time

In the dynamic regime, HC-MOFs were sealed in specially designed liquid cells (LCs). Cells were prepared using the commercially available 3D printer Prusa i3 steel. Its printing tolerance of ~0.1 mm totally meets the accuracy requirements for the reproducible production of high-quality liquid cells. In total, two liquid cells and HC-MOF sealed in them form a simple and robust structure. A detailed schematic of the designed LCs is illustrated in Figure 6.10.
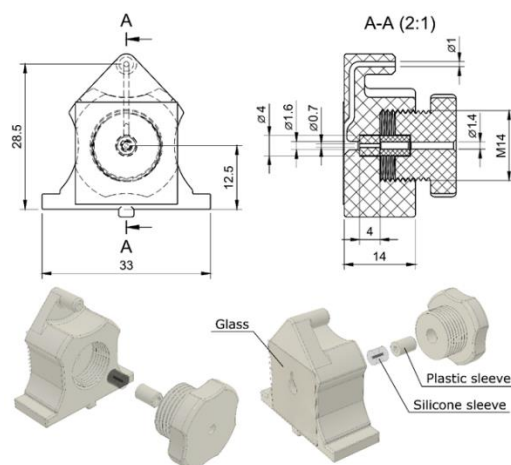
Figure 6-10: Schematic of the liquid cells. Dimensions are denoted in mm [14].

Liquid samples were streamed through the HC-MOFs by the peristaltic pump connected to the inlet of the LC. Real-time tracking of the transmission spectra minima for the fundamental fiber mode only was achieved by means of LabVIEW software (Ivan Gnusov wrote the code) [14] (Figure 6.11).
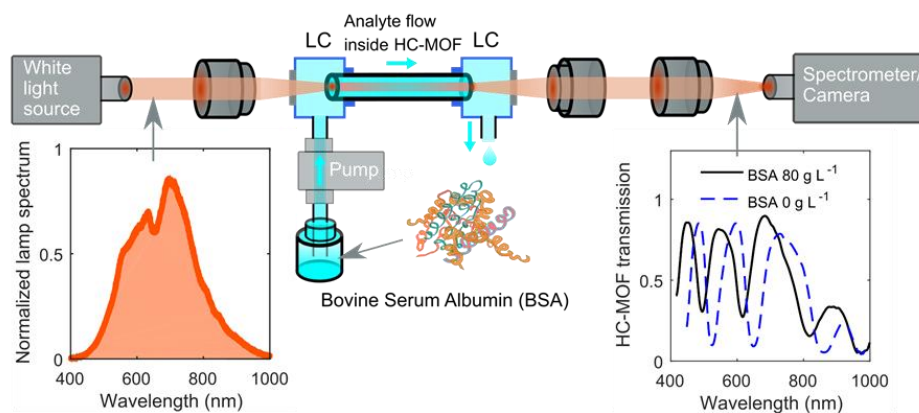
Figure 6-11: Illustration of the dynamic multispectral sensing concept for liquid samples. Scheme of the setup for transmission characterization of HC-MOFs. Fiber facets are fastened in liquid cells (LCs), which are optically accessible via thin glass windows, allowing simultaneous pumping of fluids through fiber capillaries and measurement of the transmission spectrum. The red rays illustrate the light path from a broadband halogen lamp through the HC-MOF to the spectrometer and the CCD (charge-coupled device) camera to record the output mode profile. The insets depict the input and output spectra for different concentrations of BSA dissolved in PBS [14].

The geometrical structure and the relatively large sizes of the hollow-core and the surrounding cladding capillaries allow the controllable and persistent stream of solutions inside the hollow channels at various flow rates (from 50 to 1000 µL min^{-1}). Figure 6.12 displays the results. Although the PBS buffer for BSA dissolution prevents the intensive formation of air bubbles while the analyte flows through the fiber, bubbles still appear at the moments of solution switching, leading to instantaneous disturbance of the minima positions during the transitional time intervals (colored curves in Figure 6.12).
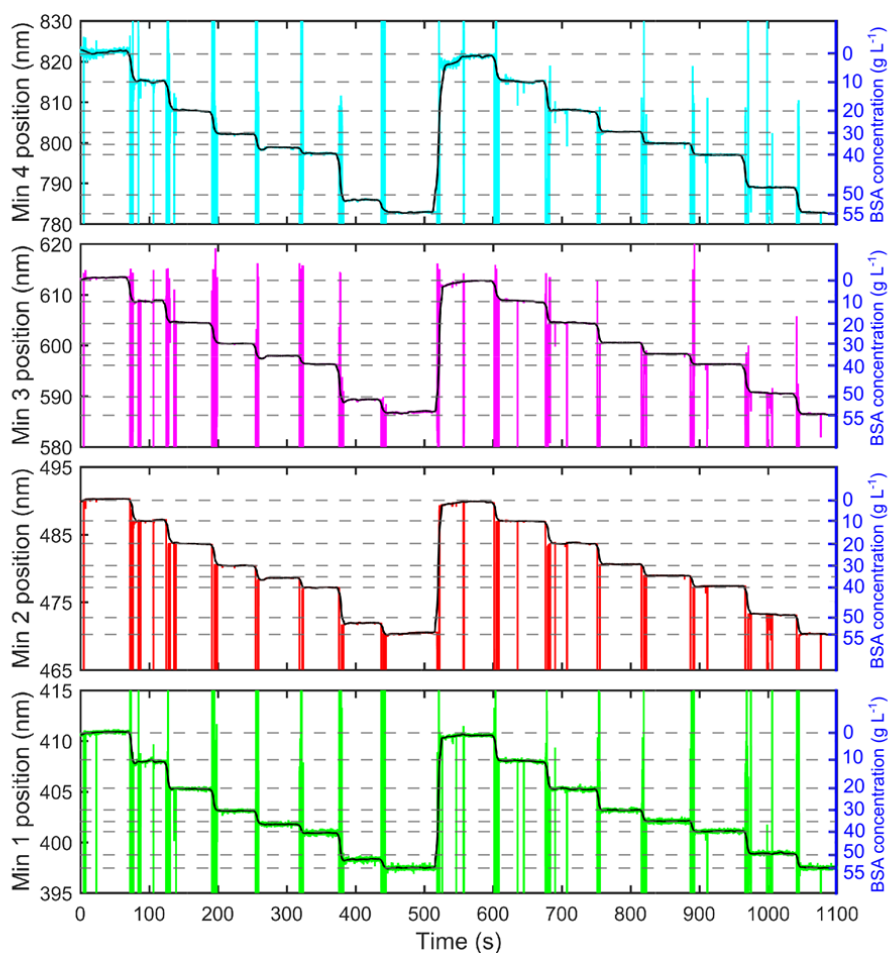
Figure 6-12: IMOS in real-time for BSA dissolved in PBS buffer. The colored lines denote instantaneous positions of the transmission minima when the peristaltic pump is switched between 5 solutions with different concentrations of BSA. The black lines exhibit the data smoothed with MATLAB. The flow rate created by the peristaltic pump is fixed at 1 mL min^{-1} [14].

It should be noted that real-time monitoring of RI optical dispersion simultaneously at 42 (or even several hundred) wavelengths can be achieved by using several post-processed HC-MOFs with necessary modifications of LCs and adaptation of the optical setup to parallel measurements (Figures 6.13).
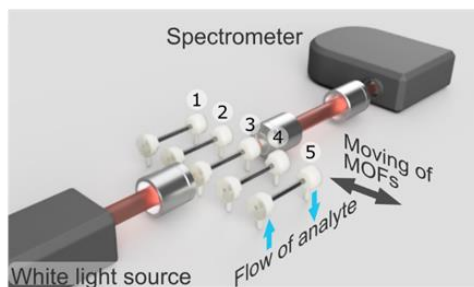
Figure 6-13: Illustration of the automatic fiber switching in the system optical path by a piezo stage. Independent optical paths can be created to perform measurements simultaneously with all fibers [14].

6.4 Summary

In summary, the technique of IMOS based on the analysis of spectral shifts in the minima and maxima of the HC-MOF transmission filled with a bioanalyte has been proposed and experimentally demonstrated. In contrast to the convential optical biosensors that work at only a single wavelength, the presented approach allows simultaneous measurement of the RI at many wavelengths in the visible and near-infrared spectral domains with RIS values up to ~3000 nm RIU^{-1} and FOMs reaching 99 RIU^{-1}. Specifically, we have demonstrated the use of IMOS to measure the optical dispersion and concentration of BSA dissolved in water and PBS buffers in both static and dynamic regimes, with a resolution of ~1 g L^{-1} (Figure 6.5) when determining the BSA concentration, which matches the accuracy of the standard tests on albumin. Furthermore, for the first time, to our knowledge, we have extracted the RI of pure BSA at 42 spectral points in the wavelength range 400 – 850 nm based on a specially developed algorithm (Figure 6.4). Potentially, the number of wavelengths available for the measurement of RI can be increased further to several hundred by producing the necessary number of HC-MOFs with slightly shifted transmission windows [14].

114

It is instructive to compare IMOS with refractometers and ellipsometry, which perform similar RI identification. The operational principle of conventional Abbe refractometers relies on using a set of filters, one filter per single acquisition wavelength so that the RI measurements can be performed in a static regime only, and the number of wavelengths available for the measurements is restricted by the number of filters. Modern digital refractometers are more convenient, performing all operations in an automatic mode; however, they do not support real-time measurements. In-line refractometers, which are widely used in various manufacturing areas, target only a single wavelength (usually 589 nm) and therefore cannot be used for the laboratory analysis of liquids over a wide spectral range. Overall, the modern market of available refractometers is diverse. However, these devices are expensive, restricted in the number of wavelengths available for measurement (typically less than 10) and cannot perform real-time measurements at several wavelengths in parallel [215].

Thus, the main benefits of IMOS in comparison to refractometers and ellipsometers are simplicity and cost efficiency, and the setup is quite compact and simple for reproduction. In addition, IMOS makes it possible to perform RI measurements over a wide spectral range, providing great capacity for practical use. Specifically, the integration of LCs with surgery endoscopes will pave the way towards the intraoperative analysis of bodily fluids, enabling surgeons to act in a timely manner under variable conditions. Multispectral analysis of saliva, urine, and ascitic fluid will facilitate diagnostics of various diseases. In addition, IMOS enables accurate determination of the RI optical dispersion for various proteins and their complexes, which is important for reliable simulations of biological processes [216].

7. Chapter 7. Noncontact characterization of microstructured optical fibers coating in real-time

7.1 Motivation

Various experimental techniques such as scanning electron, surface force and atomic force microscopy (SEM, SFM and AFM), X-ray and neutron reflectivity, UV-VIS and IR spectroscopy, single particle light scattering, ellipsometry, surface plasmon resonance (SPR), interferometry and quartz crystal microbalance (QCM) have been used to characterize self-assembled polyelectrolyte (PE) films [119,157,217–225]. Although these studies have yielded detailed information on the film thickness and properties, they are based on sophisticated measuring techniques using bulk and expensive laboratory tools that prevent fast and easy analysis of deposited layers. Moreover, most techniques operate only in a steady mode and are carried out on dried films, not allowing *in situ* monitoring of multilayer growth. The real-time ellipsometry, SPR, AFM and QCM measurements, in turn, require complicated calibration protocols and precise adjustment of measuring units, and they are very sensitive to the surface imperfections and any height deviations [218,224]. In addition, these methods are only suitable to characterize PE multilayers deposited on planar silicon and quartz substrate or a metalized surface. Interferometric reflectance spectroscopy is also applicable for very limited structures generating a fringe pattern [217]. The existing fiber-based sensing platforms realized on the geometry-modified fibers, such as long period grating (LPG) and tilted fiber Bragg grating (TFBG), suffer from poor mechanical stability and complicated fabrication process [3,138,226]. Therefore, currently, there is no technique allowing noncontact characterization of the fiber coatings *in situ*. SEM analysis of LbL functionalized MOFs has been found as the only reliable method for the estimation of coating thickness of the geometrically confined fiber surface [14]. However, since most of the commercial fibers are made of silica and its counterparts [227], an extra deposition of conductive metals required for the proper imaging decreases the contrast between fiber walls and functional coating and does not allow resolving nanometer-thin films [14]. Overall, there is a strong demand for real-time

monitoring of the coating growth during the self-assembly on the fiber surface. In this contribution, a new technique that resolves this issue has been demonstrated.

7.2 Results and discussion

The holey structure of HC-MOFs supports the simultaneous flow of aqueous solutions and light guidance in the water-filled core. We have succeeded in the growing of LbL PE films consisted of PAH and PSS inside the HC-MOFs and synchronic tracking of the shifts in the position of optical resonances correlating with the thickness of the deposited coating. An increase in the film thicknesses with increasing ionic strength in the PE solutions was experimentally observed for the coatings formed by three PAH/PSS bilayers assembled from the buffers containing 0.15 M and 0.5 M of NaCl [14]. The versatility of the HC-MOF-based platform for monitoring the pH-induced dissolving of nanocoating consisted of BSA and TA was demonstrated as well.

7.2.1 Experimental realization

The experimental analysis of the coating thickness relies on the transmission spectra measurements and tracking the position of optical resonances of liquid-filled HC-MOFs at each stage of multicycle assembly. Liquid filling of fiber capillaries is obtained by inserting the tips of HC-MOFs into small liquid cells (LCs) equipped with tubing interfaces and optically accessible windows. Such a system ensures stable and reproducible measurements at different pumping rates from 100 to 1000 mL min^{-1} [14]. A peristaltic pump (Shenchen LabV1) connected to the inlet of the LC creates the flow of applied solutions through the fiber. Microscope objectives (Olympus, 10x) are used to couple the light from a halogen lamp (Thorlabs SLS201L) into the fibers and to collect the transmitted signal. The output spectrum is analyzed at each step of LBL deposition process and measured with a spectrometer (Ocean Optics QE Pro). The custom algorithm in LabVIEW (Ivan Gnusov wrote the code) [228] allows real-time tracking the spectral positions of minima in the fiber transmission spectra that are related with the coating thickness. Eq. 2.13 provides a convenient link between the position of the dips in the fiber transmission for the fundamental fiber mode only and the thickness of the assembled coating once the coating refractive index is close to the glass refractive index.

7.2.2 *In-situ* monitoring of coating buildup

To demonstrate the feasibility of the proposed technique for the dynamic analysis of different coating performance, the thickness of assembled PAH/PSS films dissolved in buffers containing 0.15 and 0.5 M NaCl were compared. The position of optical resonances for the water-filled non-modified HC-MOF serves as a reference for the following extraction of the coating thickness (Figure 7.1).
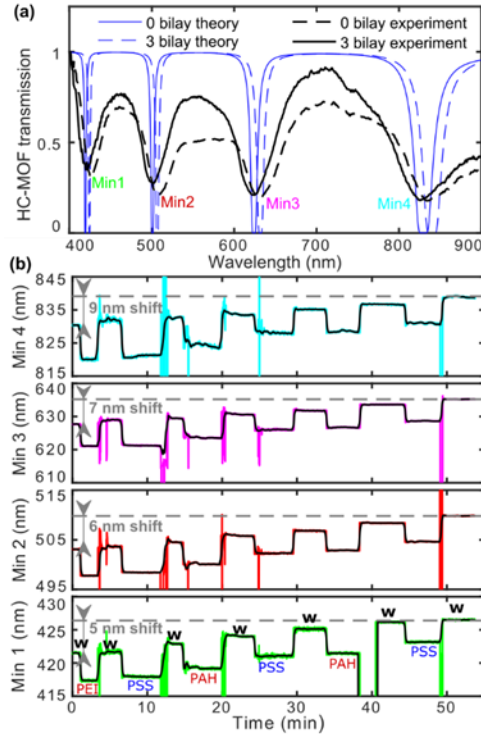
Figure 7-1: (a) Comparison of the experimental and theoretical transmission spectra for the water-filled non-modified and coated by the PEs dissolved in a buffer containing 0.15 M NaCl HC-MOF. The theoretical plot was obtained by adjusting the thickness of the polymer coating as 18 nm per 3 PAH/PSS bilayers. The experimental data summarizes the transmission spectra of a bare (nonmodified) fiber and a fiber coated with 3 PAH/PSS bilayers. (b) The spectral evolution of the transmission minima associated with LbL assembly. The colour lines indicate instantaneous positions of the transmission minima when the peristaltic pump is switched between PE solutions and deionized water (w). The black lines exhibit the data smoothed with MATLAB.

The thickness of fiber coating is evaluated via adjustment of the coating thickness in the theoretical model to get a coincidence with the experimental transmission spectrum (Figure 7.1a). The polymer coating is included into the theoretical model as an additional concentric layer of equal thickness on the core capillary [14]. For a coating consisted of 3 PE bilayers formed in the buffer containing 0.15 M NaCl, the spectral shifts of optical resonances were 5, 6, 7 and 9 nm for various minima in fiber transmission (Figure 7.1b) that corresponds to the formation of polymer coating with a thickness of 18 nm, which has been also verified by SEM (Figure 7.2b).
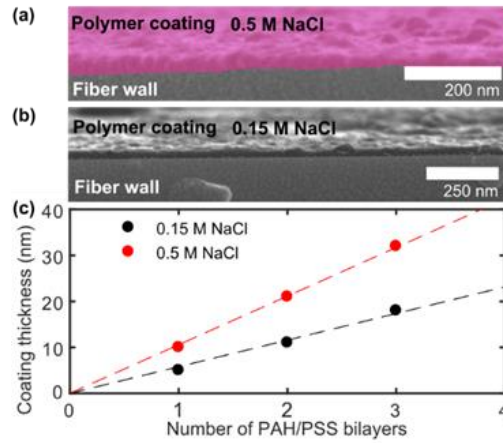
Figure 7-2: SEM micrographs of the core capillaries functionalized with 3 PAH/PSS bilayers in the presence of (a) 0.5 and (b) 0.15 M NaCl, respectively. (c) Coating thickness vs the number of PE bilayers. The coating thickness is evaluated from the shifts in the fiber transmission windows (points). Lines correspond to the thickness of 5.8 nm (0.15 M NaCl) and 10.6 nm (0.5 M NaCl) per single bilayer.

An increase in the film thicknesses with increasing ionic strength in the PE solutions from 0.15 to 0.5 M NaCl was observed. The higher salt concentration changes the molecular conformation from the linear to the globular or coiled structure. Thus, for a polymer coating consisted of 3 PAH/PSS bilayers formed in the buffer containing 0.5 M NaCl, the spectral shifts of optical resonances were 8, 12, 13 and 17 nm for various minima. This, in turn, corresponds to the formation of a 32-nm PE film on the inner surface of HC, confirmed by SEM (Figure 7.2a).

Hence, the average thickness increase of 6 ± 1 and 11 ± 1 nm per bilayer was extracted for the PE solutions in the presence of 0.15 M and 0.5 M NaCl, respectively (Figure 7.2c) [14]. These results are in good agreement with the postdeposition analysis based on transmission spectra measurements of dried functionalized HC-MOFs proving the accuracy of *in situ* characterization of LbL assembled films. Thus, the proposed technique for the evaluation of coating performance can be a promising alternative to the existing methods applied for the thickness analysis of the sequentially assembled multilayers. In particular, to SEM micrographs which are suffering from a poor contrast between the deposited films and fiber surface that does not allow to resolve the nanometer-thin films (Figure 7.2a,b).

SEM micrographs show coating formation on the internal surface of the central capillary only despite solution injection in all fiber capillaries. This effect can be explained by the enormous difference in the hydraulic resistance of the central and side capillaries. The Hagen−Poiseuille model [187] states that the capillary hydraulic resistance is inversely proportional to its radius to the fourth power that means that a flow rate in the side channels is at least 1000 times slower than in the core channel for our fiber. Thus, for the typical coating deposition duration (~10-60 min) the film is formed on the inner surface of the central capillary only.

7.2.3 *In-situ* monitoring of coating disintegration

Finally, we demonstrate the performance of our technique for real-time monitoring of the coating dissolving. We employ BSA/TA complex as a coating since it was demonstrated that the binding inside this composite is very sensitive to the pH level of the surrounding media [188]. Thus, the solutions at low (acidic) and higher (alkaline) pH prevent and/or partially reduce protein binding and induce the dissociation of existed BSA/TA networks.

The adsorption of the BSA/TA multilayers leads to a slight red-shift while pH-annealing, in turn, induces the blue-shift of optical resonances due to the disintegration of BSA/TA coating from the cladding ring [138]. Figure 7.3 summarizes the coating evolution and the associated spectral shift of transmission minimum during the immersion with the

alkalic solution at pH 9 and pH 11 for the fibers functionalized with 4 and 8 BSA/TA bilayers. The pump flow rate was set to 150 μL min^{-1}. The longest wavelength transmission minimum (Min 4) has been chosen for the study since it possesses the highest sensitivity to the thickness variations (Eq. 2.13).
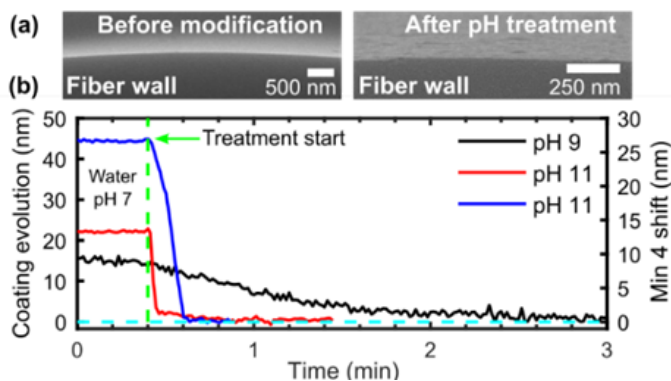
Figure 7-3: (a) SEM micrographs of the uncoated fiber and the fiber functionalized with BSA/TA multilayers followed by the alkaline treatment. (b) In situ monitoring of the BSA/TA coating disintegration (black and red line – 4 BSA/TA bilayers upon the treatment by pH 9 and 11, respectively. Blue - 8 BSA/TA bilayers treated by pH 11. The green line indicates the start of the alkaline treatment.

The spectral shift of resonant wavelength to the initial position after the alkaline treatment of functionalized HC-MOFs indicates the complete removal of BSA/TA films from the capillary walls that has been also verified by SEM micrographs (Figure 7.3a). The stable position of transmission minimum after ~2 min of the treatment at pH 9 suggests completion of the dissolution process. The kinetics of coating removing upon the treatment at pH 11 shows the much faster decay for the coatings with thicknesses of ~20 and ~45 nm (Figure 7.3b). Therefore, a variation in the pH level of the alkaline solution has a strong effect on the kinetics of removing of BSA/TA coating upon the treatment. Thus, the complete removal of the functional layers may vary from a few seconds to a couple of minutes depending on the pH level of the applied solution.

7.3 Summary
To sum up, the proposed technique for the *in situ* monitoring of LbL assembly of PE multilayers inside the HC-MOFs allows to overcome the current limitations hindering

the biomedical applications of optical fiber-based endoscopic probes and sensors. The dynamic measurements based on the tracking of optical resonances enable the noncontact analysis of the adsorption/desorption processes on the fiber surface. As an optofluidic platform, the HC-MOF-based module provides exciting opportunities for fundamental studies of the LbL process in various types of hollow fibers. Considering the multifunctionality of LbL assembled layers, the designed system offers excellent potential for the development of robust sensors for monitoring both the growth of functional materials and their release under various conditions.

8. Conclusions and future research

In the present thesis, optical properties of hollow-core microstructured fibers modified by polymers and/or inorganic nano- and submicron particles have been studied. Thus, the layer-by-layer modification technique, which has been used to create functional nanocoating in the inner surface of the fiber capillaries, allowed to tune the position of transmission windows in a highly controllable and reproducible way over the broad spectral range from 400 nm to 900 nm introducing an extra attenuation of ~0.02 dB cm^{-1} per single assembled PAH/PSS bilayer. It has been also demonstrated that the thickness and morphology of deposited polymer coating can be controlled through the variation of the salt concentration in the buffer solution. In particular, the average thickness increasing of 1.8 ± 0.3 nm and 7.0 ± 1.3 nm per single PAH/PSS bilayer for the salt-free PE solutions and in the presence of 0.15 M NaCl, respectively, has been observed [14]. Exploiting the set of modified HC-MOFs with slightly shifted transmission windows for the in-fiber multispectral sensing allows the simultaneous measurement of the optical dispersion of biological liquids at many wavelengths in the visible and near-infrared spectral domains. For example, the extraction of the refractive index of bovine serum albumin is possible with refractive index sensitivity values up to ~3000 nm RIU^{-1} and a figure of merit reaching 99 RIU^{-1} [14]. Moreover, the use of the proposed sensing technique has been proved to measure the optical dispersion and concentration of bovine serum albumin dissolved in water and PBS buffers in both static and dynamic regimes, with a resolution of ~1 g L^{-1} [14].

For the first time to our knowledge, the LBL technique for HC-MOF modification through the deposition of silica particles with different sizes (300, 420, and 900 nm) onto capillary surfaces has been presented. The potential for the creation of multilayer porous coating was demonstrated on the example of one, two, and three layers of 300-nm silica particles. The largest spectral shift in the transmission is induced by the first deposited silica layer (31 nm and 39 nm, for the first and the second transmission bands, respectively), while additional silica layers are worse-adsorbed on the first layer of particles, resulting in the additional transmission spectral shifts (11 nm and 7 nm). The limitation of this

technique has been shown in the example of silica particles at the diameters of 900 nm, the bigger particles form the rough coating and disturb the light guidance inside HC-MOFs [99].

The porous silica coatings have been also realized on the sensitive surface of 1D photonic crystal sensors for the creation of functional coatings of different nature: hydrophilic and hydrophobic. Taking into account that condensation in the pores occurs at the lowest partial gas pressures the designed sensor structure shows promising characteristics to detect the changes in surround relative humidity [176].

Ultrasmooth, biocompatible, and removable nanocoating for HC-MOFs has been introduced by BSA/TA complexes. To smooth the BSA/TA substrate, alkaline etching has been applied. The temporal kinetics of the coating dissolution shows that the alkali drops the surface roughness to 3 nm within 4 min of the treatment, resulting in decreasing the fiber optical losses by three times. The coating is fully removed in 7 min of the treatment. Thus, considering the induced optical losses introduced by functional coatings, the post-processing techniques directing to the smoothing of the initial rough coatings would be an asset to the field of hybrid optical fibers.

The overall idea of functionalized optical fibers is the integration of materials, which are traditionally not used in fiber optics, directly into fiber capillaries, for a controllable tuning of the fiber optical properties and to bring novel functionalities expanding the fields of applications to novel critical areas such as biophotonics, environmental science or chemical and biochemical sensing [2]. The functionalized hollow-core fibers investigated in this thesis represent the structures with unique properties that generally highlight the potential of this research field from a device and applications perspective. This research direction has been triggered by improvements in fiber fabrication technology and by the emergence of post-processing techniques, accompanied by the investigation of new material combinations. From a practical point of view, the anticipated applications of functionalized MOF are fiber-based sensors, endoscopic probes, and drug delivery tools.

Bibliography

1. J. C. Knight, T. A. Birks, P. S. J. Russell, and D. M. Atkin, "All-silica single-mode optical fiber with photonic crystal cladding," Optics Letters **21**(19), 1547–1549 (1996).
2. M. A. Schmidt, A. Argyros, and F. Sorin, "Hybrid Optical Fibers - An Innovative Platform for In-Fiber Photonic Devices," Advanced Optical Materials **4**(1), 13–36 (2016).
3. T. Ermatov, J. S. Skibina, V. V. Tuchin, and D. A. Gorin, "Functionalized Microstructured Optical Fibers: Materials Methods Applications," Materials **13**(4), 921 (2020).
4. C. M. B. Cordeiro, C. J. S. de Matos, E. M. dos Santos, A. Bozolan, J. S. K. Ong, T. Facincani, G. Chesini, A. R. Vaz, and C. H. Brito Cruz, "Towards practical liquid and gas sensing with photonic crystal fibres: side access to the fibre microstructure and single-mode liquid-core fibre," Measurement Science and Technology **18**(10), 3075–3081 (2007).
5. W. Ding, Y. Wang, S. Gao, M. Wang, and P. Wang, "Recent Progress in Low-Loss Hollow-Core Anti-Resonant Fibers and Their Applications," IEEE Journal of Selected Topics in Quantum Electronics **26**(4), 1–12 (2020).
6. P. Russell, "Photonic Crystal Fibers," Science **299**(5605), 358 LP – 362 (2003).
7. X. D. Wang and O. S. Wolfbeis, "Fiber-Optic Chemical Sensors and Biosensors (2013-2015)," Analytical Chemistry (2016).
8. T. A. Birks, J. C. Knight, and P. S. J. Russell, "Endlessly single-mode photonic crystal fiber," Optics Letters **22**(13), 961–963 (1997).
9. P. J. Roberts, F. Couny, H. Sabert, B. J. Mangan, D. P. Williams, L. Farr, M. W. Mason, A. Tomlinson, T. A. Birks, J. C. Knight, and P. S. J. Russell, "Ultimate low loss of hollow-core photonic crystal fibres," Optics Express **13**(1), 236–244 (2005).
10. S. Perevoschikov, N. Kaydanov, T. Ermatov, O. Bibikova, I. Usenov, T. Sakharova, A. Bocharnikov, J. Skibina, V. Artyushenko, and D. Gorin, "Light guidance up to 6.5 μm in borosilicate soft glass hollow-core microstructured optical waveguides," Optics Express **28**(19), 27940–27950 (2020).
11. A. M. Cubillas, S. Unterkofler, T. G. Euser, B. J. M. Etzold, A. C. Jones, P. J. Sadler, P. Wasserscheid, and P. S. J. Russell, "Photonic crystal fibres for chemical sensing and photochemistry," Chemical Society Reviews **42**(22), 8629–8648 (2013).
12. U. S. Dinish, F. Beffara, G. Humbert, J. Auguste, and M. Olivo, "Surface-enhanced Raman scattering-active photonic crystal fiber probe: Towards next generation liquid biopsy sensor with ultra high sensitivity," Journal of Biophotonics **12**(11), e201900027 (2019).
13. B. Doherty, A. Csáki, M. Thiele, M. Zeisberger, A. Schwuchow, J. Kobelke, W. Fritzsche, and M. A. Schmidt, "Nanoparticle functionalised small-core suspended-core fibre – a novel platform for efficient sensing," Biomedical Optics Express **8**(2), 790 (2017).

14. T. Ermatov, R. E. Noskov, A. A. Machnev, I. Gnusov, V. Atkin, E. N. Lazareva, S. V German, S. S. Kosolobov, T. S. Zatsepin, O. V Sergeeva, J. S. Skibina, P. Ginzburg, V. V Tuchin, P. G. Lagoudakis, and D. A. Gorin, "Multispectral sensing of biological liquids with hollow-core microstructured optical fibres," Light: Science & Applications **9**(1), 173 (2020).

15. A. Knebl, D. Yan, J. Popp, and T. Frosch, "Fiber enhanced Raman gas spectroscopy," TrAC Trends in Analytical Chemistry **103**, 230–238 (2018).

16. B. B. Hsu, S. R. Hagerman, K. Jamieson, J. Veselinovic, N. O'Neill, E. Holler, J. Y. Ljubimova, and P. T. Hammond, "Multilayer Films Assembled from Naturally-Derived Materials for Controlled Protein Release," Biomacromolecules **15**(6), 2049–2057 (2014).

17. I. Zhuk, F. Jariwala, A. B. Attygalle, Y. Wu, M. R. Libera, and S. A. Sukhishvili, "Self-Defensive Layer-by-Layer Films with Bacteria-Triggered Antibiotic Release," ACS Nano **8**(8), 7733–7745 (2014).

18. F. Yesilkoy, R. A. Terborg, J. Pello, A. A. Belushkin, Y. Jahani, V. Pruneri, and H. Altug, "Phase-sensitive plasmonic biosensor using a portable and large field-of-view interferometric microarray imager," Light: Science & Applications **7**(2), 17152 (2018).

19. F. Yesilkoy, E. R. Arvelo, Y. Jahani, M. Liu, A. Tittl, V. Cevher, Y. Kivshar, and H. Altug, "Ultrasensitive hyperspectral imaging and biodetection enabled by dielectric metasurfaces," Nature Photonics **13**(6), 390–396 (2019).

20. K. V. Sreekanth, Y. Alapan, M. ElKabbash, E. Ilker, M. Hinczewski, U. A. Gurkan, A. De Luca, and G. Strangi, "Extreme sensitivity biosensing platform based on hyperbolic metamaterials," Nature Materials **15**(6), 621–627 (2016).

21. Y. Xu, P. Bai, X. Zhou, Y. Akimov, C. E. Png, L. Ang, W. Knoll, and L. Wu, "Optical Refractive Index Sensors with Plasmonic and Photonic Structures: Promising and Inconvenient Truth," Advanced Optical Materials **7**(9), 1801433 (2019).

22. S. Jahani and Z. Jacob, "Breakthroughs in Photonics 2014: Relaxed Total Internal Reflection," IEEE Photonics Journal **7**(3), 1–5 (2015).

23. J. D. Colladon, "On the reflections of a ray of light inside a parabolic liquid stream," Comptes Rendus **15**, 800–802 (1842).

24. J. Hecht, "City of Light: The Story of Fiber Optics," in (1999).

25. H. Lamm, "Biegsame optische Gerate," Zeitschrift fur Instrumeten Kunde **50**, 579–581 (1930).

26. H. H. Hopkins and N. S. Kapany, "A Flexible Fibrescope, using Static Scanning," Nature **173**(4392), 39–41 (1954).

27. K. Kao and G. Hockham, "Dielectric-fibre surface waveguides for optical frequencies," in *Proceedings of the Institution of Electrical Engineers* (1966), pp. 1151–1158.

28. C. Lin, "In memory of Charles Kao," Nature Photonics **12**(12), 715–717 (2018).

29. R. F. Cregan, B. J. Mangan, J. C. Knight, T. A. Birks, P. S. Russell, P. J. Roberts, and D. C. Allan, "Single-Mode Photonic Band Gap Guidance of Light in Air.," Science (New York, N.Y.) **285**(5433), 1537–1539 (1999).

30. P. S. J. Russell, "Photonic-Crystal Fibers," Journal of Lightwave Technology **24**(12), 4729–4749 (2006).

31. F. Poletti, M. N. Petrovich, and D. J. Richardson, "Hollow-core photonic bandgap fibers: technology and applications," Nanophotonics **2**(5–6), 315–340 (2013).

32. A. Hartung, J. Kobelke, A. Schwuchow, J. Bierlich, J. Popp, M. A. Schmidt, and T. Frosch, "Low-loss single-mode guidance in large-core antiresonant hollow-core fibers," Optics Letters **40**(14), 3432–3435 (2015).

33. N. V Wheeler, A. M. Heidt, N. K. Baddela, E. N. Fokoua, J. R. Hayes, S. R. Sandoghchi, F. Poletti, M. N. Petrovich, and D. J. Richardson, "Low-loss and low-bend-sensitivity mid-infrared guidance in a hollow-core photonic-bandgap fiber," Optics Letters **39**(2), 295–298 (2014).

34. A. Ward and J. Pendry, "Refraction and geometry in Maxwell's equations," Journal of Modern Optics **43**, 773–793 (1996).

35. N. Granzow, "Microstructured Optical Fibers with Incorporated Nonlinear Glasses," (2013).

36. V. A. Markel, "Introduction to the Maxwell Garnett approximation: tutorial," Journal of the Optical Society of America A **33**(7), 1244–1256 (2016).

37. O. Levy and E. Cherkaev, "Effective medium approximations for anisotropic composites with arbitrary component orientation," Journal of Applied Physics **114**(16), 164102 (2013).

38. P. Yeh, "Optical waves in layered media: Ch 11 b," in *Optical Waves in Layered Media* (2005).

39. N. Mahnot, S. Maheshwary, and R. Mehra, "PHOTONIC CRYSTAL FIBER- AN OVERVIEW," International Journal of Scientific & Engineering Research **6**(2), 2229–5518 (2015).

40. E. A. J. Marcatili and R. A. Schmeltzer, "Hollow Metallic and Dielectric Waveguides for Long Distance Optical Transmission and Lasers," Bell System Technical Journal **43**(4), 1783–1809 (1964).

41. I. Bufetov, A. Kosolapov, A. Pryamikov, A. Gladyshev, A. Kolyadin, A. Krylov, Y. Yatsenko, and A. Biriukov, "Revolver Hollow Core Optical Fibers," Fibers **6**, 39 (2018).

42. N. M. Litchinitser, A. K. Abeeluck, C. Headley, and B. J. Eggleton, "Antiresonant reflecting photonic crystal optical waveguides," Optics Letters **27**(18), 1592–1594 (2002).

43. A. A. Machnev, A. P. Pushkarev, P. Tonkaev, R. E. Noskov, K. R. Rusimova, P. J. Mosley, S. V Makarov, P. B. Ginzburg, and I. I. Shishkin, "Modifying light–matter interactions with perovskite nanocrystals inside antiresonant photonic crystal fiber," Photonics Research **9**(8), 1462–1469 (2021).

44. R. E. Noskov, A. A. Zanishevskaya, A. A. Shuvalov, S. V. German, O. A. Inozemtseva, T. P. Kochergin, E. N. Lazareva, V. V. Tuchin, P. Ginzburg, J. S. Skibina, and D. A. Gorin, "Enabling magnetic resonance imaging of hollow-core microstructured optical fibers via nanocomposite coating," Optics Express **27**(7), 9868–9878 (2019).

45. B. D. Gupta and R. K. Verma, "Surface plasmon resonance-based fiber optic

sensors: Principle, probe designs, and some applications," Journal of Sensors **2009**, (2009).

46. A. Hassani and M. Skorobogatiy, "Design of the microstructured optical fiber-based surface plasmon resonance sensors with enhanced microfluidics," Optics Express **14**(24), 11616 (2006).

47. S. Unser, I. Bruzas, J. He, and L. Sagle, "Localized surface plasmon resonance biosensing: Current challenges and approaches," Sensors (Switzerland) **15**(7), 15684–15716 (2015).

48. B. Sciacca and T. M. Monro, "Dip biosensor based on localized surface plasmon resonance at the tip of an optical fiber," Langmuir **30**(3), 946–954 (2014).

49. I. Del Villar, F. J. Arregui, C. R. Zamarreño, J. M. Corres, C. Bariain, J. Goicoechea, C. Elosua, M. Hernaez, P. J. Rivero, A. B. Socorro, A. Urrutia, P. Sanchez, P. Zubiate, D. Lopez, N. De Acha, J. Ascorbe, and I. R. Matias, "Optical sensors based on lossy-mode resonances," Sensors and Actuators, B: Chemical **240**, 174–185 (2017).

50. C. Caucheteur, T. Guo, and J. Albert, "Review of plasmonic fiber optic biochemical sensors: improving the limit of detection," Analytical and bioanalytical chemistry **407**(14), 3883–3897 (2015).

51. M. Calcerrada, C. García-Ruiz, and M. González-Herráez, "Chemical and biochemical sensing applications of microstructured optical fiber-based systems," Laser and Photonics Reviews **9**(6), 604–627 (2015).

52. E. Klantsataya, P. Jia, H. Ebendorff-Heidepriem, T. M. Monro, and A. François, "Plasmonic fiber optic refractometric sensors: From conventional architectures to recent design trends," Sensors (Switzerland) **17**(1), (2017).

53. B. T. Wang and Q. Wang, "An interferometric optical fiber biosensor with high sensitivity for IgG/anti-IgG immunosensing," Optics Communications **426**, 388–394 (2018).

54. O. Yavas, M. Svedendahl, P. Dobosz, V. Sanz, and R. Quidant, "On-a-chip Biosensing Based on All-Dielectric Nanoresonators," Nano Letters **17**(7), 4421–4426 (2017).

55. F. Chiavaioli, P. Zubiate, I. Del Villar, C. R. Zamarrenìo, A. Giannetti, S. Tombelli, C. Trono, F. J. Arregui, I. R. Matias, and F. Baldini, "Femtomolar Detection by Nanocoated Fiber Label-Free Biosensors," ACS Sensors **3**(5), 936–943 (2018).

56. P. Uebel, S. T. Bauerschmidt, M. A. Schmidt, and P. St.j. Russell, "A gold-nanotip optical fiber for plasmon-enhanced near-field detection," Applied Physics Letters **103**(2), (2013).

57. B. Lee, S. Roh, and J. Park, "Current status of micro- and nano-structured optical fiber sensors," Optical Fiber Technology **15**(3), 209–221 (2009).

58. G. Quero, A. Crescitelli, D. Paladino, M. Consales, A. Buosciolo, M. Giordano, A. Cutolo, and A. Cusano, "Evanescent wave long-period fiber grating within D-shaped optical fibers for high sensitivity refractive index detection," Sensors and Actuators, B: Chemical **152**(2), 196–205 (2011).

59. T. M. Monro, S. Warren-Smith, E. P. Schartner, A. Franois, S. Heng, H.

Ebendorff-Heidepriem, and S. Afshar, "Sensing with suspended-core optical fibers," Optical Fiber Technology **16**(6), 343–356 (2010).

60. M. H. Frosz, A. Stefani, and O. Bang, "Highly sensitive and simple method for refractive index sensing of liquids in microstructured optical fibers using four-wave mixing," Optics Express **19**(11), 10471 (2011).

61. D. Cialla-May, X.-S. Zheng, K. Weber, and J. Popp, "Recent progress in surface-enhanced Raman spectroscopy for biological and biomedical applications: from cells to clinics," Chemical Society Reviews **46**(13), 3945–3961 (2017).

62. K. Xu, R. Zhou, K. Takei, and M. Hong, "Toward Flexible Surface-Enhanced Raman Scattering (SERS) Sensors for Point-of-Care Diagnostics," Advanced Science **6**(16), 1900925 (2019).

63. S. Mariani, V. Robbiano, L. M. Strambini, A. Debrassi, G. Egri, L. Dähne, and G. Barillaro, "Layer-by-layer biofunctionalization of nanostructured porous silicon for high-sensitivity and high-selectivity label-free affinity biosensing," Nature Communications **9**(1), 5256 (2018).

64. X. Fan, I. M. White, S. I. Shopova, H. Zhu, J. D. Suter, and Y. Sun, "Sensitive optical biosensors for unlabeled targets: A review," Analytica Chimica Acta **620**(1–2), 8–26 (2008).

65. U. S. Dinish, C. Y. Fu, K. S. Soh, B. Ramaswamy, A. Kumar, and M. Olivo, "Highly sensitive SERS detection of cancer proteins in low sample volume using hollow core photonic crystal fiber," Biosensors and Bioelectronics **33**(1), 293–298 (2012).

66. U. S. Dinish, G. Balasundaram, Y. T. Chang, and M. Olivo, "Sensitive multiplex detection of serological liver cancer biomarkers using SERS-active photonic crystal fiber probe," Journal of Biophotonics **7**(11–12), 956–965 (2014).

67. E. Coscelli, M. Sozzi, F. Poli, D. Passaro, A. Cucinotta, S. Selleri, R. Corradini, and R. Marchelli, "Toward a highly specific DNA biosensor: PNA-modified suspended-core photonic crystal fibers," IEEE Journal on Selected Topics in Quantum Electronics **16**(4), 967–972 (2010).

68. M. Barozzi, A. Manicardi, A. Vannucci, A. Candiani, M. Sozzi, M. Konstantaki, S. Pissadakis, R. Corradini, S. Selleri, and A. Cucinotta, "Optical Fiber Sensors for Label-Free DNA Detection," Journal of Lightwave Technology **35**(16), 3461–3472 (2017).

69. A. Bertucci, A. Manicardi, A. Candiani, S. Giannetti, A. Cucinotta, G. Spoto, M. Konstantaki, S. Pissadakis, S. Selleri, and R. Corradini, "Detection of unamplified genomic DNA by a PNA-based microstructured optical fiber (MOF) Bragg-grating optofluidic system," Biosensors and Bioelectronics **63**, 248–254 (2015).

70. L. V. Nguyen, S. C. Warren-Smith, A. Cooper, and T. M. Monro, "Molecular beacons immobilized within suspended core optical fiber for specific DNA detection," Optics Express **20**(28), 29378 (2012).

71. G. Decher, "Fuzzy nanoassemblies: Toward layered polymeric multicomposites," Science **277**(5330), 1232–1237 (1997).

72. Y. Han, S. Tan, M. K. Khaing Oo, D. Pristinski, S. Sukhishvili, and H. Du, "Towards full-length accumulative surface-enhanced raman Scattering-Active

photonic crystal fibers," Advanced Materials (2010).

73. Y. Han, S. Tan, M. K. Khaing Oo, D. Pristinski, S. Sukhishvili, and H. Du, "Towards full-length accumulative surface-enhanced raman Scattering-Active photonic crystal fibers," Advanced Materials **22**(24), 2647–2651 (2010).

74. G.-H. Lee, H. Moon, H. Kim, G. H. Lee, W. Kwon, S. Yoo, D. Myung, S. H. Yun, Z. Bao, and S. K. Hahn, "Multifunctional materials for implantable and wearable photonic healthcare devices," Nature Reviews Materials (2020).

75. J. F. Algorri, D. C. Zografopoulos, A. Tapetado, D. Poudereux, and J. M. Sánchez-Pena, "Infiltrated photonic crystal fibers for sensing applications," Sensors (Switzerland) **18**(12), (2018).

76. S. A. Pidenko, N. A. Burmistrova, A. A. Shuvalov, A. A. Chibrova, Y. S. Skibina, and I. Y. Goryacheva, "Microstructured optical fiber-based luminescent biosensing: Is there any light at the end of the tunnel? - A review," Analytica Chimica Acta **1019**, 14–24 (2018).

77. E. P. Schartner, G. Tsiminis, A. François, R. Kostecki, S. C. Warren-Smith, L. V. Nguyen, S. Heng, T. Reynolds, E. Klantsataya, K. J. Rowland, A. D. Abell, H. Ebendorff-Heidepriem, and T. M. Monro, "Taming the Light in Microstructured Optical Fibers for Sensing," International Journal of Applied Glass Science **6**(3), 229–239 (2015).

78. A. M. Zheltikov, "Microstructure Fibers in Biophotonics," in *Handbook of Biophotonics*, A. C. and S. H. H. J. Popp, V.V. Tuchin, ed., Major Reference Works (WILEY-VCH Verlag GmbH & Co. KGaA, 2013), pp. 77–103.

79. J. Li, H. Ebendorff-Heidepriem, B. C. Gibson, A. D. Greentree, M. R. Hutchinson, P. Jia, R. Kostecki, G. Liu, A. Orth, M. Ploschner, E. P. Schartner, S. C. Warren-Smith, K. Zhang, G. Tsiminis, and E. M. Goldys, "Perspective: Biomedical sensing and imaging with optical fibers - Innovation through convergence of science disciplines," APL Photonics **3**(10), (2018).

80. W. Talataisong, R. Ismaeel, M. Beresna, and G. Brambilla, "Suspended-core microstructured polymer optical fibers and potential applications in sensing," Sensors (Switzerland) **19**(16), (2019).

81. A. Schwuchow, M. Zobel, A. Csaki, K. Schröder, J. Kobelke, W. Fritzsche, and K. Schuster, "Monolayers of different metal nanoparticles in microstructured optical fibers with multiplex plasmonic properties," Optical Materials Express **2**(8), 1050 (2012).

82. A. Cerqueira S., Jr., C. M. B. Cordeiro, F. Biancalana, P. J. Roberts, H. E. Hernandez-Figueroa, and C. H. B. Cruz, "Nonlinear interaction between two different photonic bandgaps of a hybrid photonic crystal fiber," Optics Letters **33**(18), 2080 (2008).

83. C. J. De Matos, C. M. B. Cordeiro, E. M. dos Santos, J. S. Ong, A. Bozolan, and C. H. Brito Cruz, "Liquid-core, liquid-cladding photonic crystal fibers," Optics Express **15**(18), 11207 (2007).

84. S. A. Pidenko, N. A. Burmistrova, P. S. Pidenko, A. A. Shuvalov, A. A. Chibrova, Y. S. Skibina, and I. Y. Goryacheva, "Controlled chemical modification of the internal surface of photonic crystal fibers for application as biosensitive elements,"

Optical Materials **60**, 283–289 (2016).

85. M. K. K. Oo, Y. Han, R. Martini, S. Sukhishvili, and H. Du, "Forward-propagating surface-enhanced Raman scattering and intensity distribution in photonic crystal fiber with immobilized Ag nanoparticles," Optics Letters **34**(7), 968 (2009).

86. A. Csaki, F. Jahn, I. Latka, T. Henkel, D. Malsch, T. Schneider, K. Schröder, K. Schuster, A. Schwuchow, R. Spittel, D. Zopf, and W. Fritzsche, "Nanoparticle layer deposition for plasmonic tuning of microstructured optical fibers," Small **6**(22), 2584–2589 (2010).

87. K. Schröder, A. Csáki, A. Schwuchow, F. Jahn, K. Strelau, I. Latka, T. Henkel, D. Malsch, K. Schuster, K. Weber, T. Schneider, R. Möller, and W. Fritzsche, "Functionalization of microstructured optical fibers by internal nanoparticle mono-layers for plasmonic biosensor applications," IEEE Sensors Journal **12**(1), 218–224 (2012).

88. S. Ponce, M. Munoz, A. M. Cubillas, T. G. Euser, G. R. Zhang, P. S. J. Russell, P. Wasserscheid, and B. J. M. Etzold, "Stable Immobilization of Size-Controlled Bimetallic Nanoparticles in Photonic Crystal Fiber Microreactor," Chemie-Ingenieur-Technik **90**(5), 653–659 (2018).

89. N. Zhang, K. Li, Y. Cui, Z. Wu, P. P. Shum, J. L. Auguste, X. Q. Dinh, G. Humbert, and L. Wei, "Ultra-sensitive chemical and biological analysis: Via specialty fibers with built-in microstructured optofluidic channels," Lab on a Chip **18**(4), 655–661 (2018).

90. S. Heng, C. A. McDevitt, R. Kostecki, J. R. Morey, B. A. Eijkelkamp, H. Ebendorff-Heidepriem, T. M. Monro, and A. D. Abell, "Microstructured Optical Fiber-based Biosensors: Reversible and Nanoliter-Scale Measurement of Zinc Ions," ACS Applied Materials and Interfaces **8**(20), 12727–12732 (2016).

91. S. C. Warren-Smith, S. Heng, H. Ebendorff-Heidepriem, A. D. Abell, and T. M. Monro, "Fluorescence-based aluminum ion sensing using a surface-functionalized microstructured optical fiber," Langmuir **27**(9), 5680–5685 (2011).

92. S. Heng, M. C. Nguyen, R. Kostecki, T. M. Monro, and A. D. Abell, "Nanoliter-scale, regenerable ion sensor: Sensing with a surface functionalized microstructured optical fibre," RSC Advances **3**(22), 8308–8317 (2013).

93. H. K. Tyagi, M. A. Schmidt, L. Prill Sempere, and P. S. Russell, "Optical properties of photonic crystal fiber with integral micron-sized Ge wire," Optics Express **16**(22), 17227 (2008).

94. N. Granzow, M. A. Schmidt, W. Chang, L. Wang, Q. Coulombier, J. Troles, P. Toupin, I. Hartl, K. F. Lee, M. E. Fermann, L. Wondraczek, and P. S. J. Russell, "Mid-infrared supercontinuum generation in As_2S_3-silica "nano-spike" step-index waveguide," Optics Express **21**(9), 10969 (2013).

95. M. Chemnitz, J. Wei, C. Jain, B. P. Rodrigues, T. Wieduwilt, J. Kobelke, L. Wondraczek, and M. A. Schmidt, "Octave-spanning supercontinuum generation in hybrid silver metaphosphate/silica step-index fibers," Optics Letters **41**(15), 3519 (2016).

96. C. Gaida, M. Gebhardt, P. Kadwani, L. Leick, J. Broeng, L. Shah, and M. Richardson, "Amplification of nanosecond pulses to megawatt peak power levels

in Tm^3+-doped photonic crystal fiber rod," Optics Letters **38**(5), 691 (2013).

97. C. Gaida, P. Kadwani, L. Leick, J. Broeng, L. Shah, and M. Richardson, "CW-lasing and amplification in Tm^3+-doped photonic crystal fiber rod," Optics Letters **37**(21), 4513 (2012).

98. X. Fan, M. Chen, A. Shirakawa, K. Ueda, C. B. Olausson, J. K. Lyngsø, and J. Broeng, "High power Yb-doped photonic bandgap fiber oscillator at 1178 nm," Optics Express **20**(13), 14471 (2012).

99. T. Ermatov, Y. V. Petrov, S. V. German, A. A. Zanishevskaya, A. A. Shuvalov, V. Atkin, A. Zakharevich, B. N. Khlebtsov, J. S. Skibina, P. Ginzburg, R. E. Noskov, V. V. Tuchin, and D. A. Gorin, "Microstructured optical waveguide-based endoscopic probe coated with silica submicron particles," Materials **12**(9), 1424 (2019).

100. A. Bozolan, R. M. Gerosa, C. J. S. De Matos, and M. A. Romero, "Temperature sensing using colloidal-core photonic crystal fiber," IEEE Sensors Journal **12**(1), 195–200 (2012).

101. L. Ding, Y. Ruan, T. Li, J. Huang, S. C. Warren-Smith, H. Ebendorff-Heidepriem, and T. M. Monro, "Nitric oxide optical fiber sensor based on exposed core fibers and CdTe/CdS quantum dots," Sensors and Actuators, B: Chemical **273**, 9–17 (2018).

102. J. S. W. Mak, A. A. Farah, F. Chen, and A. S. Helmy, "Photonic crystal fiber for efficient Raman scattering of CdTe quantum dots in aqueous solution," ACS Nano **5**(5), 3823–3830 (2011).

103. M. C. Stuart, R. de Vries, and H. Lyklema, "Chapter 2 - Polyelectrolytes," in *Soft Colloids*, J. B. T.-F. of I. and C. S. Lyklema, ed. (Academic Press, 2005), **5**, pp. 2.1-2.84.

104. P. M. Budd, "11 - Polyelectrolytes," in G. Allen and J. C. B. T.-C. P. S. and S. Bevington, eds. (Pergamon, 1989), pp. 215–230.

105. A. Sundaramurthy, "9 - Responsive polyelectrolyte multilayer nanofilms for drug delivery applications," in *Woodhead Publishing Series in Biomaterials*, A. S. H. Makhlouf and N. Y. B. T.-S. R. P. N. for D. D. A. Abu-Thabit Volume 1, eds. (Woodhead Publishing, 2018), pp. 247–266.

106. J. Hiller, J. D. Mendelsohn, and M. F. Rubner, "Reversibly erasable nanoporous anti-reflection coatings from polyelectrolyte multilayers," Nature Materials **1**(1), 59–63 (2002).

107. G. Decher, J. D. Hong, and J. Schmitt, "Buildup of ultrathin multilayer films by a self-assembly process: III. Consecutively alternating adsorption of anionic and cationic polyelectrolytes on charged surfaces," Thin Solid Films **210**–**211**(PART 2), 831–835 (1992).

108. M. Schönhoff, "Layered polyelectrolyte complexes: physics of formation and molecular properties," Journal of Physics: Condensed Matter **15**(49), R1781–R1808 (2003).

109. J. J. Richardson, M. Björnmalm, and F. Caruso, "Technology-driven layer-by-layer assembly of nanofilms," Science **348**(6233), aaa2491 (2015).

110. A. F. Abouraddy, M. Bayindir, G. Benoit, S. D. Hart, K. Kuriki, N. Orf, O.

Shapira, F. Sorin, B. Temelkuran, and Y. Fink, "Towards multimaterial multifunctional fibres that see, hear, sense and communicate," Nature Materials **6**(5), 336–347 (2007).

111. J. J. Richardson, J. Cui, M. Björnmalm, J. A. Braunger, H. Ejima, and F. Caruso, "Innovation in Layer-by-Layer Assembly," Chemical Reviews **116**(23), 14828–14867 (2016).

112. S. T. Dubas and J. B. Schlenoff, "Factors Controlling the Growth of Polyelectrolyte Multilayers," Macromolecules **32**(24), 8153–8160 (1999).

113. D. Lee, Z. Gemici, M. F. Rubner, and R. E. Cohen, "Multilayers of Oppositely Charged SiO2 Nanoparticles: Effect of Surface Charge on Multilayer Assembly," Langmuir **23**(17), 8833–8837 (2007).

114. S. Pavlukhina and S. Sukhishvili, "Polymer assemblies for controlled delivery of bioactive molecules from surfaces," Advanced drug delivery reviews **63**, 822–836 (2011).

115. D. Lee, D. Omolade, R. E. Cohen, and M. F. Rubner, "pH-Dependent Structure and Properties of TiO2/SiO2 Nanoparticle Multilayer Thin Films," Chemistry of Materials **19**(6), 1427–1433 (2007).

116. J. Hiller and M. F. Rubner, "Reversible Molecular Memory and pH-Switchable Swelling Transitions in Polyelectrolyte Multilayers," Macromolecules **36**(11), 4078–4083 (2003).

117. M. V. Lomova, A. I. Brichkina, M. V. Kiryukhin, E. N. Vasina, A. M. Pavlov, D. A. Gorin, G. B. Sukhorukov, and M. N. Antipina, "Multilayer Capsules of Bovine Serum Albumin and Tannic Acid for Controlled Release by Enzymatic Degradation," ACS Applied Materials and Interfaces (2015).

118. H. Lau, R. Murney, N. Yakovlev, M. Novoselova, S. Lim, N. Roy, H. Singh, G. Sukhorukov, B. Haigh, and M. Kiryukhin, "Protein-Tannic Acid Multilayer Films: a Multifunctional Material for Microencapsulation of Food-derived Bioactives," Journal of Colloid and Interface Science **505**, (2017).

119. J. P. DeRocher, P. Mao, J. Han, M. F. Rubner, and R. E. Cohen, "Layer-by-Layer Assembly of Polyelectrolytes in Nanofluidic Devices," Macromolecules **43**(5), 2430–2437 (2010).

120. Y. Svenskaya, B. Parakhonskiy, A. Haase, V. Atkin, E. Lukyanets, D. Gorin, and R. Antolini, "Anticancer drug delivery system based on calcium carbonate particles loaded with a photosensitizer," Biophysical chemistry **182**, 11–15 (2013).

121. D. Furtado, M. Björnmalm, S. Ayton, A. I. Bush, K. Kempe, and F. Caruso, "Overcoming the Blood–Brain Barrier: The Role of Nanomaterials in Treating Neurological Diseases," Advanced Materials **30**(46), 1801362 (2018).

122. S. Zhao, F. Caruso, L. Dähne, G. Decher, B. G. De Geest, J. Fan, N. Feliu, Y. Gogotsi, P. T. Hammond, M. C. Hersam, A. Khademhosseini, N. Kotov, S. Leporatti, Y. Li, F. Lisdat, L. M. Liz-Marzán, S. Moya, P. Mulvaney, A. L. Rogach, S. Roy, D. G. Shchukin, A. G. Skirtach, M. M. Stevens, G. B. Sukhorukov, P. S. Weiss, Z. Yue, D. Zhu, and W. J. Parak, "The Future of Layer-by-Layer Assembly: A Tribute to ACS Nano Associate Editor Helmuth Möhwald," ACS Nano **13**(6), 6151–6169 (2019).

123. R. A. Ghostine, R. M. Jisr, A. Lehaf, and J. B. Schlenoff, "Roughness and Salt Annealing in a Polyelectrolyte Multilayer," Langmuir **29**(37), 11742–11750 (2013).

124. S. S. Shiratori and M. F. Rubner, "pH-Dependent Thickness Behavior of Sequentially Adsorbed Layers of Weak Polyelectrolytes," Macromolecules **33**(11), 4213–4219 (2000).

125. R. A. McAloney, V. Dudnik, and M. C. Goh, "Kinetics of Salt-Induced Annealing of a Polyelectrolyte Multilayer Film Morphology," Langmuir **19**(9), 3947–3952 (2003).

126. H. E. Karahan, L. Eyuboglu, D. Kıyılar, and L. Demirel, "pH-stability and pH-annealing of H-bonded multilayer films prepared by layer-by-layer spin-assembly," European Polymer Journal **56**, 159 —167 (2014).

127. I. Erel-Unal and S. A. Sukhishvili, "Hydrogen-Bonded Hybrid Multilayers: Film Architecture Controls Release of Macromolecules," Macromolecules **41**(22), 8737–8744 (2008).

128. T. Mauser, C. Déjugnat, and G. B. Sukhorukov, "Balance of Hydrophobic and Electrostatic Forces in the pH Response of Weak Polyelectrolyte Capsules," The Journal of Physical Chemistry B **110**(41), 20246–20253 (2006).

129. D. O. Ignatyeva, G. A. Knyazev, P. O. Kapralov, G. Dietler, S. K. Sekatskii, and V. I. Belotelov, "Magneto-optical plasmonic heterostructure with ultranarrow resonance for sensing applications," Scientific Reports **6**(28077), (2016).

130. J. Chochol, K. Postava, M. Čada, and J. Pištora, "Experimental demonstration of magnetoplasmon polariton at InSb(InAs)/dielectric interface for terahertz sensor application," Scientific Reports **7**(1), 13117 (2017).

131. A. P. Vinogradov, A. V Dorofeenko, A. A. Pukhov, and A. A. Lisyansky, "Exciting surface plasmon polaritons in the Kretschmann configuration by a light beam," Physical Review B **97**(23), 235407 (2018).

132. F. Cao, D. Li, R. Deng, L. Huang, D. Pan, J. Wang, S. Li, and G. Qin, "Synthesis of small Fe2O3 nanocubes and their enhanced water vapour adsorption–desorption properties," RSC Advances **5**(103), 84587–84591 (2015).

133. J. Puibasset and R. J.-M. Pellenq, "Influence of temperature on water adsorption / desorption hysteresis loop in disordered mesoporous silica glass by Grand Canonical Monte Carlo simulation method," in *Characterization of Porous Solids VII*, P. L. Llewellyn, F. Rodriquez-Reinoso, J. Rouqerol, and N. B. T.-S. in S. S. and C. Seaton, eds. (Elsevier, 2007), **160**, pp. 535–541.

134. E. Armstrong and C. O'Dwyer, "Artificial opal photonic crystals and inverse opal structures – fundamentals and applications from optics to energy storage," Journal of Materials Chemistry C **3**(24), 6109–6143 (2015).

135. M. Y. Tsvetkov, B. N. Khlebtsov, V. A. Khanadeev, V. N. Bagratashvili, P. S. Timashev, M. I. Samoylovich, and N. G. Khlebtsov, "SERS substrates formed by gold nanorods deposited on colloidal silica films," Nanoscale Research Letters **8**(1), 250 (2013).

136. G. I. N. Waterhouse and M. R. Waterland, "Opal and inverse opal photonic crystals: Fabrication and characterization," Polyhedron **26**(2), 356–368 (2007).

137. A. A. Akhmadeev and M. Kh Salakhov, "Investigations of properties of opal-like photonic crystals using combined methods," Journal of Physics: Conference Series **714**, 12003 (2016).

138. F. Tian, J. Kanka, S. A. Sukhishvili, and H. Du, "Photonic crystal fiber for layer-by-layer assembly and measurements of polyelectrolyte thin films," Optics Letters **37**(20), 4299–4301 (2012).

139. D. Lopez-Torres, C. Elosua, J. Villatoro, J. Zubia, M. Rothhardt, K. Schuster, and F. J. Arregui, "Photonic crystal fiber interferometer coated with a PAH/PAA nanolayer as humidity sensor," Sensors and Actuators, B: Chemical **242**, 1065–1072 (2017).

140. F. Tian, S. Sukhishvili, and H. Du, "Photonic Crystal Fiber as a Lab-in-Fiber Optofluidic Platform BT - Lab-on-Fiber Technology," in A. Cusano, M. Consales, A. Crescitelli, and A. Ricciardi, eds. (Springer International Publishing, 2015), pp. 315–334.

141. F. Benabid, F. Couny, J. C. Knight, T. A. Birks, and P. S. J. Russell, "Compact, stable and efficient all-fibre gas cells using hollow-core photonic crystal fibres," Nature **434**(7032), 488–491 (2005).

142. J. S. Skibina, R. Iliew, J. Bethge, M. Bock, D. Fischer, V. I. Beloglasov, R. Wedell, and G. Steinmeyer, "A chirped photonic-crystal fibre," Nature Photonics **2**(11), 679–683 (2008).

143. A. M. Zheltikov, "Colors of thin films, antiresonant phenomena in optical systems, and the limiting loss of modes in hollow optical waveguides," Physics-Uspekhi **51**(6), 591–600 (2008).

144. A. Stefani, M. Stecher, G. E. Town, and O. Bang, "Direct Writing of Fiber Bragg Grating in Microstructured Polymer Optical Fiber," IEEE Photonics Technology Letters **24**(13), 1148–1150 (2012).

145. L. Ding, Z. Li, Q. Ding, X. Shen, Y. Yuan, and J. Huang, "Microstructured optical fiber based chloride ion sensing method for concrete health monitoring," Sensors and Actuators B: Chemical **260**, 763–769 (2018).

146. C. Wu, B. Guan, Z. Wang, and X. Feng, "Characterization of Pressure Response of Bragg Gratings in Grapefruit Microstructured Fibers," Journal of Lightwave Technology **28**(9), 1392–1397 (2010).

147. S. V German, O. A. Inozemtseva, A. V Markin, K. Metvalli, G. B. Khomutov, and D. A. Gorin, "Synthesis of magnetite hydrosols in inert atmosphere," Colloid Journal **75**(4), 483–486 (2013).

148. V. A. Khanadeev, B. N. Khlebtsov, S. A. Klimova, M. Y. Tsvetkov, V. N. Bagratashvili, G. B. Sukhorukov, and N. G. Khlebtsov, "Large-scale high-quality 2D silica crystals: dip-drawing formation and decoration with gold nanorods and nanospheres for SERS analysis," Nanotechnology **25**(40), 405602 (2014).

149. L. Zhang, H. Guo, and J. Sun, "Salt effects on the structural tailoring of layer-by-layer assembled polyelectrolyte complexes and salt-containing polyelectrolyte films," Thin Solid Films **653**, 258–266 (2018).

150. T. Ermatov, J. S. Skibina, R. E. Noskov, and D. A. Gorin, "Layer-by-layer assembled-composite nanocoating for functionalization of microstructured optical

fibers," in *Journal of Physics: Conference Series* (2020), **1571**(1).

151. M. Kolasińska and P. Warszyński, "The effect of support material and conditioning on wettability of PAH/PSS multilayer films," Bioelectrochemistry **66**(1–2), 65–70 (2005).

152. M. Kolasińska and P. Warszyński, "The effect of nature of polyions and treatment after deposition on wetting characteristics of polyelectrolyte multilayers," Applied Surface Science **252**(3), 759–765 (2005).

153. G. B. Sukhorukov, E. Donath, H. Lichtenfeld, E. Knippel, M. Knippel, A. Budde, and H. Möhwald, "Layer-by-layer self assembly of polyelectrolytes on colloidal particles," Colloids and Surfaces A: Physicochemical and Engineering Aspects **137**(1), 253–266 (1998).

154. Z. Feldötö, I. Varga, and E. Blomberg, "Influence of salt and rinsing protocol on the structure of PAH/PSS polyelectrolyte multilayers," Langmuir **26**(22), 17048–17057 (2010).

155. P. A. Neff, A. Naji, C. Ecker, B. Nickel, R. V. Klitzing, and A. R. Bausch, "Electrical detection of self-assembled polyelectrolyte multilayers by a thin film resistor," Macromolecules **39**(2), 463–466 (2006).

156. A. D. Cramer, W. F. Dong, N. L. Benbow, J. L. Webber, M. Krasowska, D. A. Beattie, and J. K. Ferri, "The influence of polyanion molecular weight on polyelectrolyte multilayers at surfaces: Elasticity and susceptibility to saloplasticity of strongly dissociated synthetic polymers at fluid-fluid interfaces," Physical Chemistry Chemical Physics (2017).

157. M. Kolasińska, R. Krastev, and P. Warszyński, "Characteristics of polyelectrolyte multilayers: Effect of PEI anchoring layer and posttreatment after deposition," Journal of Colloid and Interface Science **305**(1), 46–56 (2007).

158. S. Kang, D. E. Day, and J. O. Stoffer, "Measurement of the refractive index of glass fibers by the Christiansen-Shelyubskii method," Journal of Non-Crystalline Solids **220**(2–3), 299–308 (1997).

159. H. G. Tompkins, S. Smith, and D. Convey, "Optimizing the ellipsometric analysis of a transparent layer on glass," Surface and Interface Analysis **29**(12), 845–850 (2000).

160. D. Wang, Y. He, J. Zhang, W. Li, X. Fu, M. Tian, Y. Zhou, and Z. Yao, "Layer-by-layer assembled transparent polymeric adhesive films with adjustable refractive indices," International Journal of Adhesion and Adhesives **85**, 202–207 (2018).

161. J. H. Kim, J. H. Hwang, and T. Y. Lim, "A layer-by-layer self-assembly method for organic-inorganic hybrid multilayer thin films," Journal of Ceramic Processing Research **10**(6), 770–773 (2009).

162. X. Jiang, T. G. Euser, A. Abdolvand, F. Babic, F. Tani, N. Y. Joly, J. C. Travers, and P. S. J. Russell, "Single-mode hollow-core photonic crystal fiber made from soft glass," Optics Express **19**(16), 15438–15444 (2011).

163. F. G. Omenetto, N. A. Wolchover, M. R. Wehner, M. Ross, A. Efimov, A. J. Taylor, V. V. R. K. Kumar, A. K. George, J. C. Knight, N. Y. Joly, and P. S. J. Russell, "Spectrally smooth supercontinuum from 350 nm to 3 μm in sub-centimeter lengths of soft-glass photonic crystal fibers.," Optics Express **14**(11),

4928–4934 (2006).

164. M. Klimczak, B. Siwicki, P. Skibiński, D. Pysz, R. Stępień, A. Heidt, C. Radzewicz, and R. Buczyński, "Coherent supercontinuum generation up to 2.3 µm in all-solid soft-glass photonic crystal fibers with flat all-normal dispersion," Optics Express **22**(15), 18824–18832 (2014).

165. M. Klimczak, B. Siwicki, P. Skibinski, D. Pysz, R. Stepien, A. Szolno, J. Pniewski, C. Radzewicz, and R. Buczynski, "Mid-infrared supercontinuum generation in soft-glass suspended core photonic crystal fiber," Optical and Quantum Electronics **46**(4), 563–571 (2014).

166. A. N. Kolyadin, A. F. Kosolapov, A. D. Pryamikov, A. S. Biriukov, V. G. Plotnichenko, and E. M. Dianov, "Light transmission in negative curvature hollow core fiber in extremely high material loss region," Optics Express **21**(8), 9514–9519 (2013).

167. X. Zhang, S. Gao, Y. Wang, W. Ding, X. Wang, and P. Wang, "7-cell hollow-core photonic bandgap fiber with broad spectral bandwidth and low loss," Optics Express **27**(8), 11608–11616 (2019).

168. J. D. Shephard, W. N. MacPherson, R. R. J. Maier, J. D. C. Jones, D. P. Hand, M. Mohebbi, A. K. George, P. J. Roberts, and J. C. Knight, "Single-mode mid-IR guidance in a hollow-core photonic crystal fiber," Optics Express **13**(18), 7139 (2005).

169. A. D. Pryamikov, A. S. Biriukov, A. F. Kosolapov, V. G. Plotnichenko, S. L. Semjonov, and E. M. Dianov, "Demonstration of a waveguide regime for a silica hollow - core microstructured optical fiber with a negative curvature of the core boundary in the spectral region > 3.5 µm," Optics Express **19**(2), 1441–1448 (2011).

170. J. K. Lyngsø, B. J. Mangan, C. Jakobsen, and P. J. Roberts, "7-cell core hollow-core photonic crystal fibers with low loss in the spectral region around 2 µm," Optics Express **17**(26), 23468–23473 (2009).

171. F. Yu, W. J. Wadsworth, and J. C. Knight, "Low loss silica hollow core fibers for 3–4 µm spectral region," Optics Express **20**(10), 11153–11158 (2012).

172. W. Talataisong, R. Ismaeel, T. H. R. Marques, S. Abokhamis Mousavi, M. Beresna, M. A. Gouveia, S. R. Sandoghchi, T. Lee, C. M. B. Cordeiro, and G. Brambilla, "Mid-IR Hollow-core microstructured fiber drawn from a 3D printed PETG preform," Scientific Reports **8**(1), 8113 (2018).

173. N. V Wheeler, T. D. Bradley, J. R. Hayes, M. A. Gouveia, S. Liang, Y. Chen, S. R. Sandoghchi, S. M. Abokhamis Mousavi, F. Poletti, M. N. Petrovich, and D. J. Richardson, "Low-loss Kagome hollow-core fibers operating from the near- to the mid-IR," Optics Letters **42**(13), 2571–2574 (2017).

174. X. Jiang, N. Y. Joly, M. A. Finger, F. Babic, G. K. L. Wong, J. C. Travers, and P. S. J. Russell, "Deep-ultraviolet to mid-infrared supercontinuum generated in solid-core ZBLAN photonic crystal fibre," Nature Photonics **9**(2), 133–139 (2015).

175. H. H. Nguyen, J. Park, S. Kang, and M. Kim, "Surface Plasmon Resonance: A Versatile Technique for Biosensor Applications," Sensors **15**(5), (2015).

176. A. Klimchuk, V. Lychagov, E. Salamatova, T. Ermatov, D. Gorin, P.

Rudakovskaya, S. German, and P. Kapralov, "Sensor device for recognition of mixtures of volatile compounds and method of its production," (2020).

177. Z. Li, J. Zhong, and D. A. Levin, "Modeling of CO2 Homogeneous and Heterogeneous Condensation Plumes," The Journal of Physical Chemistry C **114**(12), 5276–5286 (2010).

178. E. Kilic, M. V Novoselova, S. H. Lim, N. A. Pyataev, S. I. Pinyaev, O. A. Kulikov, O. A. Sindeeva, O. A. Mayorova, R. Murney, M. N. Antipina, B. Haigh, G. B. Sukhorukov, and M. V Kiryukhin, "Formulation for Oral Delivery of Lactoferrin Based on Bovine Serum Albumin and Tannic Acid Multilayer Microcapsules," Scientific Reports **7**(1), 44159 (2017).

179. J. T. Busher, "Serum Albumin and Globulin," in *Clinical Methods: The History, Physical, and Laboratory Examinations*, E. Walker H. K., Hall W. D., Hurst J. W., ed., 3rd editio (Butterworths, 1990), pp. 479–499.

180. L. Yang, H. Sun, W. Jiang, T. Xu, B. Song, R. Peng, L. Han, and L. Jia, "A Chemical Method for Specific Capture of Circulating Tumor Cells Using Label-Free Polyphenol-Functionalized Films," Chemistry of Materials **30**(13), 4372–4382 (2018).

181. M. V Lomova, G. B. Sukhorukov, and M. N. Antipina, "Antioxidant Coating of Micronsize Droplets for Prevention of Lipid Peroxidation in Oil-in-Water Emulsion," ACS Applied Materials & Interfaces **2**(12), 3669–3676 (2010).

182. L. Xu, D. Pranantyo, K.-G. Neoh, and E.-T. Kang, "Tea Stains-Inspired Antifouling Coatings Based on Tannic Acid-Functionalized Agarose," ACS Sustainable Chemistry & Engineering **5**(4), 3055–3062 (2017).

183. X. Gao, Z. Xu, G. Liu, and J. Wu, "Polyphenols as a versatile component in tissue engineering," Acta Biomaterialia **119**, 57–74 (2021).

184. N. Sahiner, S. Sagbas, M. Sahiner, C. Silan, N. Aktas, and M. Turk, "Biocompatible and biodegradable poly(Tannic Acid) hydrogel with antimicrobial and antioxidant properties," International Journal of Biological Macromolecules **82**, 150–159 (2016).

185. J. Borges and J. F. Mano, "Molecular Interactions Driving the Layer-by-Layer Assembly of Multilayers," Chemical Reviews **114**(18), 8883–8942 (2014).

186. H. T. M. Phan, S. Bartelt-Hunt, K. B. Rodenhausen, M. Schubert, and J. C. Bartz, "Investigation of Bovine Serum Albumin (BSA) Attachment onto Self-Assembled Monolayers (SAMs) Using Combinatorial Quartz Crystal Microbalance with Dissipation (QCM-D) and Spectroscopic Ellipsometry (SE)," PLOS ONE **10**(10), e0141282 (2015).

187. J. Cai, E. Perfect, C.-L. Cheng, and X. Hu, "Generalized Modeling of Spontaneous Imbibition Based on Hagen–Poiseuille Flow in Tortuous Capillaries with Variably Shaped Apertures," Langmuir **30**(18), 5142–5151 (2014).

188. R. Osawa and T. P. Walsh, "Effects of acidic and alkaline treatments on tannic acid and its binding property to protein," Journal of Agricultural and Food Chemistry **41**(5), 704–707 (1993).

189. A. Sihvola, *Electromagnetic Mixing Formulas and Applications*, Electromag (Institute of Electrical Engineers, 1999).

190. Global Chemical Network, "Tannic acid," http://www.chemnet.com/cas/en/1401-55-4/tannic-acid.html.

191. S. T. Dubas and J. B. Schlenoff, "Swelling and Smoothing of Polyelectrolyte Multilayers by Salt," Langmuir **17**(25), 7725–7727 (2001).

192. M. A. Go and V. R. Daria, "Light-neuron interactions: Key to understanding the brain," Journal of Optics (United Kingdom) **19**(2), 023002 (2017).

193. I. Y. Yanina, E. N. Lazareva, and V. V. Tuchin, "Refractive index of adipose tissue and lipid droplet measured in wide spectral and temperature ranges," Applied Optics **57**(17), 4839 (2018).

194. A. Ricciardi, A. Crescitelli, P. Vaiano, G. Quero, M. Consales, M. Pisco, E. Esposito, and A. Cusano, "Lab-on-fiber technology: a new vision for chemical and biological sensing," Analyst **140**(24), 8068–8079 (2015).

195. H. Zhu, S. O. Isikman, O. Mudanyali, A. Greenbaum, and A. Ozcan, "Optical imaging techniques for point-of-care diagnostics," Lab on a Chip **13**(1), 51–67 (2013).

196. S. Tabassum and R. Kumar, "Advances in Fiber-Optic Technology for Point-of-Care Diagnosis and In Vivo Biosensing," Advanced Materials Technologies **5**(5), 1900792 (2020).

197. M. Soler, C. S. Huertas, and L. M. Lechuga, "Label-free plasmonic biosensors for point-of-care diagnostics: a review," Expert Review of Molecular Diagnostics **19**(1), 71–81 (2019).

198. O. S. Zhernovaya, V. V. Tuchin, and I. V. Meglinski, "Monitoring of blood proteins glycation by refractive index and spectral measurements," Laser Physics Letters **5**(6), 460–464 (2008).

199. M. Daimon and A. Masumura, "Measurement of the refractive index of distilled water from the near-infrared region to the ultraviolet region," Applied Optics **46**(18), 3811–3820 (2007).

200. A. A. Rifat, R. Ahmed, A. K. Yetisen, H. Butt, A. Sabouri, G. A. Mahdiraji, S. H. Yun, and F. R. M. Adikan, "Photonic crystal fiber based plasmonic sensors," Sensors and Actuators B: Chemical **243**, 311–325 (2017).

201. M. R. Hasan, S. Akter, A. A. Rifat, S. Rana, K. Ahmed, R. Ahmed, H. Subbaraman, and D. Abbott, "Spiral Photonic Crystal Fiber-Based Dual-Polarized Surface Plasmon Resonance Biosensor," IEEE Sensors Journal **18**(1), 133–140 (2018).

202. T. L. McMeekin, M. L. Groves, and N. J. Hipp, "Refractive Indices of Amino Acids, Proteins, and Related Substances," in *Amino Acids and Serum Proteins* (Advances in Chemistry; American Chemical Society, 1964), pp. 54–66.

203. M. Halwer, G. C. Nutting, and B. A. Brice, "Molecular Weight of Lactoglobulin, Ovalbumin, Lysozyme and Serum Albumin by Light Scattering," Journal of the American Chemical Society **73**(6), 2786–2790 (1951).

204. H. Edelhoch, "The properties of thyroglobulin. I. The effects of alkali.," The Journal of biological chemistry **235**, 1326–1334 (1960).

205. G. E. Perlmann and L. G. Longsworth, "The Specific Refractive Increment of Some Purified Proteins," Journal of the American Chemical Society **70**(8), 2719–

2724 (1948).

206. R. Barer and S. Tkaczyk, "Refractive index of concentrated protein solutions," Nature **173**(4409), 821–822 (1954).

207. M. B. Huglin, "Specific refractive index increments of polymer solutions. Part I. Literature values," Journal of Applied Polymer Science **9**(12), 3963–4001 (1965).

208. T. Tumolo, L. Angnes, and M. S. Baptista, "Determination of the refractive index increment (dn/dc) of molecule and macromolecule solutions by surface plasmon resonance," Analytical Biochemistry **333**(2), 273–279 (2004).

209. A. K. Wright and M. R. Thompson, "Hydrodynamic structure of bovine serum albumin determined by transient electric birefringence," Biophysical Journal **15**(2), 137–141 (1975).

210. T. J. Peters, "The Albumin Molecule: Its Structure and Chemical Properties," in *All About Albumin.Biochemistry, Genetics, and Medical Applications.* (Academic Press, 1996), pp. 9–75.

211. O. Levy and D. Stroud, "Maxwell Garnett theory for mixtures of anisotropic inclusions: Application to conducting polymers," Physical Review B - Condensed Matter and Materials Physics **56**(13), 8035–8046 (1997).

212. Sigma-Aldrich, "A2153 - Bovine Serum Albumin," https://www.sigmaaldrich.com/catalog/product/sigma/a2153?lang=en&region=RU .

213. Agat-Med, "Bilirubin Etalon Agat," https://www.agat.ru/documents/instructions/5075/.

214. R. Barer and S. Joseph, "Refractometry of Living Cells: Part 1 Basic Principles," Quarterly Journal of Microscopial Science1 **95**(4), 399–423 (1954).

215. E. N. Lazareva and V. V. Tuchin, "Measurement of refractive index of hemoglobin in the visible/NIR spectral range," Journal of Biomedical Optics **23**(03), (2018).

216. N. Mclntyre and S. Rosalki, "22 - Tests of the Functions of the Liver," in D. L. Williams and V. B. T.-S. F. of B. in C. P. (Second E. Marks, eds. (Butterworth-Heinemann, 1994), pp. 383–398.

217. F. S. H. Krismastuti, H. Bayat, N. H. Voelcker, and H. Schönherr, "Real Time Monitoring of Layer-by-Layer Polyelectrolyte Deposition and Bacterial Enzyme Detection in Nanoporous Anodized Aluminum Oxide," Analytical Chemistry **87**(7), 3856–3863 (2015).

218. F. Caruso, K. Niikura, D. N. Furlong, and Y. Okahata, "2. Assembly of Alternating Polyelectrolyte and Protein Multilayer Films for Immunosensing," Langmuir **13**(13), 3427–3433 (1997).

219. F. Caruso, H. Lichtenfeld, E. Donath, and H. Möhwald, "Investigation of Electrostatic Interactions in Polyelectrolyte Multilayer Films: Binding of Anionic Fluorescent Probes to Layers Assembled onto Colloids," Macromolecules **32**(7), 2317–2328 (1999).

220. R. Steitz, V. Leiner, R. Siebrecht, and R. v. Klitzing, "Influence of the ionic strength on the structure of polyelectrolyte films at the solid/liquid interface," Colloids and Surfaces A: Physicochemical and Engineering Aspects **163**(1), 63–70 (2000).

221. M. Gopinadhan, O. Ivanova, H. Ahrens, J.-U. Günther, R. Steitz, and C. A. Helm, "The Influence of Secondary Interactions during the Formation of Polyelectrolyte Multilayers: Layer Thickness, Bound Water and Layer Interpenetration," The Journal of Physical Chemistry B **111**(29), 8426–8434 (2007).

222. M. Lösche, J. Schmitt, G. Decher, W. G. Bouwman, and K. Kjaer, "Detailed Structure of Molecularly Thin Polyelectrolyte Multilayer Films on Solid Substrates as Revealed by Neutron Reflectometry," Macromolecules **31**(25), 8893–8906 (1998).

223. W.-F. Dong, J. K. Ferri, T. Adalsteinsson, M. Schönhoff, G. B. Sukhorukov, and H. Möhwald, "Influence of Shell Structure on Stability, Integrity, and Mesh Size of Polyelectrolyte Capsules: Mechanism and Strategy for Improved Preparation," Chemistry of Materials **17**(10), 2603–2611 (2005).

224. J. J. Harris and M. L. Bruening, "Electrochemical and in Situ Ellipsometric Investigation of the Permeability and Stability of Layered Polyelectrolyte Films," Langmuir **16**(4), 2006–2013 (2000).

225. A. N. Raegen, K. Reiter, A. Dion, A. J. Clarke, J. Lipkowski, and J. R. Dutcher, "Advances in Surface Plasmon Resonance Imaging Enable Quantitative Tracking of Nanoscale Changes in Thickness and Roughness," Analytical Chemistry **86**(7), 3346–3354 (2014).

226. Y. Shevchenko, N. U. Ahamad, A. Ianoul, and J. Albert, "In situ monitoring of the formation of nanoscale polyelectrolyte coatings on optical fibers using Surface Plasmon Resonances," Optics Express **18**(19), 20409–20421 (2010).

227. J. Ballato, H. Ebendorff-Heidepriem, J. Zhao, L. Petit, and J. Troles, "Glass and Process Development for the Next Generation of Optical Fibers: A Review," Fibers **5**(1), (2017).

228. T. Ermatov, I. Gnusov, J. Skibina, R. E. Noskov, and D. Gorin, "Noncontact characterization of microstructured optical fibers coating in real time," Optics Letters **46**(19), 4793–4796 (2021).